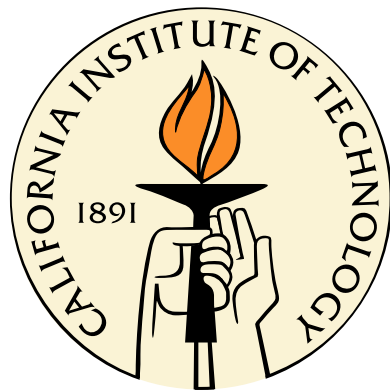


LIGHTWEIGHT DEFORMABLE MIRRORS FOR FUTURE SPACE TELESCOPES

Thesis by
Keith Patterson

In Partial Fulfillment of the Requirements
for the Degree of
Doctor of Philosophy



California Institute of Technology
Pasadena, California

2014
(Defended December 12, 2013)

UMI Number: 3609385

All rights reserved

INFORMATION TO ALL USERS

The quality of this reproduction is dependent upon the quality of the copy submitted.

In the unlikely event that the author did not send a complete manuscript and there are missing pages, these will be noted. Also, if material had to be removed, a note will indicate the deletion.



UMI 3609385

Published by ProQuest LLC (2014). Copyright in the Dissertation held by the Author.

Microform Edition © ProQuest LLC.

All rights reserved. This work is protected against unauthorized copying under Title 17, United States Code



ProQuest LLC.
789 East Eisenhower Parkway
P.O. Box 1346
Ann Arbor, MI 48106 - 1346

© 2014

Keith Patterson

All Rights Reserved

Dedicated to my parents, whose love encouraged, sacrifice enabled, and hard work inspired me to chase my dreams. And to Zheng, for her patience and loving support over many years.

Acknowledgments

The work presented herein could not have been done without the support of many people. First and foremost, I would like to recognize my advisor, Professor Sergio Pellegrino, whose vision, guidance, and behind-the-scenes orchestration enabled me to reach this point. He never takes “it can’t be done” as a finality, and always pushes forward and higher. I would also like to recognize my thesis committee: Professor Guruswami “Ravi” Ravichandran, Professor Julia Greer, and Professor Dennis Kochmann. I make a special acknowledgement to Ravi, whose gentle encouragements from time to time were always welcome. I’d also like to thank the Keck Institute for Space Studies and the Jet Propulsion Laboratory for funding our efforts and believing in our vision.

Throughout my time here at Caltech I have had several mentors to whom I am eternally grateful for their advice and wisdom: Dr. James Breckinridge, for transforming an optically illiterate engineering student into a Ph.D. recipient who works on telescope design and active optics. His tireless dedication and the vast experience he voluntarily brings to our efforts are quite commendable and admirable. Dr. Risaku Toda, for introducing me to the world of microfabrication, and patiently teaching me the various methods and machinery that allowed me to make these active mirrors. Mr. Victor White, who always had a “crazy idea” whenever I would get stuck, which turned out to be not so crazy more often than not. Dr. Harish Manohara and Dr. Andrew Shapiro, for establishing the collaboration between our lab and his, and working with my advisor to enable new areas of research.

I have collaborated with many people during my time at Caltech on research, projects, and classes, and special acknowledgements go to Professor Chiara Daraio, Professor Abha Misra, Dr. Greg Davis, Dr. Yunjin Kim, Dr. Terry Gdoutos, Dr. Namiko Yamamoto, Dr. Marie Laslandes, and fellow mirror researcher John Steeves. The staff here in GALCIT were also extremely helpful, especially Petros Arakelian, Joe Haggerty, Kathleen Jackson, Christine Ramirez, and, of course, Dimity Nelson, who keeps the place running.

I would like to also generally acknowledge past and present members of my lab group and project team, whose hard work were always an inspiration for me and pushed me to always keep going: the staff and researchers in the Microdevices Lab who were always so friendly and helpful, my fellow classmates who helped each other through the first year, and the various Ae105 classes who put so much hard work into the design project in such a limited timeframe. I would like to thank my friends for their support, and last but *most importantly*, my family. All so scattered about, and yet always so close.

Abstract

This thesis presents a concept for ultra-lightweight deformable mirrors based on a thin substrate of optical surface quality coated with continuous active piezopolymer layers that provide modes of actuation and shape correction. This concept eliminates any kind of stiff backing structure for the mirror surface and exploits micro-fabrication technologies to provide a tight integration of the active materials into the mirror structure, to avoid actuator print-through effects. Proof-of-concept, 10-cm-diameter mirrors with a low areal density of about 0.5 kg/m^2 have been designed, built and tested to measure their shape-correction performance and verify the models used for design. The low cost manufacturing scheme uses replication techniques, and strives for minimizing residual stresses that deviate the optical figure from the master mandrel. It does not require precision tolerancing, is lightweight, and is therefore potentially scalable to larger diameters for use in large, modular space telescopes. Other potential applications for such a laminate could include ground-based mirrors for solar energy collection, adaptive optics for atmospheric turbulence, laser communications, and other shape control applications.

The immediate application for these mirrors is for the Autonomous Assembly and Reconfiguration of a Space Telescope (AAReST) mission, which is a university mission under development by Caltech, the University of Surrey, and JPL. The design concept, fabrication methodology, material behaviors and measurements, mirror modeling, mounting and control electronics design, shape control experiments, predictive performance analysis, and remaining challenges are presented herein. The experiments have validated numerical models of the mirror, and the mirror models have been used within a model of the telescope in order to predict the optical performance. A demonstration of this mirror concept, along with other new telescope technologies, is planned to take place during the AAReST mission.

Contents

Acknowledgments	iv
Abstract	v
1 Introduction	1
1.1 Motivation	1
1.2 Background	1
1.2.1 Segmented Large Aperture Concept	2
1.2.2 AAReST Technology Demonstration Mission	3
1.2.3 Existing Deformable Mirror Technologies	3
1.2.4 Need for New Technology	5
2 Deformable Mirror Design Concept	9
2.1 Laminate Concept	9
2.2 Active Materials	10
2.3 Substrate Selection	11
2.4 Design Summary	15
3 Deformable Mirror Fabrication	16
3.1 Substrate Processing	16
3.1.1 Flat Substrates	16
3.1.2 Curved Substrates	16
3.2 Laminate Processing	18
3.3 Mirror Coating	20
3.3.1 Reflective Surface	21
3.3.2 Thick Reflective Layer	22
3.4 Kinematic Mounting	22

4 Material Behaviors	30
4.1 Borosilicate Glass Properties	30
4.2 P(VDF-TrFE) Properties	30
4.2.1 Piezoelectric Behavior	30
4.2.2 Thermal Behavior	32
4.2.3 High Temperatures and Polarization	32
4.2.4 Time-Dependent Behaviors	33
4.2.4.1 Viscoelastic Master Curve	33
4.2.4.2 Piezoelectric Creep	33
4.2.4.3 Stress Annealing	34
4.3 Laminate Properties	34
4.3.1 Laminate Thermal Balance	34
5 Deformable Mirror Modeling and Optimization	52
5.1 Mirror Shape Control	52
5.2 Electrode Design	54
5.3 Optimized Pattern	58
6 Mirror Experiments	64
6.1 Measurement Testbed	64
6.2 Control Implementation	65
6.3 Measured Influence Functions	66
6.3.1 16-Channel Prototype	66
6.3.2 41-Channel Prototype	66
6.4 Focus Control	67
6.5 Shape Control	67
6.5.1 16-Channel Prototype	67
7 Mirror Performance Analysis	79
7.1 Acoustics and Launch Survival	79
7.1.1 Vibration Model	80
7.1.2 Forced Vibrations	82
7.1.3 Modal Damping	84
7.1.4 Example Case: Delta IV Launch	84
7.1.4.1 Mirror Damping Estimation	85
7.1.4.2 Loads and Response	87

7.2	Mirror Shape Stability for Imaging	88
7.2.1	Vibrational Disturbances	88
7.2.1.1	Example Case: Reaction Wheel Vibration Effect on Image Quality	90
7.3	AAReST Closed-Loop System Performance Model	95
7.3.1	AAReST Telescope Operation Overview	95
7.3.2	System Modeling	96
7.3.3	Closed-Loop Performance Estimates	99
7.3.3.1	Wavefront Flattening	100
7.3.3.2	Spot Size Reduction	101
7.4	Performance Summary	102
8	Conclusion	106
Bibliography		108

List of Figures

1.1	Concept illustration of a large segmented mirror being autonomously assembled in space.	2
1.2	An f/1, parabolic, 10-m-diameter mirror with 1-m-diameter identical, active, spherical segments. The colorbar displays the shape errors, in units of 633 nm wavelengths, of the segments (a) before, and (b) after correction.	6
1.3	Rendering of the current design of the AAReST telescope showing the four primary mirror segments mounted on mirrorcraft, deployed boom, and camera/wavefront sensor.	7
1.4	Four different ways of flexing a deformable mirror: (a) surface-normal, (b) boundary, (c) surface-parallel, and (d) boundary + surface-parallel actuation.	8
2.1	Electro-active polymers: (a) PVDF copolymer, and (b) P(VDF-TrFE) copolymer.	12
2.2	3D model of two arrangements of the PVDF molecule. Black spheres represent carbon atoms, red spheres represent fluorine, and yellow spheres are hydrogen.	13
2.3	Estimated actuation capability of 20- μm -thick P(VDF-TrFE) coating as a function of substrate biaxial modulus and thickness. A practical lower limit is imposed by substrate buckling due to residual poling strain.	14
2.4	Layers of an ultra-lightweight deformable mirror.	15
3.1	Estimated viscosity curve of Schott D263 glass using data reported by PGO [31]	17
3.2	Illustration of slumping process. As the wafer is heated from left to right, it conforms to the mold shape.	18
3.3	Typical film coating thicknesses for P(VDF-TrFE) (75:25 copolymer, by mol) dissolved in cyclopentanone solvent (80:20 copolymer to solvent, by mass). The resin was spread on the substrate at 500 RPM for 3 seconds before the final spin for 10 seconds.	19
3.4	Active laminate (a) before, and (b) after poling process. The thin laminate is wax bonded onto a chuck for processing. Small pinholes in the copolymer film can be seen; they were created by electrical discharges during the poling process due to coating imperfections. The electrode pattern shown on the sample was a result of design optimization work done by Dr. Marie Laslandes for the AAReST mission, and is described in a separate article [21].	24

3.5	Normal incidence intensity reflectance of aluminum, gold, and silver as a function of wavelength. Computed from index of refraction data from Raki and Palik [32, 26].	25
3.6	Intensity reflectance of S and P polarizations at an incidence angle of 45 degrees for aluminum, gold, and silver as a function of wavelength. Computed from index of refraction data from Raki and Palik [32, 26].	26
3.7	Comparison of annealing effects on film stress of thick coatings of pure aluminum vs. layered aluminum+chromium.	27
3.8	Cross-section of magnetic mounting scheme. Pairs of polished, magnetized spheres pinch the mirror at three places around the rim to hold it on a PCB. Tiny wire-bonded electrical connections jump from the board to the mirror.	28
3.9	(a) Front and (b) back of an assembled mirror prototype mounted on a custom-built 3-axis piston/tip/tilt gimbal.	29
4.1	Estimated viscosity curve of Schott D263 glass using data reported by PGO [31].	31
4.2	Copolymer response to poling cycles: (a) butterfly curves showing poling switching behavior, and (b) electric polarization.	37
4.3	Copolymer material test data: (a) Differential scanning calorimetry (DSC), and (b) Thermo-gravimetric analysis (TGA).	38
4.4	XRD response peaks of the P(VDF-TrFE) copolymer film. The peak shifts to the right after poling, and back to the left after annealing at or above the Curie temperature.	39
4.5	Typical actuation cycle of the copolymer in the quasi-linear region.	40
4.6	Piezoelectric coefficient temperature dependence of a similar P(VDF-TrFE) material as reported by Dargaville et al [8].	41
4.7	Loss and storage moduli for the copolymer thin film.	42
4.8	Copolymer material test data: (a) in-plane thermal expansion, and (b) CTE estimate.	43
4.9	Loss of P(VDF-TrFE) piezoelectric capability due to elevated poling temperatures. The material sample was subjected to poling/depoling 0.1 Hz cycles continuously over several hours while the temperature was simultaneously raised to 68°C and then returned to room temperature.	44
4.10	Retention of P(VDF-TrFE) piezoelectric capability over wide range of annealing temperatures. The material sample's polarization loop at 0.05 Hz was measured at room temperature after each successive annealing.	45
4.11	Copolymer viscoelastic master curve showing the storage and loss moduli compiled using time-temperature superposition of DMA test data at various frequencies and temperatures.	46
4.12	Estimates of the relaxation modulus derived from the master curve data using various approximate transforms from frequency domain into the time domain [38].	47

4.13	Estimates of the creep compliance derived from the master curve data using various approximate transforms from frequency domain into the time domain [38].	48
4.14	Laminate response to square wave voltage. Response indicates piezoelectric relaxation in the polymer. The average relaxation time was approximately 130 seconds.	49
4.15	Annealing of the thermoplastic copolymer. The sample was successively annealed at higher temperatures. Stress measurements were taken at room temperature between each anneal. Significant points: (a) film as deposited; (b) poled; (c) Curie transition; (d) melting; (e) poled again.	50
4.16	Estimated laminate behavior for 20- μm copolymer film coated on 200- μm glass substrate across a wide temperature range: (a) estimated piezoelectric stroke, and (b) effect of thermal imbalance on allowable operating temperatures.	51
5.1	Exploded views of two example mirror designs that were explored at various points during this research: (a) single active layer design and (b) double active layer design.	55
5.2	Finite element predictions of influence function shapes for selected electrodes from (a) coarse and (b) fine patterns of Figure 5.1. Units are $\mu\text{m}/\text{V}$	56
5.3	Electrode design patterns (a-c) triangular lattices with 42, 90, and 156 actuators; (d-f) hexagonal patch tessellations with 43, 91, and 151 actuators.	57
5.4	Correctabilities of six actuation patterns in Figure 5.3, for first 30 Zernike modes.	58
5.5	General relationship between residual and input error in any chosen mode.	59
5.6	Variation of residual RMS error with RMS error in three chosen modes for the six actuation patterns in Figure 5.3; (a) Mode Z_2^0 defocus; (b) Mode Z_2^{-2} astigmatism; (c) Mode Z_3^{-1} coma. Reference wavelength is 633 nm.	60
5.7	Optimized "Notre Dame" electrode pattern design with 41 actuators filling most of the 100-mm-diameter area with small gaps for fabrication purposes.	61
5.8	Modal correctabilities for the lowest Zernikes for the optimized "Notre Dame" pattern.	62
5.9	Stroke and correctability performance for the low order shape modes: focus, astigmatism, and coma. The points of first actuator saturation are marked on the plot with circles.	63
6.1	Schematic diagram of experimental measurement setup.	65
6.2	Photo of experimental measurement setup.	69

6.3	(a) Schematic diagram of control system showing wavefront feedback from the mirror passed to a controller; the controller then uses a high voltage amplifier and multiplexer to apply a new set of voltages to the mirror electrodes. (b) Photo of a 10-cm-by-10-cm prototype high voltage multiplexer board populated with solid state switches is shown on the right; it is capable of running 42 channels to +/- 500 V.	70
6.4	Traces showing time-varying high-voltage input (heavy, black) and multiple actuator channels (light, colored) with a steady quasi-DC level. Channel decay between refresh points is exaggerated for illustration purposes.	71
6.5	Definition of actuator numbers for 16-channel prototype.	72
6.6	Influence functions of preliminary 100-mm mirror prototype with 16 channels with the pattern in Figure 6.5. (a) experimental measurements and (b) finite element predictions due to 400-V inputs. Deflection color scale is in units of waves at 633 nm. The diameter of the images is only 75 mm, due to objective lens size constraints.	73
6.7	Numbering definition of unique actuators for 41-channel prototype used in Figure 6.8.	74
6.8	Side-by-side comparisons of the 6 unique influence functions in the 41-channel actuation pattern as measured (left side) and as simulated (right side). (a)-(f) correspond to labels 1-6, as shown in Figure 6.7. Units are micrometers.	75
6.9	Comparisons of the Zernike components of the 6 unique influence functions in the 41-channel actuation pattern as measured (blue columns) and as simulated (red columns). (a)-(f) correspond to labels 1-6 as shown in Figure 6.7. Units are micrometers.	76
6.10	Demonstration of defocus control using a single input voltage.	77
6.11	(a) Reduction of static RMS shape error using 16 channels and (b) evolution of channel voltages.	78
7.1	Design chosen for performance analysis. See text for layer descriptions.	80
7.2	Axisymmetric vibrational modes of the deformable mirror. Scaled for a unity inner product over mirror disk.	85
7.3	Measured impulse response of mirror in time and frequency domains (upper plots). Three single DOF vibration models were fitted to the data to reconstruct the behavior and extract modal damping estimates (lower plots).	86
7.4	Representative random acoustic noise estimated from Delta IV launch environment specification.	87
7.5	Mirror vibration transfer functions for first three modes. Also shown is the spectrum of the acoustic loading.	88
7.6	Mirror center deflection due to vibration input for the first three modes. The first mode dominates the response.	89

7.7	Time histories of piston, tip, and tilt accelerations used as imposed boundary conditions in mirror jitter model.	92
7.8	Simulated spot image blurring due to mirror jitter from reaction wheel vibrations with constant exposure times.	93
7.9	Simulated spot image blurring due to mirror jitter from reaction wheel vibrations with adjusted exposure times.	94
7.10	AAReST mission concept illustration.	96
7.11	AAReST mission optical design layout.	97
7.12	Flowchart showing how the telescope performance Monte Carlo model runs using three software packages: Abaqus, MATLAB, and Code V.	101
7.13	Example trial in the Monte Carlo system performance analysis.	102
7.14	Telescope wavefront control performance, as measured by the Shack-Hartmann, of the (a) compact and (b) wide configurations for different cases of Shack-Hartmann sampling and mirror voltage limits. The reference wavelength is 540 nm.	103
7.15	Telescope geometric spot diameter, using 80% encircled energy criteria, of the (a) compact and (b) wide configurations for different cases of Shack-Hartmann sampling and mirror voltage limits. The reference wavelength is 540 nm.	104
7.16	Summary of the wavefront and spot size performance distributions of the (a) compact and (b) wide configurations for different cases of Shack-Hartmann sampling and mirror voltage limits. The reference wavelength is 540 nm, and the error bars indicate one standard deviation of the distributions.	105

List of Tables

2.1	Candidate active materials with order of magnitude performance values.	10
2.2	Candidate materials for mirror substrates.	12
3.1	Summary of mirror layers.	20
4.1	Schott D263® borosilicate glass properties. Values taken from various sources [31, 37, 5].	30
5.1	Material properties.	55
7.1	Acoustic vibration model parameters.	85
7.2	Optical prescriptions for the path to the Shack-Hartmann sensor. Dimensions are in mm. Negative thicknesses are due to the change of direction after reflection from the deformable mirror.	98
7.3	Optical prescriptions for the path to the imaging camera. Dimensions are in mm. Negative thicknesses are due to the change of direction after reflection from the deformable mirror.	99
7.4	AAReST performance modeling: injected errors range.	100

Chapter 1

Introduction

1.1 Motivation

Recent advances in mirror technologies have started a transformation in the architecture of space-based telescopes. Compare, for example, the monolithic primary mirror of the Hubble Space Telescope, with a diameter of 2.4 m and an areal density of $\approx 183 \text{ kg/m}^2$ [40], to the segmented aperture of the James Webb Space Telescope, with an overall diameter of 6.6 m and consisting of 18 lightweighted beryllium mirrors with an areal density of $\approx 20 \text{ kg/m}^2$ [13]. Two key advances that enabled this larger and much lighter aperture were the use of a folding architecture and the use of wavefront sensing and control (WFS&C) of the mirror surface error. The current state of the art in primary mirrors is the Active Hybrid Mirror (AHM) technology [14], with an areal density of $\approx 10 \text{ kg/m}^2$ and a wavefront correction capability on the order of $20 \mu\text{m}$, which sets the standard for further developments.

Further advances in technology are expected to enable even larger telescopes [23]. A study of large space apertures sponsored by the Keck Institute of Space Studies (KISS) [4], put forward the concept of forming large mosaic mirrors through on-orbit self-assembly of identical active mirror segments mounted on modular, low-cost spacecraft (“mirrorcraft”). An illustration of a large mirror being constructed in space is shown in Figure 1.1. The mirrorcraft would dock and mechanically link to each other, and the mirrors’ shapes would then be adjusted to form a single coherent surface.

1.2 Background

This section provides an overview of the two problems that formed the basis of the research in this thesis. The first is the problem of the architecture of the large primary mirror for a future space telescope. The second is a small scale technology demonstration toward which this research is geared and which is envisioned as a stepping stone to future architectures.

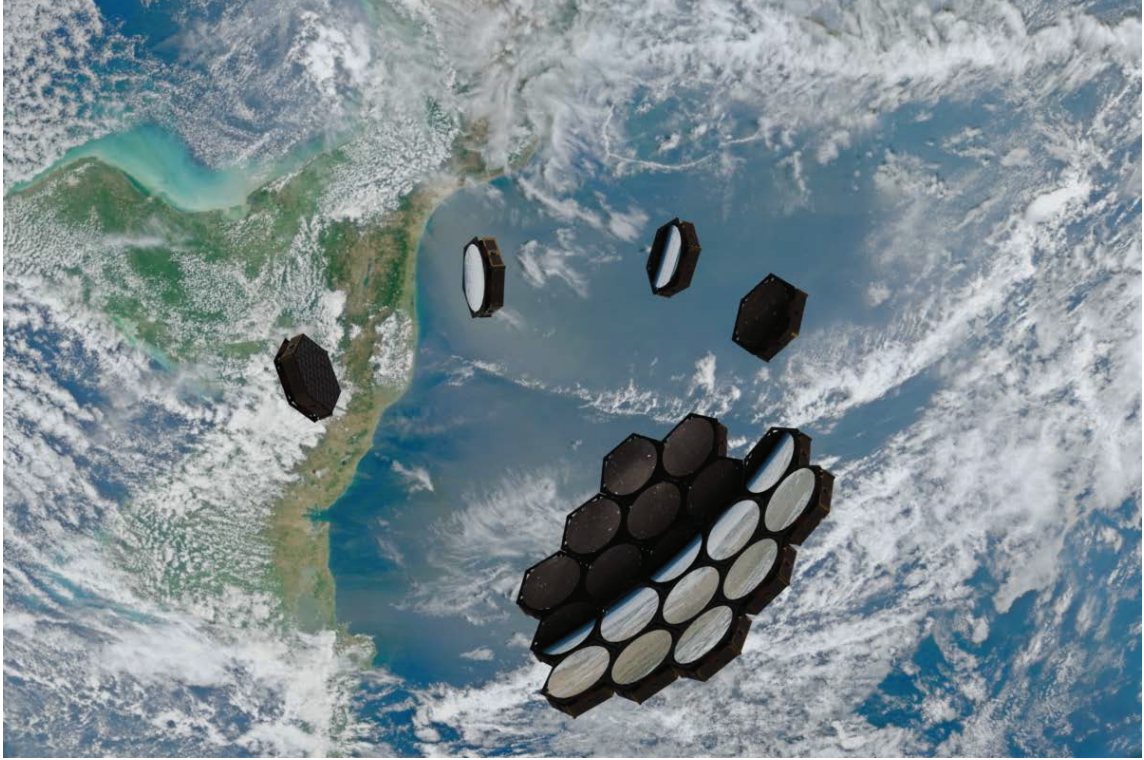


Figure 1.1: Concept illustration of a large segmented mirror being autonomously assembled in space.

1.2.1 Segmented Large Aperture Concept

A large mirror in space would necessarily be constructed out of segments, and to lower the costs of and add redundancy to the mirror segments, they would ideally be identical in manufacture. However, the manufacturing process is never perfect, and the only axisymmetric segmented mirror types that could be made from identical segments are flat and spherical. Most large reflecting telescope designs use a Cassegrain or Ritchey-Chretien layout which instead uses a parabolic or hyperbolic mirror. Therefore, it is best to think of these segments as nominally spherical in manufacture, but built with embedded active elements to allow for shape adjustment.

A previous study was done that investigated the performance of an example active segment design in a 10-m-diameter aperture [27]. The segments included actuators both embedded in the thin mirror, as well as around the edge for support. After optimizing the control solution, the shape errors between the base spherical shape and the desired paraboloidal shape were reduced by three orders of magnitude, as shown in Figure 1.2. This result was an encouragement for pursuing a demonstration of such mirrors, albeit on a smaller 10:1 scale.

1.2.2 AAReST Technology Demonstration Mission

The Autonomous Assembly and Reconfiguration of a Space Telescope (AAReST) mission is an endeavor to demonstrate key technologies for on-orbit telescope assembly and active mirrors using low-cost Cubesats. The latest telescope concept is shown in Figure 1.3. The telescope is a prime focus design (1.2-m focal length, 0.4° field-of-view) with the primary mirror divided up into a sparse aperture consisting of an arrangement of 10-cm-diameter circular mirrors. Two of the segments are active, and two are passive (rigid). The active mirror segments are attached to a cluster of Cubesats (mirrorsats), two of which are able to undock from the cluster and navigate independently.

The sensor package is deployed on the end of a foldable boom. It includes a detector at the image plane, lenses to reimaging the telescope entrance pupil, a Shack-Hartmann wavefront sensor, and a masking system to control any stray light from the telescope's open design. Using the wavefront sensor within the camera package for mirror shape information, the mirrors are adjusted and calibrated in order to minimize the size of the mirrors' individual point spread functions (PSF). Images are taken to demonstrate the ability of the mirrors to self-correct their shape, as well as the ability to re-point and correct the individual PSF's.

When the initial calibration and imaging demonstration is completed, the two active segments, which are carried by independent Cubesats equipped with propulsion systems, would detach from the mirror cluster, perform a maneuver to reposition themselves at a new location in the array, and then redock to the ends of the cluster. This would demonstrate in a limited manner the on-orbit assembly of mirror segments.

Once the cluster is again assembled, the mirror calibration and imaging would be performed again to show the capability of calibration in various configurations. To be successful, the new array positions of the mirrors would require them to be adjustable in order to achieve focused PSF's. To achieve diffraction-limited PSF's, the mirrors' surface accuracy must be controlled down to the order of fractions of the telescope's observational wavelength. For the visible band, this requirement is on the order of tens of nanometers. Hence, the mirrors have to be able to provide relatively large shape changes, or stroke, between different configurations, which is on the order of several microns, with an accuracy on the level of tens of nanometers.

1.2.3 Existing Deformable Mirror Technologies

There are several approaches for deforming mirrors by means of actuators. These approaches can be broadly divided into three categories, depending on the geometric arrangement of the actuators with respect to the mirror surface: (i) normal, (ii) parallel, and (iii) along the boundary of the mirror. Illustration of the various methods are shown in Figure 1.4. In case (i), known as *surface-normal actuation*, an array of stack or piston actuators push and pull on the mirror surface to produce local bumps and dips. In case (ii), known as *surface-parallel actuation*, actuators attached to a mirror facesheet bend the mirror. Case (iii), *boundary actuation*, applies forces and/or torques on the mirror rim to produce distortions of the mirror interior.

We expect that the future implementation of lighter and highly active space telescope systems will restrict the adoption of surface-normal actuation to smaller mirrors, typically the secondary or tertiary mirror of a telescope, whereas surface-parallel actuation will become established as the dominant lightweight solution for larger mirrors such as primary segments. A combination of surface normal and boundary actuation is also lightweight with the additional benefits of more shape control modes.

MEMS-based mirrors are well developed and are already implemented extensively in adaptive optics for ground telescopes, where they are employed in correcting atmospheric turbulence. Both surface-normal and surface-parallel actuation schemes have been developed. Deformable mirrors with diameters up to a few centimeters, hundreds to thousands of actuator channels and actuation strokes on the order of several micrometers based on MEMS technology are marketed by Boston Micromachines Corp. and OKO Technologies [25, 43]; silicon membrane mirrors actuated by PZT have been fabricated with silicon technology [46]. These types of devices are quite limited in the size of their clear apertures, and the required fabrication processes are not suitable for scaling these designs up to larger diameters.

Larger surface-normal actuation mirrors produced by Xinetics consist of PMN stacks attached to a mirror facesheet. The Xinetics standard PMN deformable mirrors have a diameter up to 241 mm, maximum deflection range of 4 micrometers and up to 941 actuators at a spacing of 7 mm [24]. The adaptive secondary mirrors on MMT, Magellan Baade Telescope and LBT use hundreds of surface-normal actuators [35].

Boundary actuation has been investigated in large thin, lightweight shell mirrors [22], and also in secondary telescope mirrors, where radial cantilever beams attached to the rim of a glass mirror were deflected by means of PZT actuators that impose a long-range deformation, while minimizing local dimpling effects for low-order modes [20].

Surface-parallel-actuation schemes have been studied extensively. Examples include PZT actuators laminated to glass or silicon substrates [41], piezoelectric strips or sheets bonded to the back of a thin shell [36, 19, 6], and schemes involving surface-parallel transducers integrated into the mirror structure [29]. Off-the-shelf deformable mirrors marketed by Cilas include a range of flat bimorph mirrors based on a symmetric arrangement of two glass plates enclosing two patterned piezoceramic plates; these mirrors have diameters up to 100 mm and 188 actuators that can provide a maximum curvature of 0.07 m^{-1} . Cilas also markets a range of unimorph mirrors, with diameters up to 115 mm and 63 actuators, that can provide a maximum defocusing correction of $20 \mu\text{m}$ peak-to-valley.

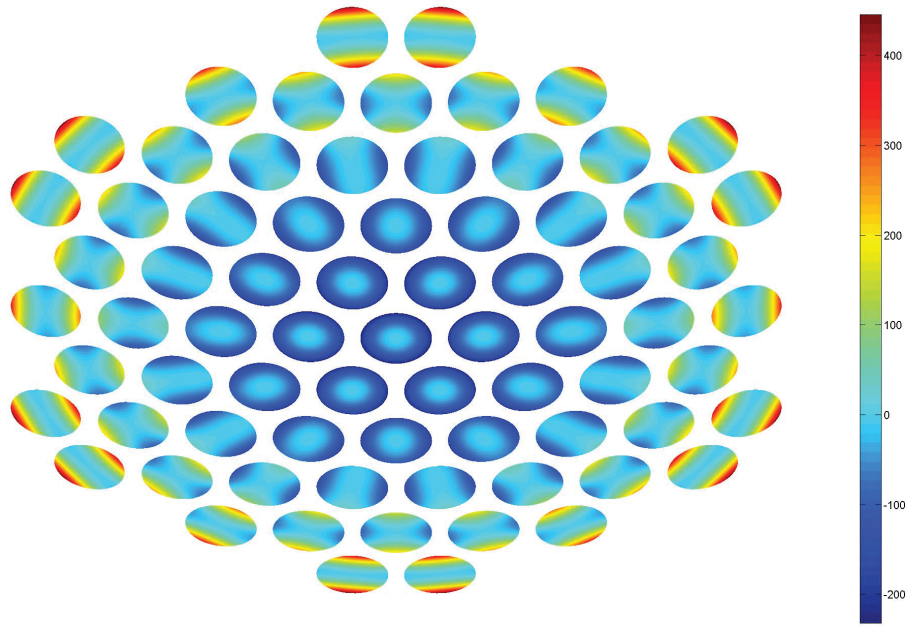
For the AHM technology, mentioned previously, the reflective surface is provided by a 10-to-100- μm -thick nanolaminate foil, bonded to a lightweight silicon carbide structure. Hundreds of electrostrictive actuators are embedded within the structure to make adjustments to the surface figure, in a form of surface-parallel actuation. Diameters up to 1 m have been demonstrated [14].

Extremely lightweight concepts have also been proposed for making mirrors from laminated polymer

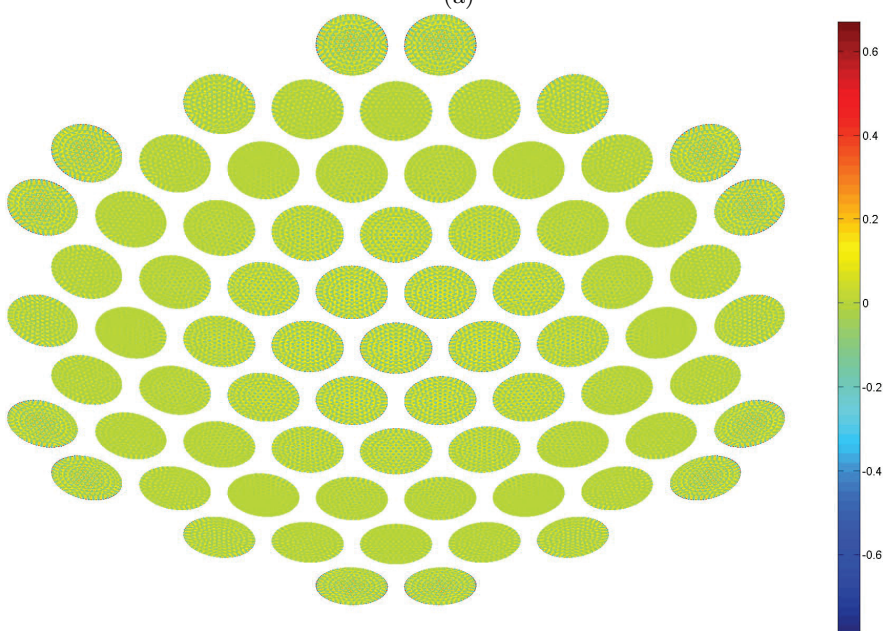
films [30, 1]. A review of processes aimed at minimizing surface roughness, thickness variation, and thermal expansion has been compiled by de Blonk et al. [9].

1.2.4 Need for New Technology

All of the reviewed technologies suffer from one or more deficiencies: either they are too heavy or complicated to be scaled up to large diameters, too expensive to manufacture, or have not yet demonstrated optical quality surfaces. The mirror design advocated in this research is one which takes advantage of the low mass of the surface parallel design, maintains good surface finish and figure, can be replicated from a master mandrel, has a simplified fabrication process, and is low cost.



(a)



(b)

Figure 1.2: An f/1, parabolic, 10-m-diameter mirror with 1-m-diameter identical, active, spherical segments. The colorbar displays the shape errors, in units of 633 nm wavelengths, of the segments (a) before, and (b) after correction.

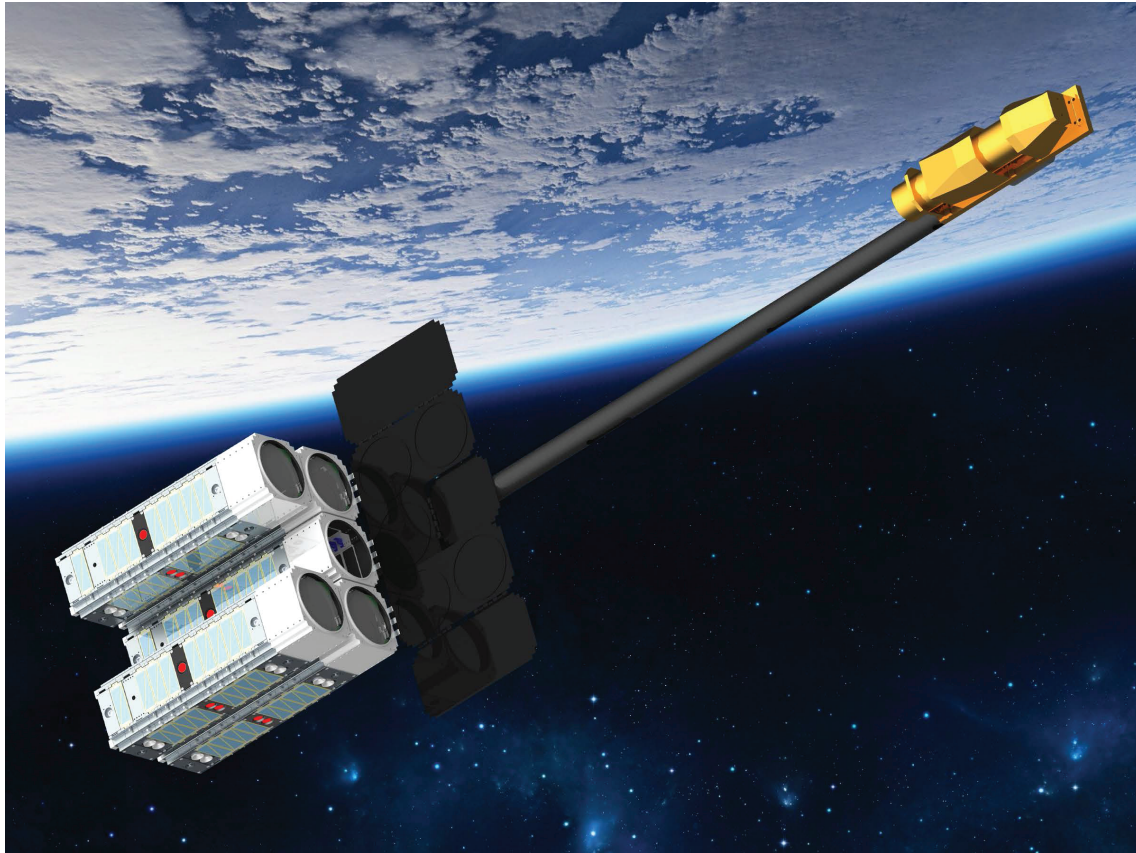


Figure 1.3: Rendering of the current design of the AARest telescope showing the four primary mirror segments mounted on mirrorcraft, deployed boom, and camera/wavefront sensor.

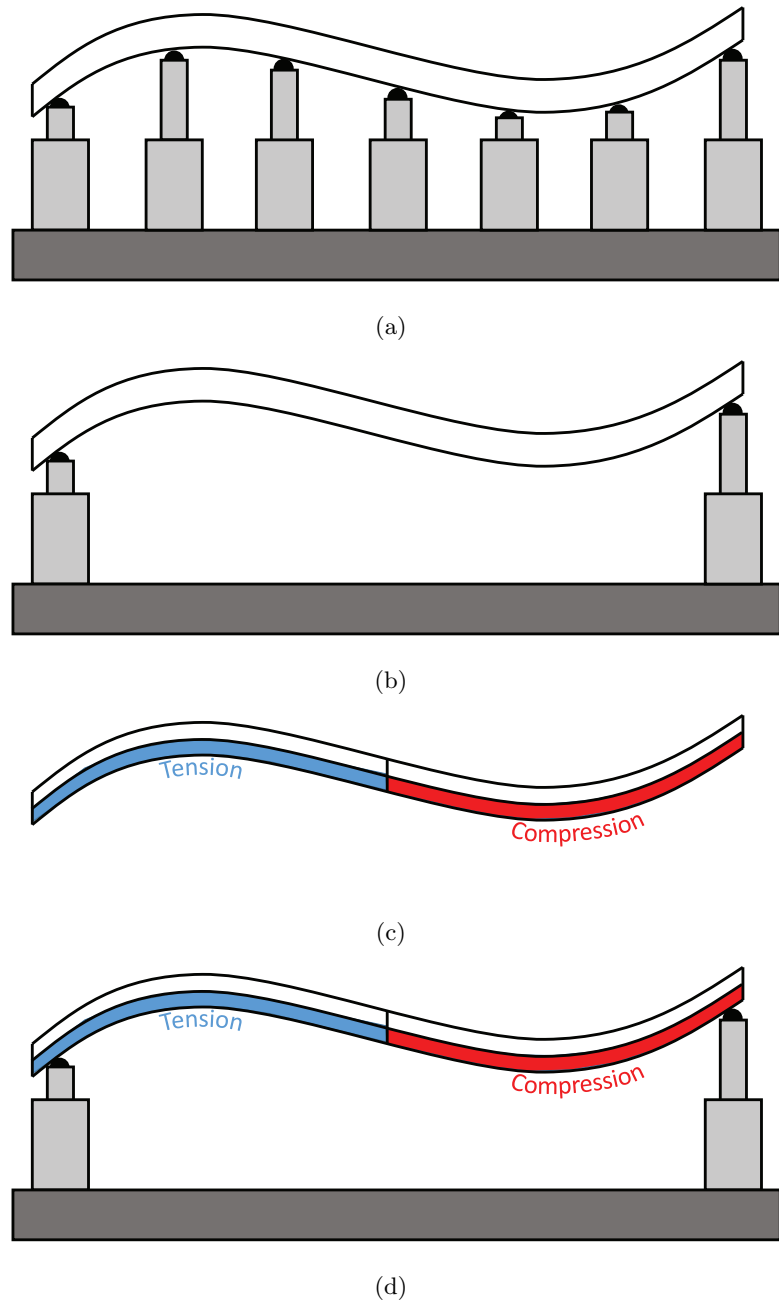


Figure 1.4: Four different ways of flexing a deformable mirror: (a) surface-normal, (b) boundary, (c) surface-parallel, and (d) boundary + surface-parallel actuation.

Chapter 2

Deformable Mirror Design Concept

The objective of this research is to develop a deformable mirror design that is lightweight, scalable, inexpensive, and with a sufficiently large shape correction dynamic range to allow the same base design to be used in many parts of a segmented aspheric mirror, and to compensate for thermally-induced optical perturbations along with material effects such as creep and aging. These requirements are to ensure economies of scale and simpler architectures in future large telescopes. This chapter discusses the design choices available for class of lightweight deformable mirrors based on a thin laminate design.

2.1 Laminate Concept

For lightness, the approach of choice is surface-parallel actuation; more specifically, laminated shell mirrors consisting of a stiff, thin layer with an optically smooth surface, with bonded active material layers. The active layers are coated with electrodes patterned in such a way that provides optimal control of the mirror figure. The most aggressive approach for lightness would be to make the whole mirror structure out of active materials including the substrate. This was pursued at the early stages of the present study, but was later abandoned due to the fragility of piezoceramic substrates, and the difficulty of fabricating quality piezopolymer thin shells.

A high stiffness substrate does provide the advantage of an increased bending stiffness that aids shape retention without complex mounting fixtures, and provides an initial shape for the mirror that is close to the desired optical figure. However, a disadvantage of this approach is that it decreases the actuators' range, or stroke, for shape adjustment. The substrate also aids in keeping the mirror thermally stable, by suppressing the thermal expansion of piezopolymer materials.

2.2 Active Materials

A list of active materials suitable for the actuation layer of a deformable mirror based on the present concept, in order of increasing maximum actuation strain, is presented in Table 2.1. The field that is used to control the actuation strain —electric, magnetic or temperature— is listed in the second column of the table and, since precise control can be achieved most easily for electric voltage, the research focused on piezoelectrics, both ceramics and polymers, and electrostrictives, and also dielectric elastomers. Two parameters that are used for the selection of actuators [16, 17] are the maximum actuation strain, i.e., the strain achieved by raising the control field to its highest safe value, and the blocked stress, i.e., the stress required to hold the material at zero strain overall while raising the control field to its highest safe value. The values of these parameters are listed in columns three and four.

Table 2.1: Candidate active materials with order of magnitude performance values.

	Piezoelectric Polymers	Electro-strictives	Magneto-strictives	Piezoelectric Ceramics	Shape Memory Alloys
Control Field	electric	electric	magnetic	electric	temperature
Examples	PVDF P(VDF-TrFE)	PMN, PLZT PMN-PT PLZT	Terfenol-D	PZT, BaTiO ₃ BaTiO ₃	Nitinol CuAlNi
Free Strain [%]	0.1	0.1	0.2	0.2	5
Blocked Stress [MPa]	5	100	70	100	200
Notes	low temperature processing	low hysteresis; needs voltage bias	needs large magnetic field	high temperature processing	large strains; slow

Electrostrictives and piezoceramics were ultimately not used in the final design, although they do provide large actuation stresses with good strain linearity, and low hysteresis in the case of some electrostrictives. Their fragility, high temperature processing, and cost made it more desirable to use piezopolymers instead. The issues related to fragility have been alleviated in the currently available MFC actuators based on piezoceramic fibers bonded with epoxy and prestressed in a polymer package [45]; however, these are discrete devices that may lead to print-through problems, and would also be difficult to integrate into a mirror concept that requires a large number of independent actuators. Thin coatings of ceramic actuator material do have potential for certain mirror applications, and are currently being developed by others [7]. However, the thickness of these coatings is currently constrained to a level of several micrometers or less.

Piezoelectric polymers are a reasonable compromise between performance and ease of processing, hence they were selected for the present study. Their primary drawbacks are relatively low blocked stress and

maximum actuation strain, but these issues can be addressed by designing a laminate with a sufficiently flexible passive layer. More specifically, the active material used in the present research was the copolymer of vinylidene fluoride and trifluoroethylene, P(VDF-TrFE). This material is a piezoelectric, semi-crystalline, thermoplastic fluoropolymer with similar properties to the homopolymer polyvinylidene fluoride, PVDF.

An extensive study has been done by Sandia National Labs [8] on the performance of PVDF and its copolymers under conditions similar to low earth orbit and including: temperature variation, UV exposure, atomic oxygen, and other effects. Subject to certain restrictions on the allowable temperature range to prevent loss of piezoelectricity, approximately -80°C to 90°C, and the need to shield against atomic oxygen, the study concluded that this polymer is suitable for space applications. It should also be noted that an instrument on the New Horizons mission to Pluto utilizes films of PVDF to count dust particle impacts on its journey towards the outer solar system by measuring currents in the film [15].

Diagrams of the chemical structure of the two polymers are shown in Figure 2.1. The homopolymer PVDF molecule is a long carbon chain covered by an equal ratio of hydrogen and fluorine atoms. In order for the material to behave as a piezoelectric actuator, the molecule should have a non-zero electric dipole moment, such that an applied electric field can reorient the dipole and induce mechanical strains into the material [8]. This is possible with PVDF and P(VDF-TrFE) due to the strong electronegativity of the fluorine atoms relative to the hydrogen atoms.

As shown in Figure 2.2, two possible arrangements or forms of the PVDF molecular chains are the α and β phases. The α phase is thermodynamically favorable; however, the fluorine and hydrogen atoms alternate on either side of the carbon chain, resulting in no overall electric dipole moment. In contrast, the β phase is arranged so that the two atoms are separated on opposing sides of the chain. One way of coercing the material into the β phase is to mechanically stretch the film to straighten the polymer chains, and apply a large electric field across the film. However, this is not a very convenient processing technique for making deformable mirrors. Another way to get the beta phase is to introduce defects into the polymer chain. By using a 3-fluorine, 1-hydrogen TrFE monomer unit in place of some of the VDF units, the beta phase becomes more favorable even without stretching. The high electric field is still required, however. The material used in this research was 75:25 mol % VDF:TrFE SolvaneTM purchased from Solvay Solexis.

2.3 Substrate Selection

The substrate should have high extensional stiffness yet low bending stiffness to maximize the range of curvature changes that can be achieved for any given active material. Hence, the material used for the substrate should be stiff, manufacturable in small thicknesses, and with low surface roughness. Alternately, it should be a material that can be polished to an optical-quality finish and will retain this finish in a space environment. Ideally, it would also have low density to reduce the overall mass of the mirror, high thermal

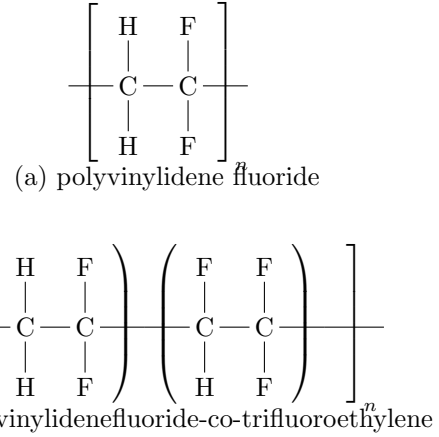


Figure 2.1: Electro-active polymers: (a) PVDF copolymer, and (b) P(VDF-TrFE) copolymer.

conductivity to prevent thermal gradients from distorting the shape, and be durable enough for handling and processing purposes. The surface roughness desired for optical wavelength mirrors is on the order of a few nanometers or less. Table 2.2 provides a list of several potentially suitable materials.

Table 2.2: Candidate materials for mirror substrates.

Material	Type	Notes
Si (single crystal)	ceramic	benefits from existing fabrication technologies; readily available; limited diameters but increasing over time
SiC	ceramic	very stiff; can be made to any size
Glass (FS, BK7, borosilicate, Zerodur, etc.)	ceramic	traditional mirror material; new flexible electronics display glasses could be suitable
Carbon fiber composites	polymer	low thermal expansion; scalable using tape dispensing techniques; surface roughness is open concern
Al, Be	metal	ductile and easy to machine; low thermal stability; beryllium is toxic.

The required thickness of the mirror will primarily depend on the actuation stroke. Assuming that the actuation layer is much thinner than the substrate, the curvature change, κ , can be estimated with Stoney's formula [42],

$$\kappa = \frac{6\epsilon_a M_a t_a}{t_s^2 M_s} = \frac{6\sigma_a t_a}{t_s^2 M_s}, \quad (2.1)$$

where ϵ_a is the free strain, t_s and t_a , and M_s and M_a are the thicknesses and the biaxial moduli of the substrate and actuator, respectively. For an isotropic material, the biaxial modulus is $E/1 - \nu$, where E is the Young's modulus, and ν is the Poisson's ratio. The (biaxial) blocked stress, $\sigma_a = \epsilon_a M_a$, may be used in place of the actuation strain, if preferred.

In order to increase κ without changing the blocked stress, the substrate thickness should be reduced

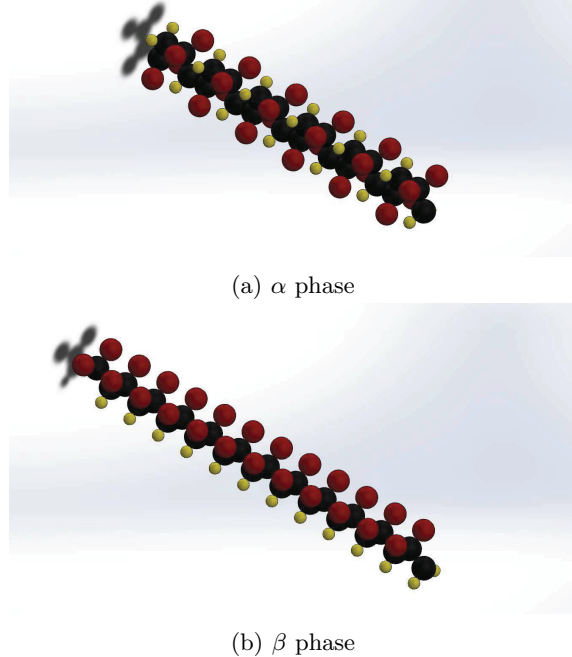


Figure 2.2: 3D model of two arrangements of the PVDF molecule. Black spheres represent carbon atoms, red spheres represent fluorine, and yellow spheres are hydrogen.

or a softer substrate be chosen. However, there are some practical limits. First, when it was attempted to construct whole mirrors out of layers of P(VDF-TrFE), it was found that the mirror would wrinkle (buckle) very easily unless it was held under a state of tension. Second, high modulus substrates that are too thin bend under self-weight and become distorted due to fabrication residual stresses. Packaging such low stiffness mirrors for launch is challenging, and the handling of thin substrates is very difficult during processing.

All of these effects can be analyzed with standard techniques, but a specific effect should be mentioned. In cases where the active material is poled after deposition onto the substrate, a residual poling strain, ϵ_p , will remain due to the permanent reorientation of the dipole domains. If the poling strain is too large, this residual strain can cause the substrate to buckle into a cylindrical mode. The minimum (critical) thickness at the onset of buckling of a circular plate of radius, R , is given by [11, 12]:

$$t_{crit} \approx \left(\frac{1.05\epsilon_p M_a t_a R^2}{M_s} \right)^{1/3}, \quad (2.2)$$

Note that there are other sources of residual strain beyond poling stresses, for example, coating processes and thermal cycling. All such effects can be treated in a similar manner.

Estimates of the actuation curvatures that can be achieved using a uniformly actuated, single layer of P(VDF-TrFE) with a thickness of 20 μm on substrates of arbitrary thickness has been obtained using Equation 2.1; the results have been plotted in Figure 2.3. The theoretical lower limit imposed by buckling

into a cylindrical mode, predicted by Equation 2.2, bounds the practical design space. Using this type of plot, an appropriate substrate material and thickness could be chosen based on a required actuation curvature and for a chosen active material.

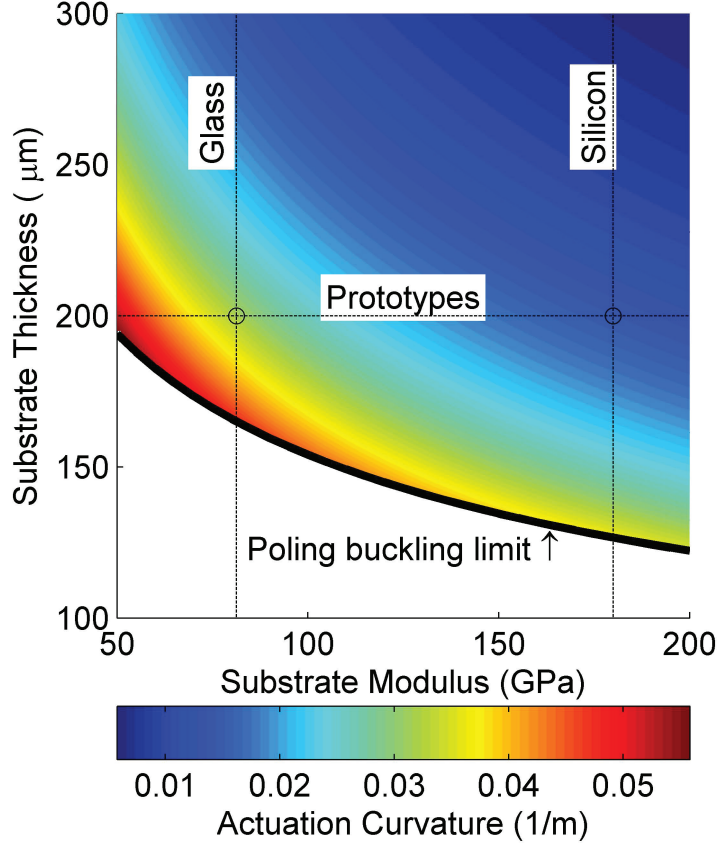


Figure 2.3: Estimated actuation capability of 20- μm -thick P(VDF-TrFE) coating as a function of substrate biaxial modulus and thickness. A practical lower limit is imposed by substrate buckling due to residual poling strain.

In order to use deformable mirrors in a primary aperture, it is desirable to introduce a base curvature to decrease the demand on the actuators. In the case of a low-cost telescope with a segmented primary mirror, identical spherical active segments with curvature equal to the average overall curvature of the aperture would be required [27]. For the case of AAReST, the required curvature is on the order of 0.4 m^{-1} , which is quite shallow, with a peak-to-valley height of about 0.5 mm for a 100-mm-diameter mirror.

The substrate ultimately chosen for this work is thin ($200 \mu\text{m}$) Schott D263 borosilicate sheet glass, although some earlier mirror samples were made using silicon substrates. D263 glass can be purchased in sheet form at low cost with excellent surface finish, and it has space heritage in X-ray telescopes [47, 48].

2.4 Design Summary

An exploded view of the layers of an example mirror design with the materials chosen for this research is shown in Figure 2.4. These mirrors are 100 mm in diameter, with a total thickness on the order of 0.25 mm. More details on each of the layers will be given in the following chapters.

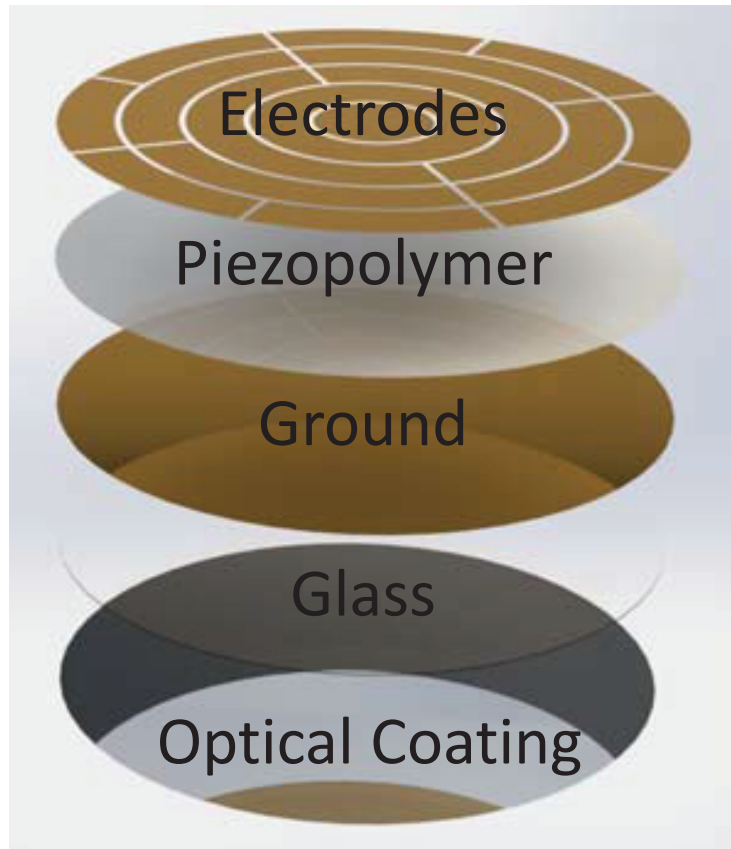


Figure 2.4: Layers of an ultra-lightweight deformable mirror.

Chapter 3

Deformable Mirror Fabrication

This chapter provides more detail on each of the layers and the methodology used to manufacture the mirror laminate.

3.1 Substrate Processing

3.1.1 Flat Substrates

Flat ground and polished silicon or glass wafers can be purchased in high volumes at low cost with figure errors on the level of a few microns or better; thus, typical arithmetic surface roughnesses are on the order of several nanometers or better. So flat wafers can typically be used in as-bought condition. For sheet glass, the figure errors can be worse, so these substrates may require slumping on a mold.

In order to improve the adhesion of the active layers on the backside of the mirrors, it can help to pre-roughen the substrate surface. With glass this can be accomplished by briefly exposing the surface to HF vapor for several minutes. For silicon, this can be done by stripping the native oxide surface layer (by dipping in HF, or by reactive ion etching (RIE)), and then exposing the surface to xenon difluoride vapor in a vacuum chamber.

The required substrate thickness is on the order of $200 \mu\text{m}$, which means that the samples can be damaged easily by mishandling. To avoid this, the samples were temporarily bonded onto a thick aluminum chuck using water soluble CrystalbondTM 555 wax during the processing. It also improves temperature uniformity across the sample during each of the processing steps and helps with process repeatability.

3.1.2 Curved Substrates

Glass or silicon wafers are excellent substrates for the mirrors; however, they are usually manufactured to be nominally flat. One way to introduce a permanent curvature into a nominally flat substrate is by applying a stressed coating to the substrate, e.g., by depositing coatings while either cooling or heating the substrate.

This works well up to a limit defined by Equation 2.2, after which the substrate will buckle from a spherical into a cylindrical shape [11]. To go beyond this limit, a boundary constraint could be used to hold the axisymmetric shape at higher levels of stress; however, this comes at the cost of a reduced actuation range.

An alternative approach, suitable for glass substrates, is to heat it above its glass transition temperature to the point where it will slump under its self-weight, as shown in Figures 3.1 and 3.2. This can be done on top of a polished mandrel in order to replicate the surface figure into the sheet glass substrate. This process, known as slumping, will cause the substrate to take the curvature of the mold without sacrificing the optically smooth surface finish of the original wafer. It was used for the mirrors of the NuSTAR X-ray telescope [47]. It has been demonstrated that under carefully controlled conditions silicon can be slumped as well, at around 900 °C [10]. Note that care must be taken to ensure that no dust is trapped between the sample and mandrel, otherwise defects will be present after slumping. Therefore, this process is best done in a cleanroom environment.

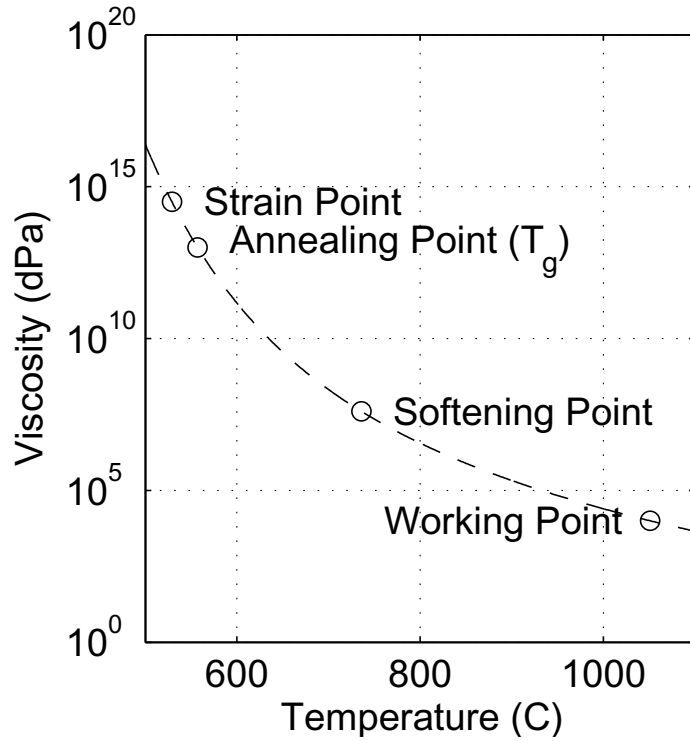


Figure 3.1: Estimated viscosity curve of Schott D263 glass using data reported by PGO [31]

A release layer is required between the mandrel and sample to prevent it from fusing at high temperature. Boron nitride spray coating has been used successfully in the past [47] due to its lubricity, softness, and chemical stability at high temperature in air. Sputtered platinum has also been used as a release layer

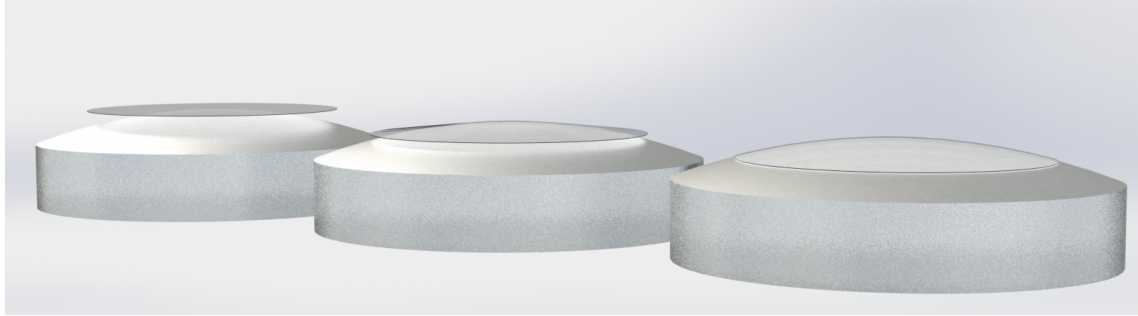


Figure 3.2: Illustration of slumping process. As the wafer is heated from left to right, it conforms to the mold shape.

due to its chemical inertness and reflectivity, which allows for optical measurements of the mandrel and/or sample [34].

For this work, 10-cm-diameter samples are slumped over a polished fused silica mandrel in a furnace at 580 °C and held there for 12 hours. The temperature ramp rates are 0.25 °C/min. RF-sputtered boron nitride is used as the release coating and applied to the mandrel. At the time of the writing of this thesis, the slumping process had not yet been optimized and more research into sputtered release layers is still needed.

3.2 Laminate Processing

Starting from either the silicon or glass substrate (wafer), the piezopolymer layer is spin-coated onto the wafer. P(VDF-TrFE) copolymer in powder form is dissolved overnight in cyclopentanone (20:80 by mass) to create a resin with reasonably high viscosity. If the viscosity is too high, it is difficult to spin-coat evenly, whereas a low viscosity produces layers that are too thin. This resin is poured onto the wafer surface, and the wafer is then rotated on a vacuum chuck for a set time and spin rate to produce a nearly uniform coating. The sample is then baked on a hot plate at about 130 °C or 140 °C for an hour to boil off the solvent and anneal the thermoplastic polymer. Copolymer film layers of 3 to 8 μm can be spin cast, depending on the final spin speed, as shown in Figure 3.3. This process is repeated multiple times to build up a film layer of the required thickness. The reason for building each active layer out of several thin coats is to reduce the effect of pinhole defects, as well as to attain thick enough layers for actuation purposes.

Each piezoelectric layer is coated on either side with a conductive film, formed by vacuum sputtering a metal such as aluminum, titanium, or gold. As an alternative to sputtering, thermal evaporation has also been investigated, but the latter process may cause the active layer to heat up, which could introduce damage. Therefore, sputtering is preferable whenever possible because it is a room temperature process. To avoid oxidation problems, the best metal is gold, but an intermediate layer of titanium or chromium is usually required to promote adhesion to the adjacent layers. Much care was needed to develop a successful

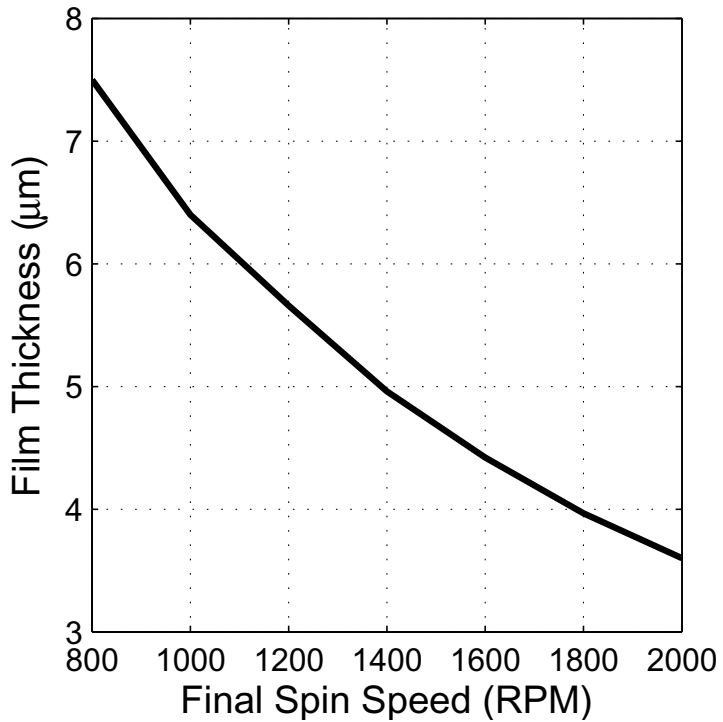


Figure 3.3: Typical film coating thicknesses for P(VDF-TrFE) (75:25 copolymer, by mol) dissolved in cyclopentanone solvent (80:20 copolymer to solvent, by mass). The resin was spread on the substrate at 500 RPM for 3 seconds before the final spin for 10 seconds.

process and avoid defects such as pinholes, cracking, and delamination. Patterning of the metal film is done by covering the film with a shadow mask during sputtering or evaporation; this works for simply connected geometries, but photolithographic techniques could be used for more complicated patterns. Note that shadow masks produce patterns with blurrier edges when sputtering, and so the mask should be placed as close as feasible to the substrate. For thermal evaporation this is less of a concern, since the deposition mostly occurs by line-of-sight.

After completing the mirror stack, it was necessary to change the state of the active material from paraelectric into piezoelectric. The method that was implemented consisted in directly applying a high-voltage potential across the top and bottom electrodes of the whole stack, although corona poling methods could be used as an alternative [8]. At field levels of 50 to 100 MV/m, the polymer used for the present study undergoes a transformation as local electric dipoles within the material align themselves to the external field. After removing the high voltage, the polymer is poled and thus ready to be actuated with lower voltages (approximately 25 MV/m). If there are pinhole or crack defects present in the laminate, the high voltage may cause arcing across the defect and permanent damage. Typically, the metallization around the defect

becomes vaporized due to local heating at the arc location, and the momentary electrical short is then re-opened. Actually, the laminate is still largely functional after this occurrence, albeit with a small defective spot. See Figure 3.4 for photos of an example mirror sample showing damaged spots after poling. A few possible ways of reducing the film defects include: elimination of dust contamination during the spin coating process, reducing tensile film stress, which can produce small cracks, filtering any particles out of the dissolved copolymer resin, and avoiding poling near the edge of the sample where film quality tends to be lower.

Note that the poling fields should be applied across the entire active layer, not just the patterned electrode regions. This prevents poling stresses in the form of the electrode pattern from printing into the mirror figure. This is achieved by depositing a thin, uniform coating of metal across the entire surface of the laminate, on top of the patterned electrodes, to act as a temporary poling electrode. A quick argon plasma etch after poling was then used to remove the uniform metal surface while leaving behind only the thicker metal pattern underneath.

A summary of the layer thicknesses and processing steps for a complete mirror laminate is presented in Table 3.1. Note that the reflective layer thickness can be increased to achieve thermal balance, as is discussed in more detail in the next section.

Table 3.1: Summary of mirror layers.

Position	Mirror layer	Material	Thickness (μm)	Order	Method(s)
1	reflective surface	Al, Ag, or Au	0.1	2	sputtering evaporation
2	substrate	Si or Glass	200	1	(slumping)
3	adhesion	Ti	0.01	3	sputtering evaporation
4	ground	Au	0.1	4	sputtering evaporation
5	adhesion	Ti	0.01	5	sputtering evaporation
6	active	P(VDF-TrFE)	20	6	spin coating
7	adhesion	Ti	0.01	7	sputtering evaporation
8	electrodes	Au	0.1	8	sputtering +ion mill

3.3 Mirror Coating

The choice of mirror coating depends on the application and the required reflectivity. Typical choices are silver, gold, and aluminum due to their generally high reflectivity. However, the reflectance of a metal depends on the incidence angle and wavelength of interest, and the analysis for computing it is covered in

this section.

3.3.1 Reflective Surface

The reflectance of a conducting (absorbing) metal in an ambient medium of index of refraction, n_1 , can be computed using its complex index of refraction, $n_2 - ik_2$, and polarization direction of the light by solving Maxwell's equations at the metal boundary. From Palik [26], the following equations can be used to find the reflectance, R_s and R_p , for S-polarized light (a wave whose electric field vector oscillates orthogonal to the plane of incidence) and P-polarized light (a wave whose electric field vector oscillates in the plane of incidence):

$$R_s = \frac{(n_1 \cos(\theta_1) - u_2)^2 + v_2^2}{(n_1 \cos(\theta_1) + u_2)^2 + v_2^2} \quad (3.1)$$

$$R_p = \frac{\left(n_2^2 - k_2^2 - \frac{u_2 n_1}{\cos(\theta_1)}\right)^2 + \left(2n_2 k_2 - \frac{v_2 n_1}{\cos(\theta_1)}\right)^2}{\left(n_2^2 - k_2^2 + \frac{u_2 n_1}{\cos(\theta_1)}\right)^2 + \left(2n_2 k_2 + \frac{v_2 n_1}{\cos(\theta_1)}\right)^2}. \quad (3.2)$$

Here the incidence angle, or the angle between the incoming light ray and the surface normal, is denoted as θ_1 . The placeholder quantities u_2 and v_2 are computed from the following equations:

$$u_2^2 - v_2^2 = n_2^2 - k_2^2 - n_1^2 \sin(\theta_1)^2 \quad (3.3)$$

$$2n_2 k_2 = 2u_2 v_2. \quad (3.4)$$

At normal incidence, i.e., $\cos(\theta_1) = 1$, the reflectance for both polarizations is equal. The normal incidence reflectance values for aluminum, silver, and gold are plotted in Figure 3.5. However, at oblique incidence angles small differences in reflectance can appear, as seen in the example curves of Figure 3.6. Depending on the telescope design and requirements, these small differences may require the active wavefront control system to handle different polarization states separately.

The choice of reflective coating for the mirror depends on the required spectrum. For visible light, aluminum has excellent reflectivity and is fairly flat over a wide wavelength range. Silver is also a good choice due to higher reflectance values, but may oxidize more readily than aluminum. Gold has excellent reflectance in the infrared, and does not oxidize like aluminum or silver. A layer of a transparent ceramic oxide can be coated over the reflective film in order to protect these soft metals from damage and to prevent oxidation in the case of aluminum or silver. The metallic coating thickness only needs to be a small fraction of the wavelength (e.g., around 100 nm for visible light) to be effective. However, the coating may be thickened

and tailor-designed for residual stress or thermal balancing purposes.

3.3.2 Thick Reflective Layer

Using a thicker coating for stress or thermal balance reasons can be tricky with Al, Ag, and Au due to their very low hardness in a pure (non-alloyed) state. The material may also plastically flow under stress at high temperatures, which can increase surface roughness and light scattering (giving the mirror a cloudier appearance), and reduce the signal-to-noise ratio in the telescope. Therefore, a harder metal such as chromium or nickel can be used for the bulk of the layer thickness, and then an overcoat of the more reflective metal can be placed on top. Another option is to constrain the grain-size growth of the soft coating by layering in a light coating of another material periodically, producing a kind of nanolaminate.

An example of this was done by alternating 500 nm of aluminum with 50 nm of chromium and comparing to a similar thickness wholly-aluminum film. The average biaxial film stress was measured from the wafer curvature. The samples were then heated on a hotplate, cooled, and measured again. This process was repeated several times at increasingly higher temperatures, and the samples were measured in between each cycle. The data is shown in Figure 3.7. The aluminum sample swung from a low compressive stress to a high tensile stress. The surface roughness also increased visibly by the end of the annealing cycles. In contrast, the mixed laminate with chromium was much more stable in stress, although there was still some plastic flow. However, the film did not produce the surface roughness like the other sample. Although it has not yet been attempted, it is expected that using thinner sublayers (e.g. 100 nm Al, 10 nm of Cr) would improve flow resistance even further.

Further discussion of laminate thermal balance is given in Section 4.3.1.

3.4 Kinematic Mounting

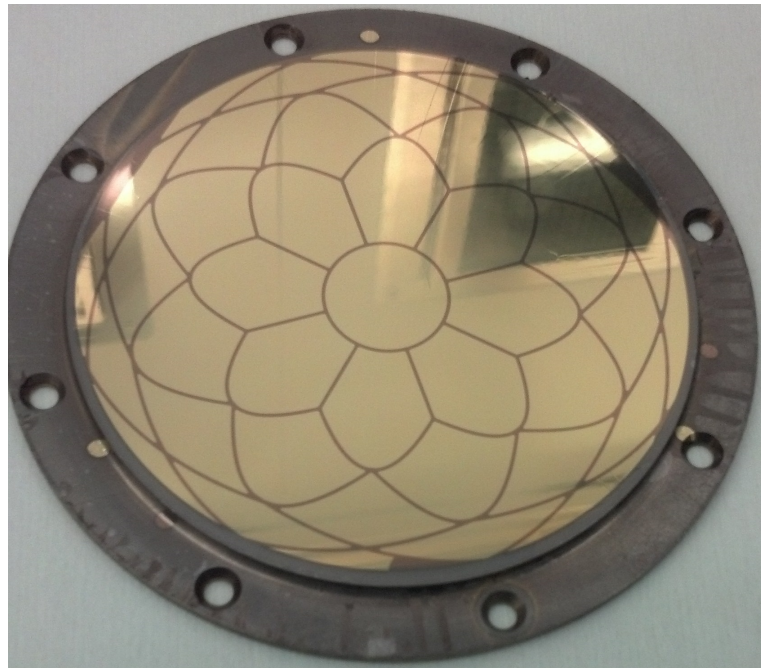
The surface-parallel actuation scheme adopted in the present study is well-suited for a kinematic mounting scheme, which mechanically constrains the six degrees-of-freedom (3 translations, 3 rotations) of the mirror without adding any additional constraints that may put the mirror in an unintended state of self-stress. This approach allows the flexible optic to deform itself into any desired shape, and hold its shape without being affected by the behavior of the mount. However, great care is needed in designing a kinematic mount for an ultra-thin plate/shell. For example, if mechanical flexures were employed to hold the mirror, any deformation introduced into the mirror by the flexures should have an amplitude on the order of optical wavelengths. Hence, the flexures would need to be designed to be so soft as to be unpractical.

A simple and effective scheme to hold the mirror has been devised, and it takes advantage of the large through-thickness stiffness of the mirror. Note that the mirror can be pinched without significant deflections

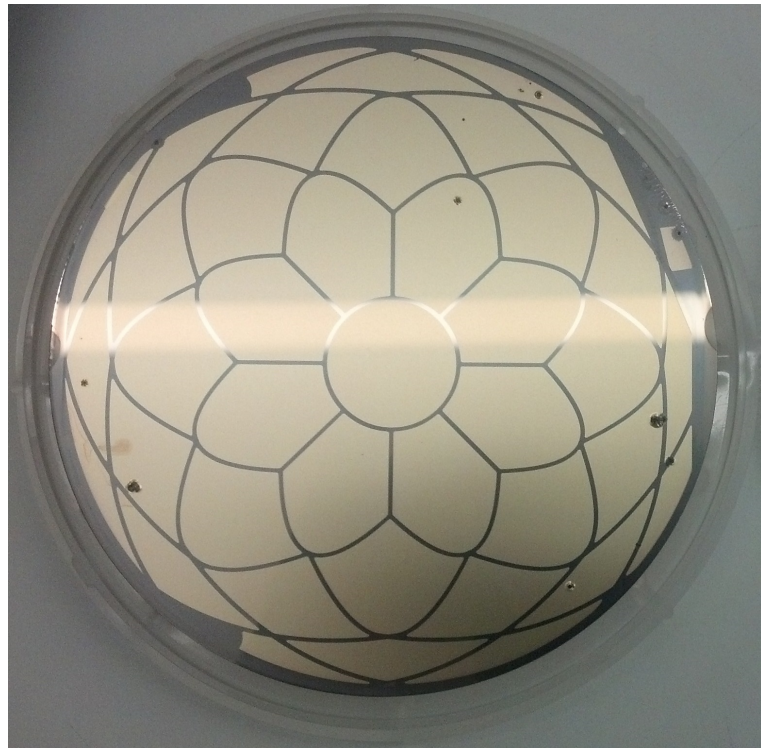
by applying equal and opposite forces on the front and back surfaces. The pinching forces need to be as close as possible to collinear, as any misalignment introduces shear and bending loads, which would induce significant deflections. Co-alignment could be achieved with machined parts that have tight tolerances, but a simpler approach is to use self-aligning magnetic forces.

Figure 3.8 shows an implementation of this scheme. The mirror is attached to a Printed Circuit Board (PCB) at three points, and at each of these points two polished, magnetized steel spheres pinch the mirror and hold it into place. The top sphere is unconstrained, and hence the magnetic field automatically aligns the upper and lower contact points. Additional constraints would need to be added to restrain the remaining three in-plane degrees of freedom (two translations, one rotation), but for the purpose of lab testing, friction at the pinched points is sufficient to hold the mirror in place.

Once the mirror is mounted on the PCB in this way, electrical connections are then made between the PCB and the mirror using very thin, pre-buckled wires made of soft, ductile metal such as gold or aluminum, bonded to the back of the mirror. The properties of these wires are such that any forces or moments applied to the mirror laminate are sufficiently small to leave the mirror figure unaffected. Resistive heating due to the narrow wire cross-section is not a concern because the wires carry only very short duration currents of microampere to milliampere levels. Figure 3.8 shows a schematic diagram of this connection scheme. Figure 3.9 shows photos of the front and back of an assembled mirror mounted on a tip/tilt gimbal.



(a)



(b)

Figure 3.4: Active laminate (a) before, and (b) after poling process. The thin laminate is wax bonded onto a chuck for processing. Small pinholes in the copolymer film can be seen; they were created by electrical discharges during the poling process due to coating imperfections. The electrode pattern shown on the sample was a result of design optimization work done by Dr. Marie Laslandes for the AAReST mission, and is described in a separate article [21].

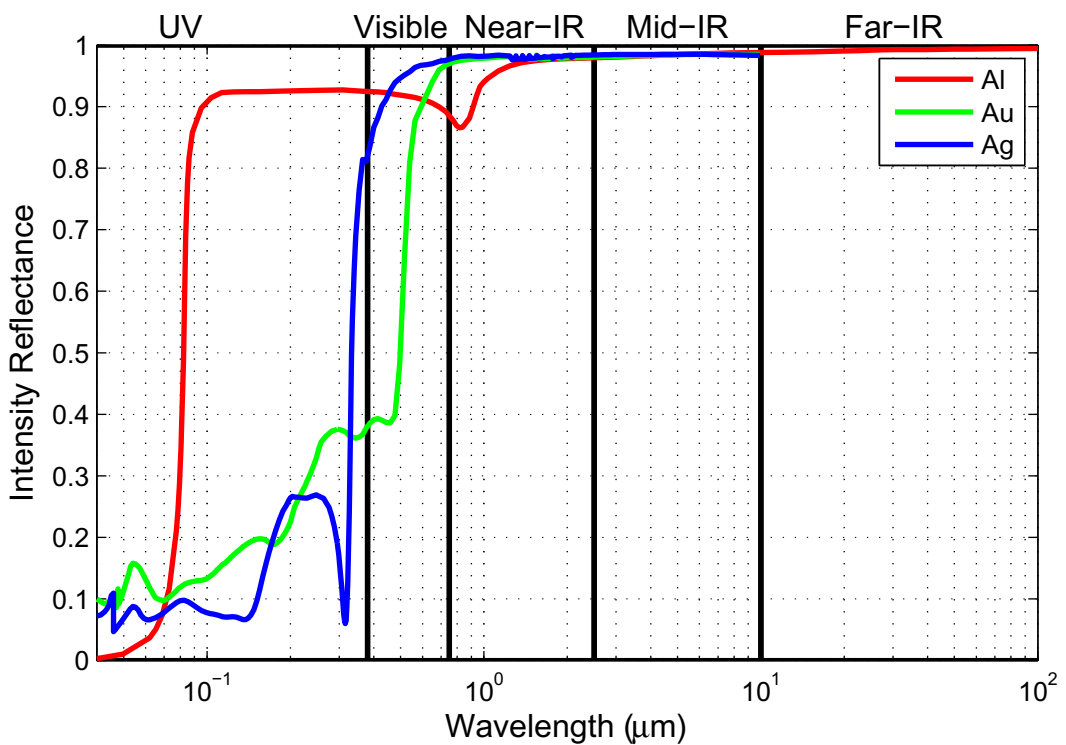


Figure 3.5: Normal incidence intensity reflectance of aluminum, gold, and silver as a function of wavelength. Computed from index of refraction data from Raki and Palik [32, 26].

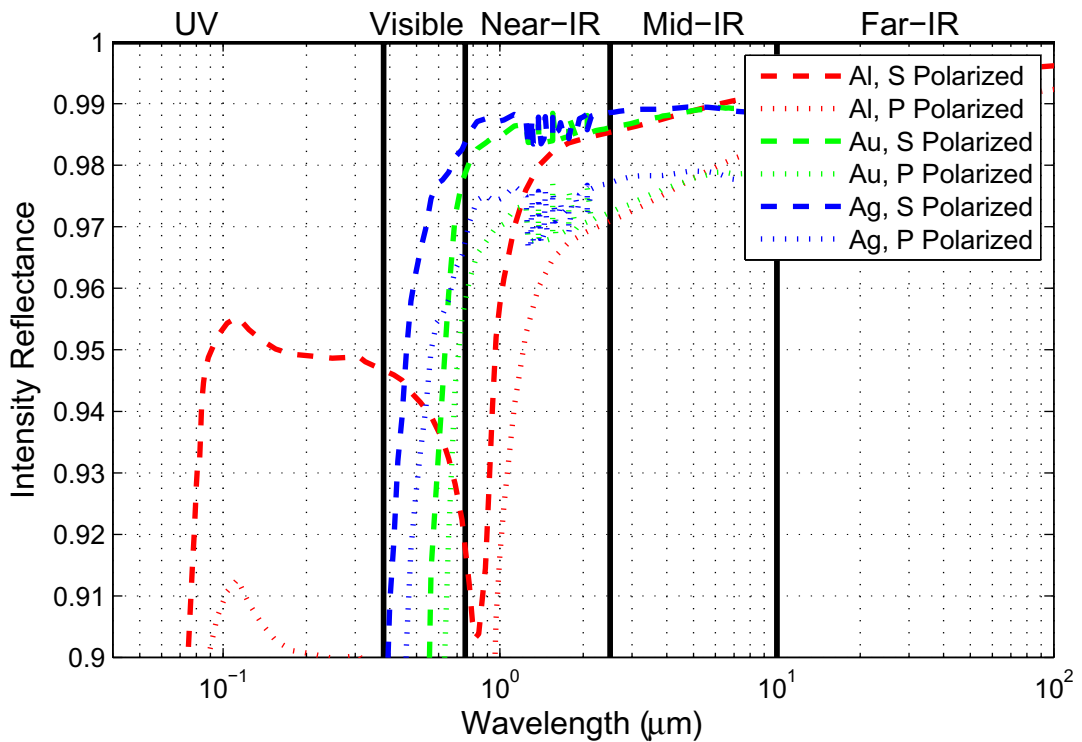


Figure 3.6: Intensity reflectance of S and P polarizations at an incidence angle of 45 degrees for aluminum, gold, and silver as a function of wavelength. Computed from index of refraction data from Raki and Palik [32, 26].

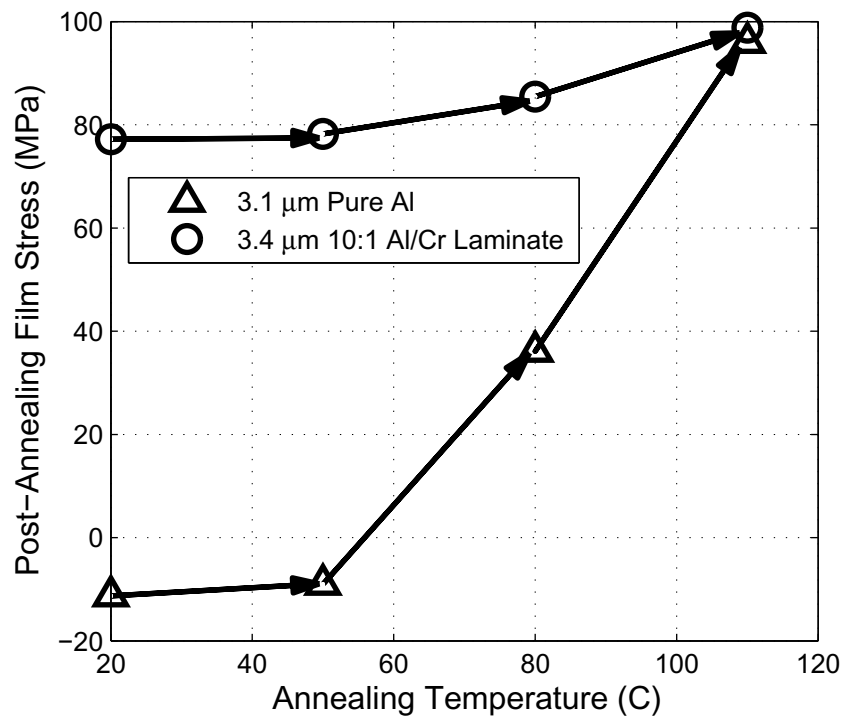


Figure 3.7: Comparison of annealing effects on film stress of thick coatings of pure aluminum vs. layered aluminum+chromium.

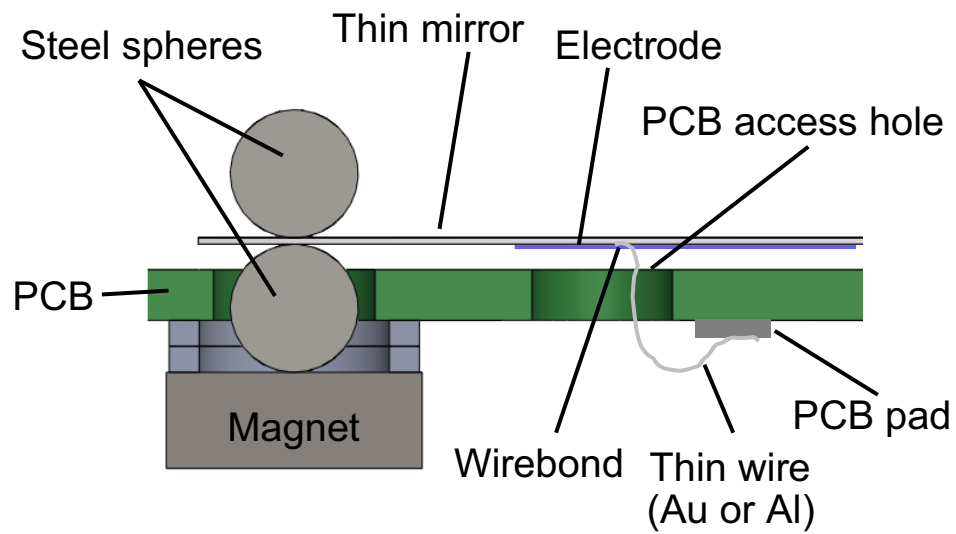
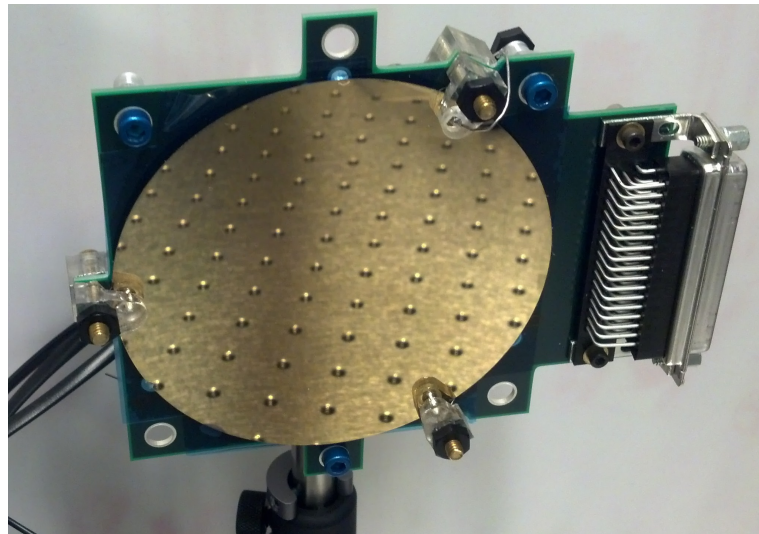
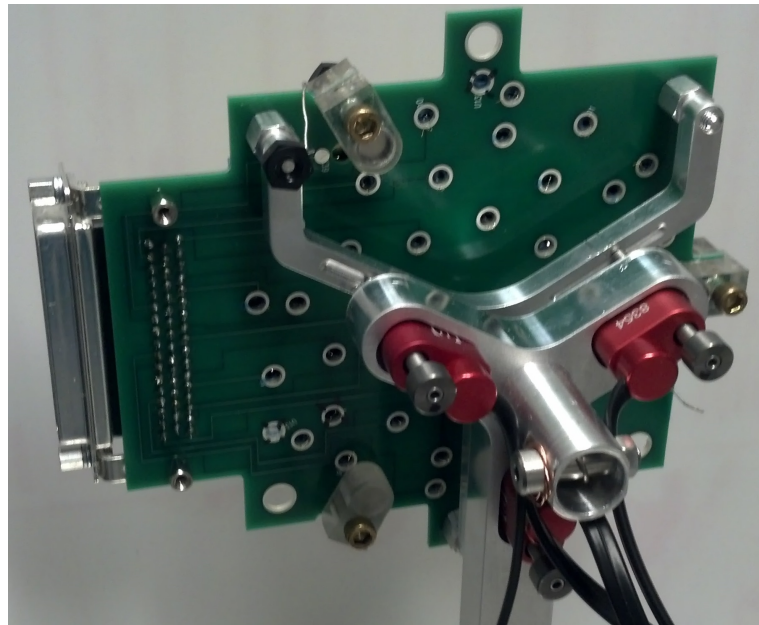


Figure 3.8: Cross-section of magnetic mounting scheme. Pairs of polished, magnetized spheres pinch the mirror at three places around the rim to hold it on a PCB. Tiny wire-bonded electrical connections jump from the board to the mirror.



(a)



(b)

Figure 3.9: (a) Front and (b) back of an assembled mirror prototype mounted on a custom-built 3-axis piston/tip/tilt gimbal.

Chapter 4

Material Behaviors

This chapter provides an overview of material properties and behaviors for the mirrors, with the emphasis on the piezopolymer active material.

4.1 Borosilicate Glass Properties

The relevant properties for the glass substrates are its viscosity for slumping, and its physical, mechanical, and thermal properties. Table 4.1 displays the important values needed for mirror design and analysis, and Figure 4.1 shows the glass viscosity temperature dependence.

Table 4.1: Schott D263[®] borosilicate glass properties. Values taken from various sources [31, 37, 5].

	Min	Max	Unit
Glass transition, T _g	557		°C
Thickness	0.2	0.25	mm
Density	2230	2510	kg/m ³
Elastic modulus	64	72.9	GPa
Poisson's ratio	0.2	0.208	

4.2 P(VDF-TrFE) Properties

This section details various piezoelectric, thermal, and mechanical behaviors of the copolymer film which may be important for laminate design depending on the specific application. The measurements were taken on 20-μm-thick film produced by spin coating the material on a stiff substrate, either silicon or glass.

4.2.1 Piezoelectric Behavior

A fresh or annealed copolymer sample will have dipoles that are randomly oriented and must be aligned together using a strong electric field in order to have a useful piezoelectric response. The critical electric

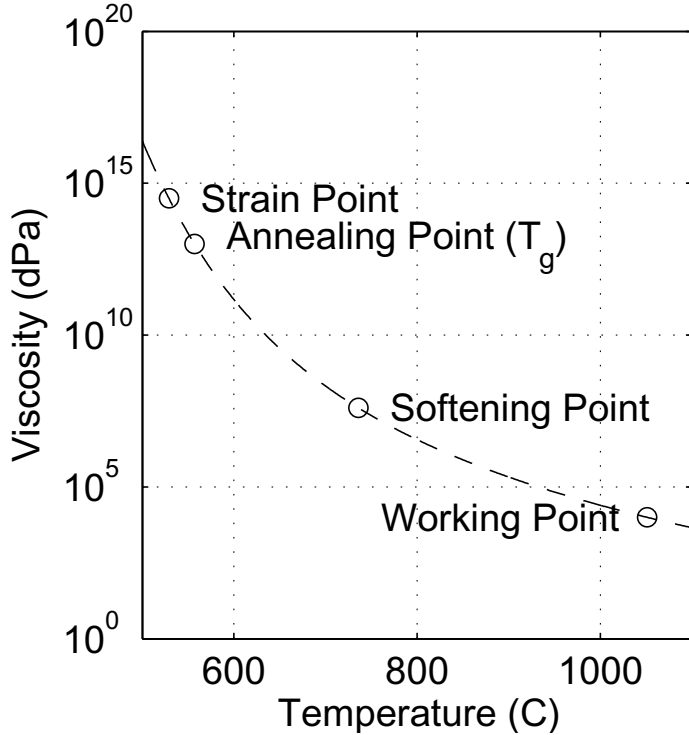


Figure 4.1: Estimated viscosity curve of Schott D263 glass using data reported by PGO [31].

field value is called the coercive or poling field. This field strength was found experimentally to be in the range of 25 to 75 MV/m; see Figure 4.2b. After the removal of the electric field, the material will retain a permanent polarization unless it is heated above its Curie temperature, above which the molecules have the mobility to randomly arrange their dipoles again. The Curie point was found using differential scanning calorimetry to be around 110 °C, although the transition zone may begin as low as 80 °C; see Figure 4.3a.

The retention of poling at high temperatures was verified using X-Ray Diffraction (XRD) analysis of the copolymer film on a single crystal silicon substrate for alignment purposes. Measurements were taken after deposition, after poling, and after annealing successively at 90 °C, 110 °C, and 130 °C for two hours each. The polymer peak of interest in the intensity data is located at a 2θ angle near 20 degrees. See Figure 4.4 for the smoothed intensity data with background levels removed. The peak is slightly shifted to the right for poled material, and slightly to the left for unpoled material. The peak location was mostly unaffected by the 90 °C anneal, but had almost completely reverted after annealing at 110 °C.

The mechanical behavior of the film during the poling process is shown in Figure 4.2a. The height of the bump, produced by the copolymer bending a small region on a 200- μ m-thick glass substrate, was measured (a surrogate for piezoelectric stress) while a large sinusoidal electric field was applied. The curve traces out a butterfly curve in which fairly straight linear regions can flip due to depoling behavior. When using the

copolymer as an active material, care needs to be taken to ensure that the material does not approach this depoling field. This means that the film should only be used in the range of -25 MV/m in the direction opposite to the poled direction, and up to around +75 MV/m in the direction of poling, depending on the dielectric breakdown strength, which is film-quality dependent. It should be noted that even when operating in the suggested linear region, there are still nonlinearities (hysteresis), as shown in a typical actuation loop shown in Figure 4.5. Larger electric fields, especially when approaching depoling, may result in larger amounts of hysteresis. The average linear slope of the curve can be used as the transverse piezoelectric coefficient, d_{31} , for linear modeling of the material in finite element analysis.

4.2.2 Thermal Behavior

The melting point of the material is in the neighborhood of 150 °C. A thermogravimetric analysis of a bare copolymer sample (see Figure 4.3b) in inert nitrogen atmosphere showed that the material has minimal moisture absorption and is chemically stable up to around 400 °C, beyond which it begins to undergo thermal decomposition.

The dependence of d_{31} on temperature for a similar P(VDF-TrFE) material has been reported by Dar-gaville et al [8]. The data has been replotted and shown in Figure 4.6. Note that the piezoelectric coefficient increases with higher temperatures; however, the usable piezoelectric actuation stress is tempered by a corresponding decrease in elastic stiffness, typical of thermoplastic materials, as seen in the dynamic mechanical analysis data (DMA) shown in Figure 4.7. The DMA test was conducted in a light tension mode on the bare copolymer film.

The thermal expansion of the bare material was measured using thermo-mechanical analysis (TMA) and is shown in Figure 4.8, along with the calculated coefficient of thermal expansion (CTE). The CTE generally increases with temperature just as the d_{31} coefficient. In fact, for electric field values of 25 MV/m, the magnitudes of the piezoelectric and thermal strains become comparable around temperature differentials on the order of only 10 °C. Therefore, if the copolymer is to be used in an application with significant temperature changes, the thermal expansion should be compensated in some manner so as to prevent taking up all piezoelectric stroke. Further discussion is given in the next section.

4.2.3 High Temperatures and Polarization

The retention of piezoelectric capability of the P(VDF-TrFE) film is important for use in extreme environments. Two experiments were carried out to determine the effects of thermal annealing on the film. The first involved measuring the electric polarization loop while the temperature of the material is slowly raised. The data can be seen plotted in Figure 4.9. It can be seen that at a temperature around 60°C, the combination of poling/depoling and high temperature causes a loss in total polarization that is not recovered when the

material is cooled back to room temperature.

Conversely, the material has shown to be quite stable after experiencing high temperatures as long as the large electric fields are not applied at the same time. Figure 4.10 shows the polarization loops when measured at room temperature after successive annealing cycles. The total polarization and the poling field values remain quite stable with only some small variations.

The results of these tests suggest that the P(VDF-TrFE) material may have limitations in usable electric field values at elevated temperatures. In other words, when used in an environment with varying temperatures, it may be prudent to restrict the allowable voltage range to low values when temperatures are higher than around 50°C, until the temperatures become lower again.

4.2.4 Time-Dependent Behaviors

The polymer exhibits several pertinent behaviors to its viscoelastic nature. There is the mechanical relaxation and creep of the material over time, as well as piezoelectric creep of the material under the constant application of voltage.

4.2.4.1 Viscoelastic Master Curve

Samples of the P(VDF-TrFE) copolymer film, 20 μm thick, were cyclically loaded under light tension at various temperatures and frequencies using a TA instruments DMA Q800 testing machine. The storage modulus, G' , and loss modulus, G'' , were recorded, and a viscoelastic master curve spanning many decades of frequencies was generated using time-temperature superposition at a reference temperature of 20°C. The master curves are plotted in Figure 4.11.

Due to the difficulty of directly taking the Fourier transform of the wide spanning data, various approximations reported by Schwarzl and Struik [38] were used to compute the relaxation modulus and the creep compliance. The various approximations are shown plotted in the time domains in Figures 4.12 and 4.13 with demarcations of convenient units of time.

4.2.4.2 Piezoelectric Creep

The application of an electric field to the constrained piezoelectric polymer will cause the material to build up stress. However, the material does not react instantaneously. While there is a near-instantaneous step response, which is usable even at very high frequencies (kHz), at low speeds the stress will continue to grow at a declining rate. An experiment was carried out on a test laminate where a square wave voltage was applied to electrodes on the laminate, and the average curvature was measured, see Figure 4.14. The raw data was fitted with exponential curves, and the relaxation times were measured. The average estimated

relaxation time from this test was approximately 2 minutes. It is therefore recommended that for the imaging application, the mirror be allowed to settle for a few minutes before beginning imaging.

4.2.4.3 Stress Annealing

One benefit of the viscoelastic nature of this material is the ability to anneal residual stresses in the material. An experiment was carried out in which a film was prepared on a stiff silicon substrate, and the stress in the copolymer film was measured using a Frontier Semiconductor film stress measurement (FSM) tool. The film was initially under a mild state of tension, and when poled produced a compressive stress due to the constrained expansion. By annealing the film at elevated temperatures for 5 minutes each and measuring the stress again at room temperature, it was observed that the film stress would eventually revert back to tensile. The maximum tensile stress occurred when annealing around the Curie temperature, and dropped again at higher temperatures until reaching a limiting value upon melting. The data is shown in Figure 4.15. In practice, the film should be annealed below the Curie temperature in order to prevent significant loss of polarization. For this simple experiment, it can be seen that a re-poling at the end again produced a sizeable compressive stress, implying that most of the polarization was lost after the exposure to high temperatures.

4.3 Laminate Properties

4.3.1 Laminate Thermal Balance

A laminate made of layers of different materials will, in general, bend when it is subjected to bulk temperature changes. Were the laminate layers symmetric in both thicknesses and materials on both sides of the substrate, then their thermal stresses would balance out, and the laminate would be neutral in bending due to temperature. In the specific application of deformable mirrors, a specular finish is required on the mirror front surface, and due to the tendency of the copolymer film to form rough free surfaces after deposition, it cannot be applied to the reflective side. Therefore, the effects of thermal bending are important and are discussed in this section.

Consider a laminate consisting of a substrate and any number of layers. Let α_s and α_i be the coefficients of thermal expansion of the substrate and the additional layers, respectively. It is assumed that all of the layers are much thinner than the substrate and hence a simple estimate for the bending curvature resulting from a temperature change, ΔT , can be constructed by substituting into Equation 4.1 the thermal strain relative to the substrate thermal strain, $\epsilon_i - \epsilon_s = (\alpha_i - \alpha_s)\Delta T$. Allowing for layers attached to both the top and the bottom of the substrate, the overall curvature can be obtained by superimposing their individual effects:

$$\kappa = \frac{6\epsilon_a M_a t_a}{t_s^2 M_s} = \frac{6\sigma_a t_a}{t_s^2 M_s} \quad (4.1)$$

$$\kappa = \sum_i \frac{6s_i (\epsilon_i - \epsilon_s) M_i t_i}{t_s^2 M_s} = \sum_i \frac{6s_i (\alpha_i - \alpha_s) \Delta T M_i t_i}{t_s^2 M_s} = \frac{6\Delta T}{t_s^2 M_s} \sum_i s_i (\alpha_i - \alpha_s) M_i t_i , \quad (4.2)$$

where $s_i = +1$ for a layer on top of the substrate, and $s_i = -1$ for a layer on the bottom.

Thermal bending can be nullified to some extent by means of additional coating layers that balance the laminate thermal stresses. To do this, set the curvature to zero and add additional layers (either on top or bottom) with appropriate thicknesses until the overall thermal curvature is zero:

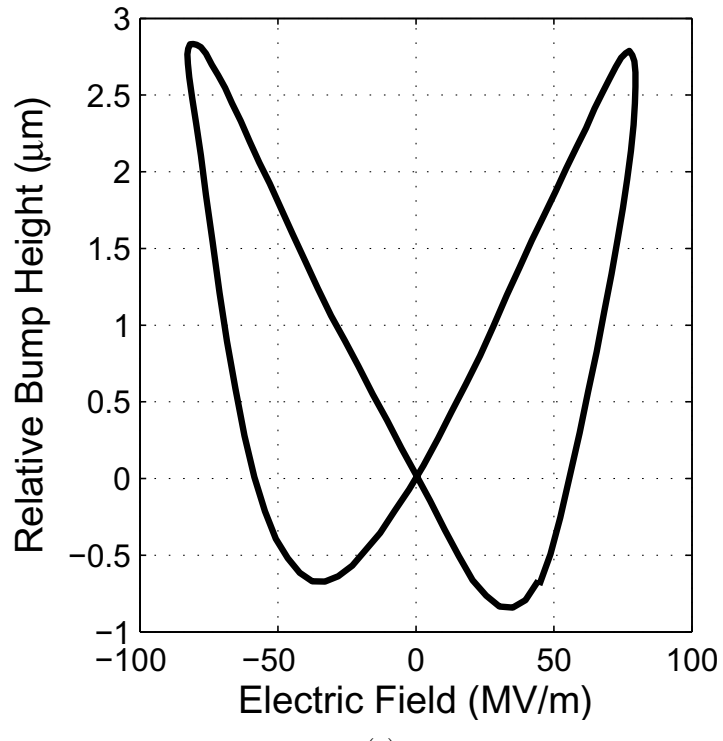
$$0 = \sum_i s_i (\alpha_i - \alpha_s) M_i t_i . \quad (4.3)$$

For example, a 200-μm-thick glass substrate coated with a 20-μm-thick layer of P(VDF-TrFE) can be balanced by means of several microns of a metal coating layer (such as Al or Ni) on the front. The use of a thick metal coating could potentially have large residual stresses, so mirror buckling should be avoided by controlling the substrate temperature during deposition to minimize the coating stress. The additional coating thickness required is small due to the higher stiffness of the metal coating relative to the polymer, and hence there is only a small increase in the bending stiffness of the mirror. Therefore, the corresponding reduction in actuation capability is small. Since a metallic coating is required anyway for reflectivity, then the thermal balance issue can simply be addressed by ensuring that the reflective coating has the thickness required to balance out the actuation layers. However, there is a limitation to this approach. Since the material properties of the polymer are not constant with temperature, a single metal balancing layer can only balance the laminate at a specific temperature. So the piezoelectric actuation needs to be used to control any residual bending due to changing material properties over the operating temperature range.

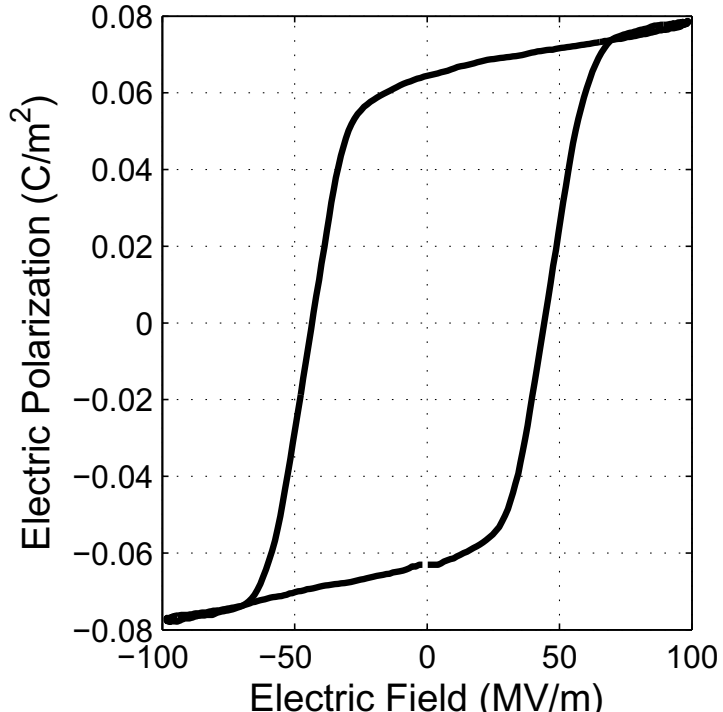
The thermal behavior of the laminate can be estimated using material properties reported in the previous section. Assuming a 20-μm copolymer film bonded to a 100-mm-diameter, 200-μm-thick borosilicate glass sheet, with an electric field limited between +/-25 MV/m, the out-of-plane bending actuation is shown in Figure 4.16a. As mentioned in the previous section, the opposing thermal trends of stiffness and piezoelectric coefficient tend to balance each other out. This creates a fairly large range of piezoelectric utility, from around -100°C to $+80^\circ\text{C}$, depending on the application. The optimal performance is estimated to occur around -40°C . However, the CTE mismatch between the substrate and copolymer film is substantial compared to the actuation range. In this case, the usable range of the laminate is quite limited, as illustrated in Figure 4.16b. The unbalanced laminate exceeds the piezoelectric stroke in less than 10°C .

To mitigate some portion of the thermal bending, the metallic reflective coating layer is then thickened to oppose the copolymer thermal stress. Assuming constant properties of the metallic coating over the displayed temperature range, the linear slope component of the unbalanced curve can be tuned by different choices of metal and thickness. An experiment was carried out over a limited temperature range where a mirror, coated by about $3\ \mu\text{m}$ of an alternating 10:1 aluminum chromium laminate, demonstrated the ability to partially balance the laminate, and is also shown in Figure 4.16b. However, the Al/Cr laminate coating ultimately did not have the same CTE as bulk aluminum (as was hoped), and so there was still a nonzero slope in the bending curve.

Further experimental investigation needs to be done regarding the optimal choice of material for thermal balancing. There are several things to consider, such as: initial deposition stress of the balancing layer, any nonlinearity in the metal behavior, as-deposited roughness of the metal, and ease and length of time of the coating process.

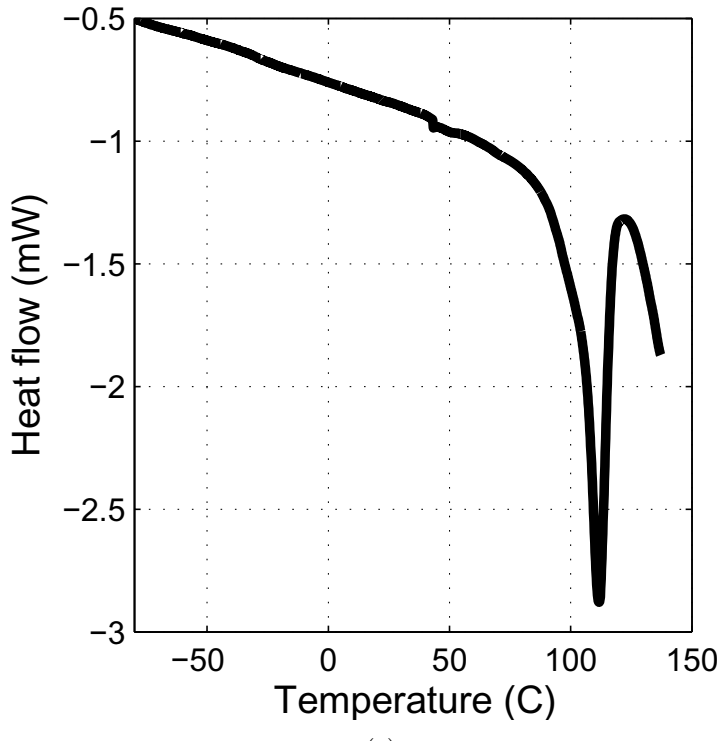


(a)

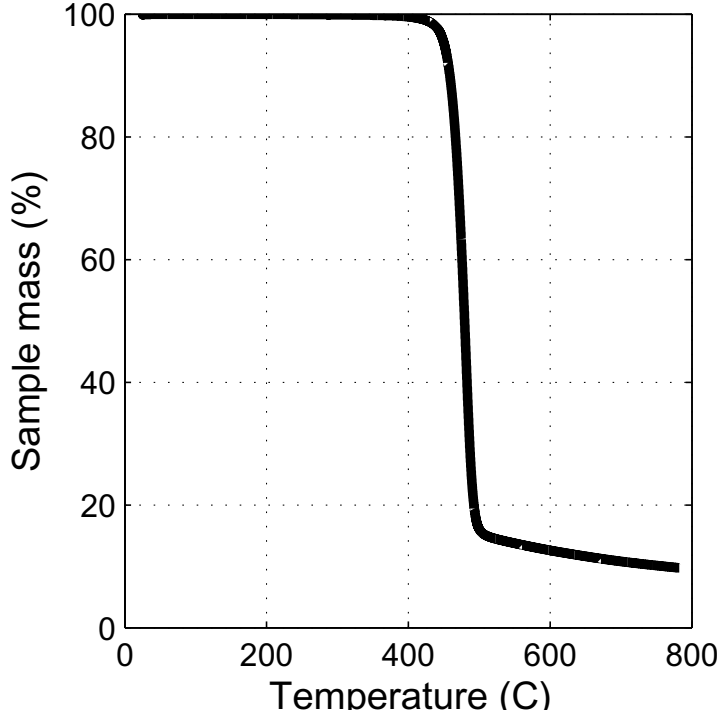


(b)

Figure 4.2: Copolymer response to poling cycles: (a) butterfly curves showing poling switching behavior, and (b) electric polarization.



(a)



(b)

Figure 4.3: Copolymer material test data: (a) Differential scanning calorimetry (DSC), and (b) Thermo-gravimetric analysis (TGA).

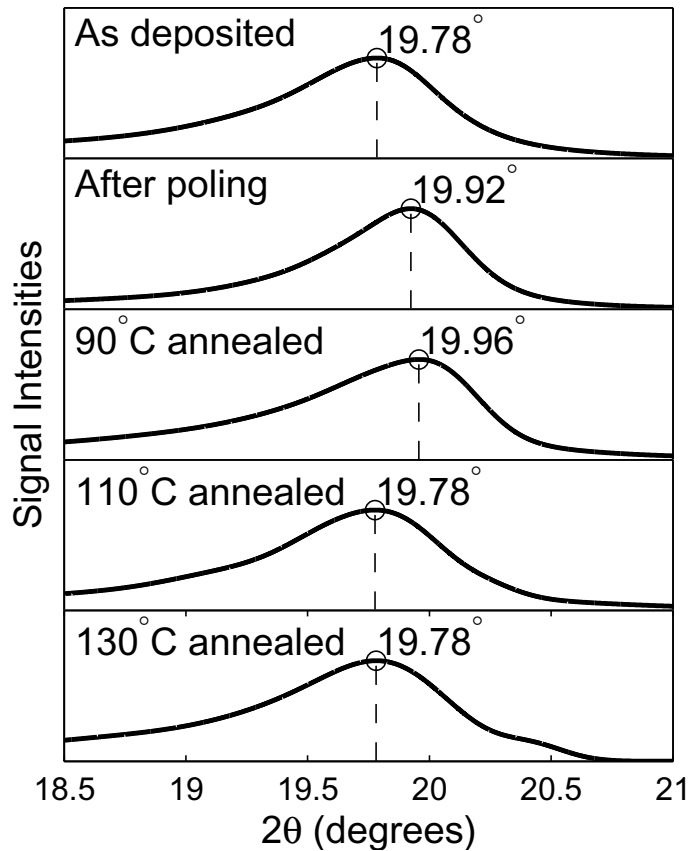


Figure 4.4: XRD response peaks of the P(VDF-TrFE) copolymer film. The peak shifts to the right after poling, and back to the left after annealing at or above the Curie temperature.

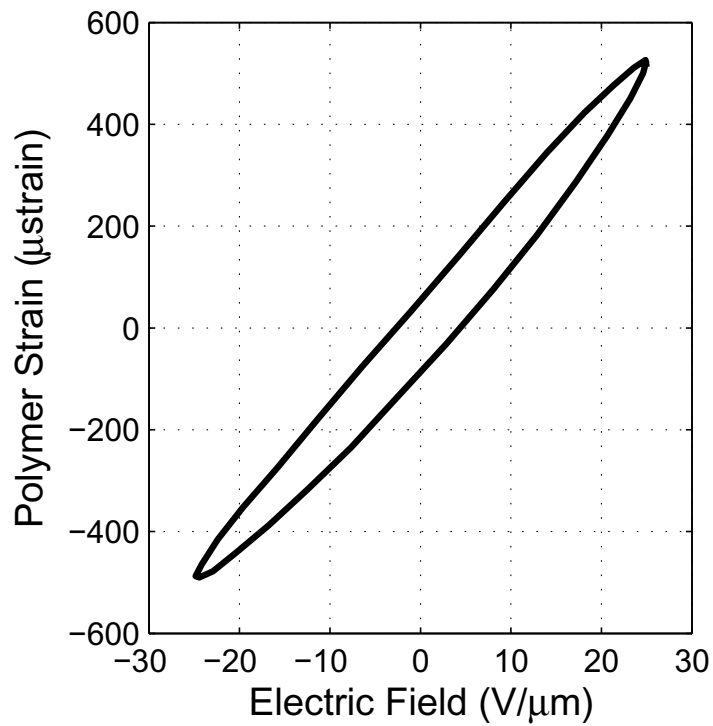


Figure 4.5: Typical actuation cycle of the copolymer in the quasi-linear region.

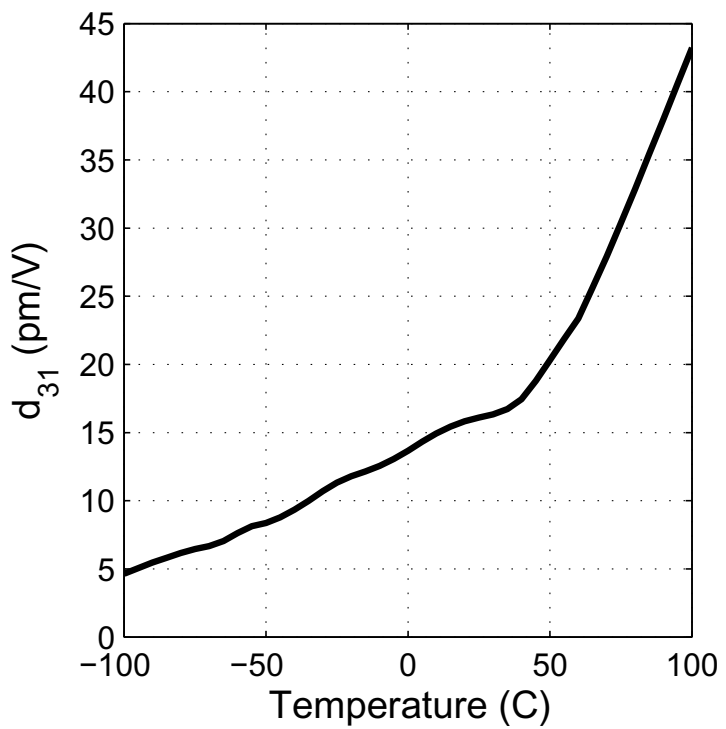


Figure 4.6: Piezoelectric coefficient temperature dependence of a similar P(VDF-TrFE) material as reported by Dargaville et al [8].

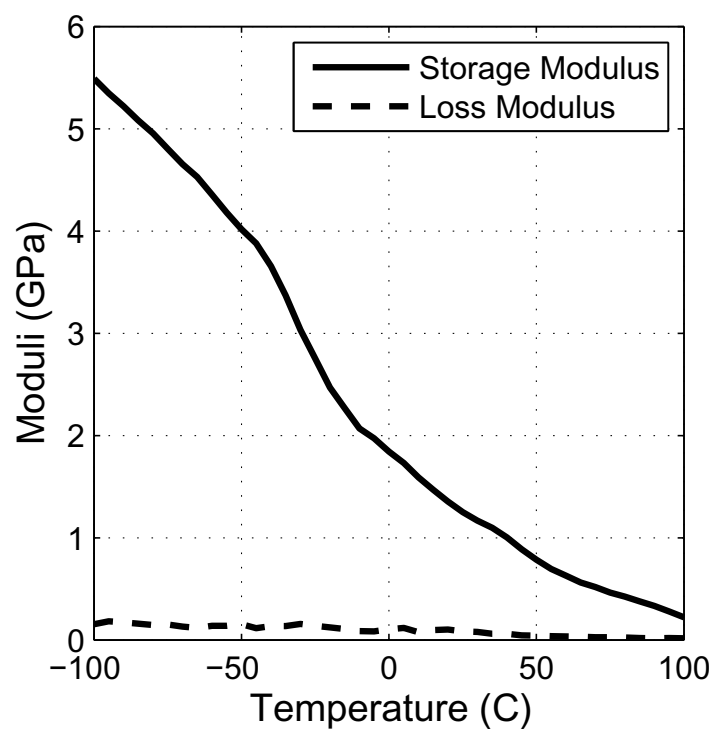
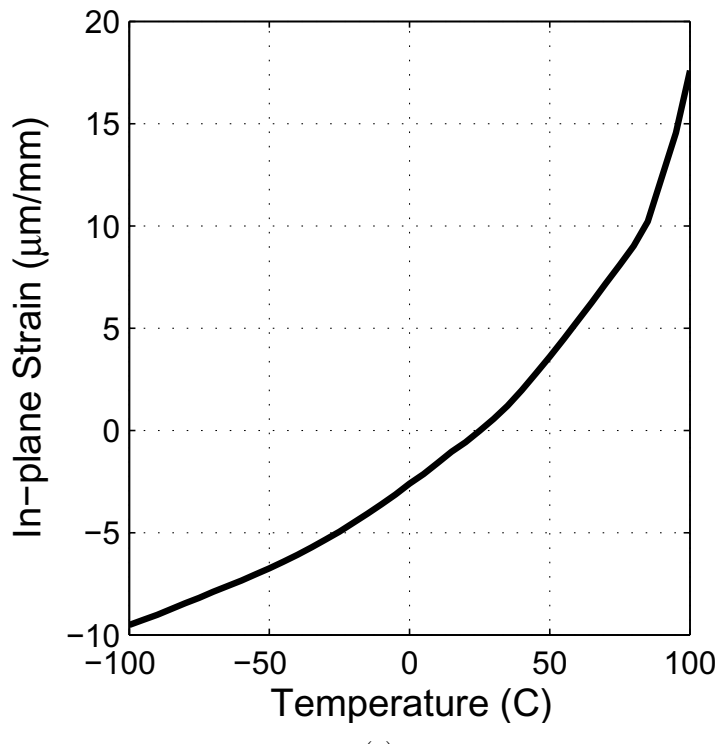
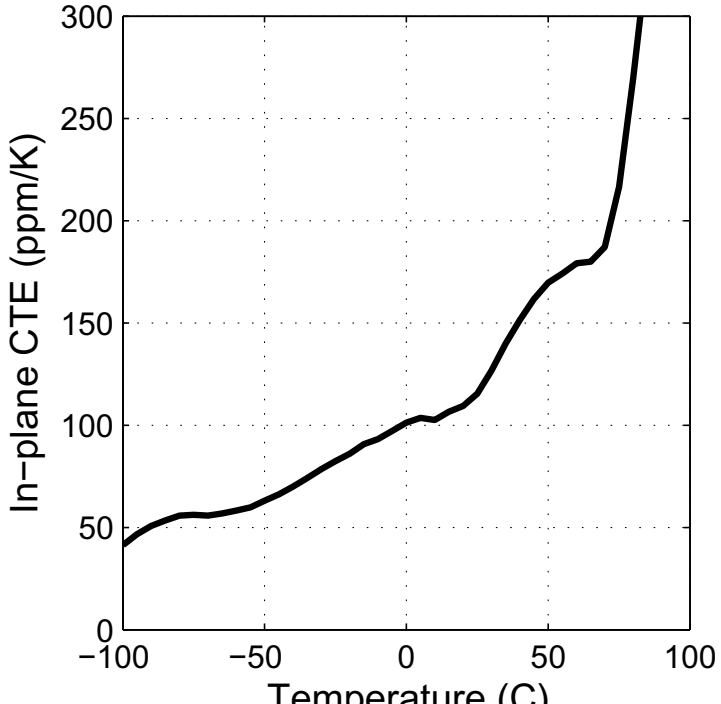


Figure 4.7: Loss and storage moduli for the copolymer thin film.



(a)



(b)

Figure 4.8: Copolymer material test data: (a) in-plane thermal expansion, and (b) CTE estimate.

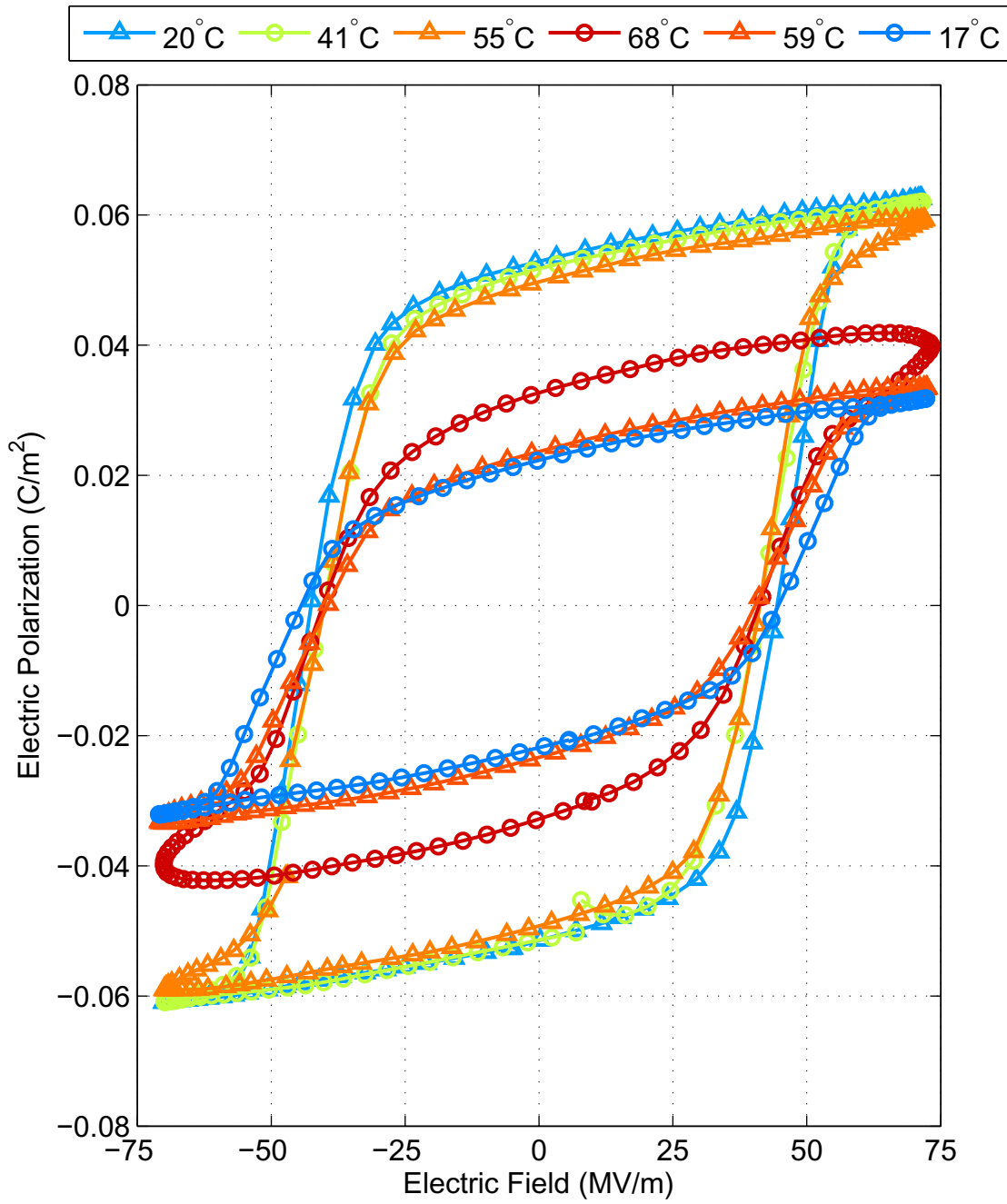


Figure 4.9: Loss of P(VDF-TrFE) piezoelectric capability due to elevated poling temperatures. The material sample was subjected to poling/depoling 0.1 Hz cycles continuously over several hours while the temperature was simultaneously raised to 68°C and then returned to room temperature.

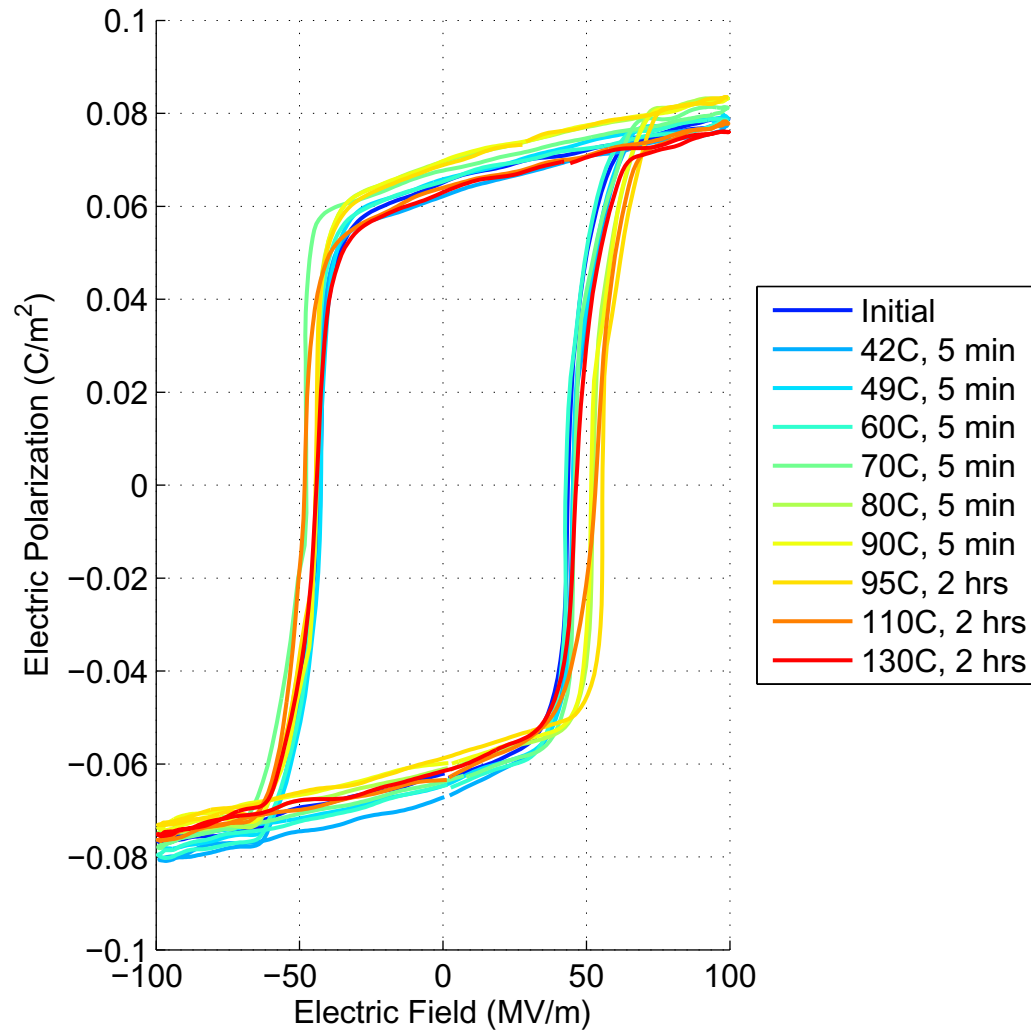


Figure 4.10: Retention of P(VDF-TrFE) piezoelectric capability over wide range of annealing temperatures. The material sample's polarization loop at 0.05 Hz was measured at room temperature after each successive annealing.

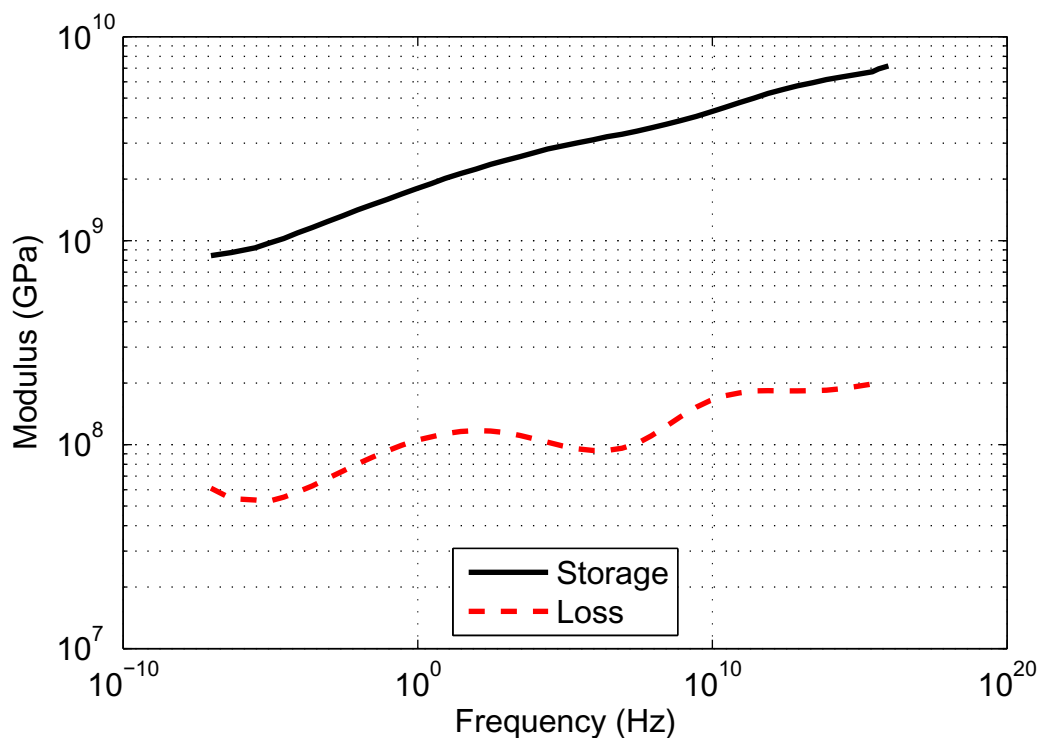


Figure 4.11: Copolymer viscoelastic master curve showing the storage and loss moduli compiled using time-temperature superposition of DMA test data at various frequencies and temperatures.

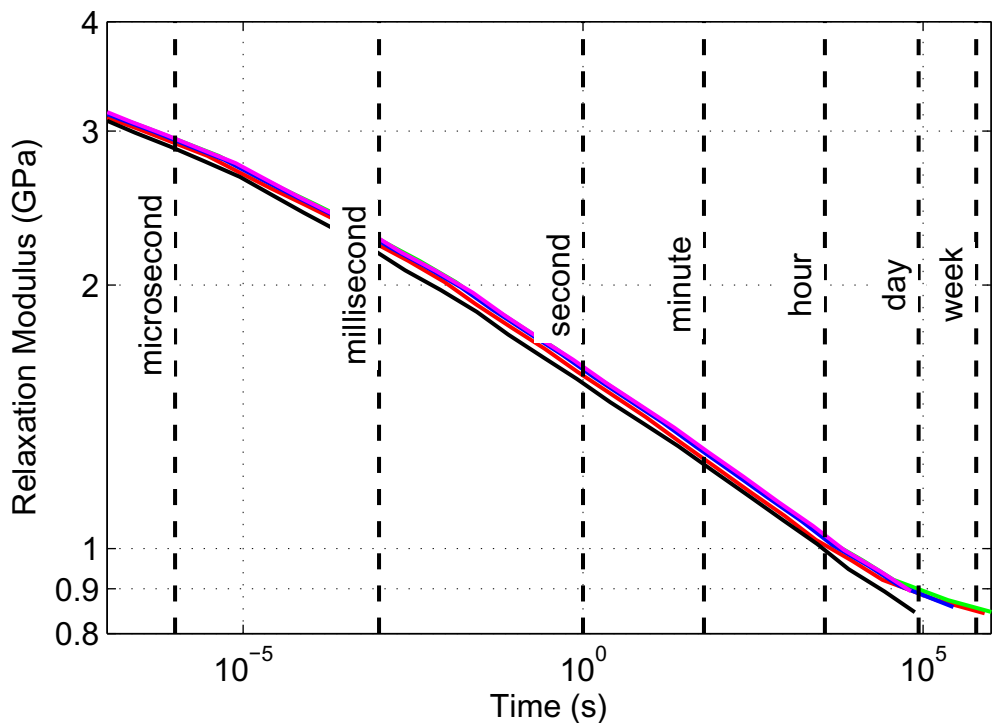


Figure 4.12: Estimates of the relaxation modulus derived from the master curve data using various approximate transforms from frequency domain into the time domain [38].

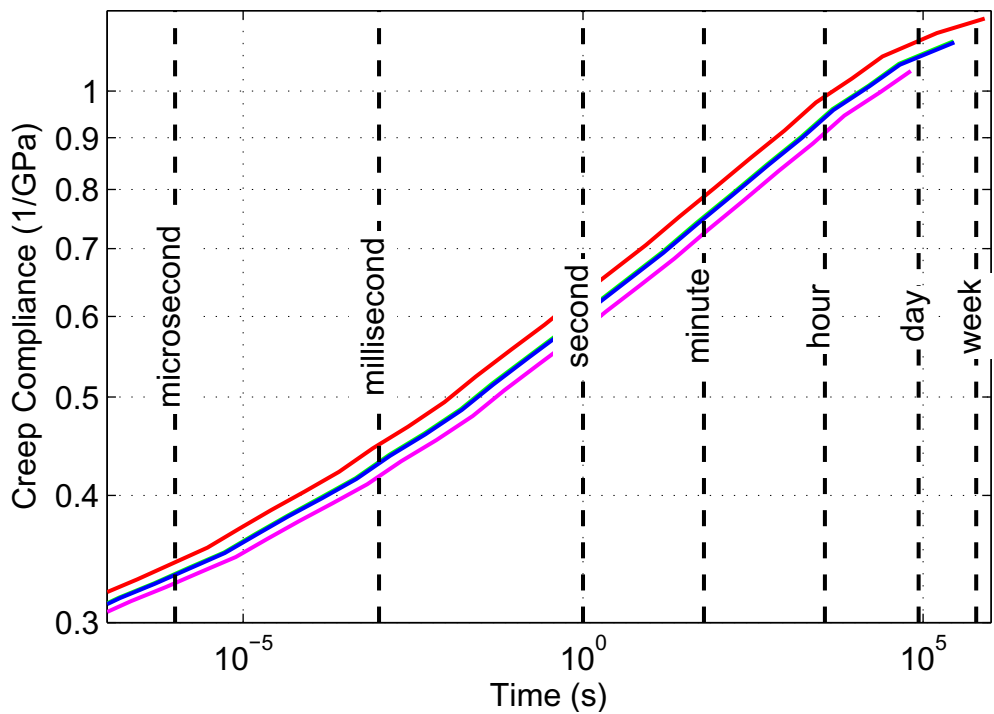


Figure 4.13: Estimates of the creep compliance derived from the master curve data using various approximate transforms from frequency domain into the time domain [38].

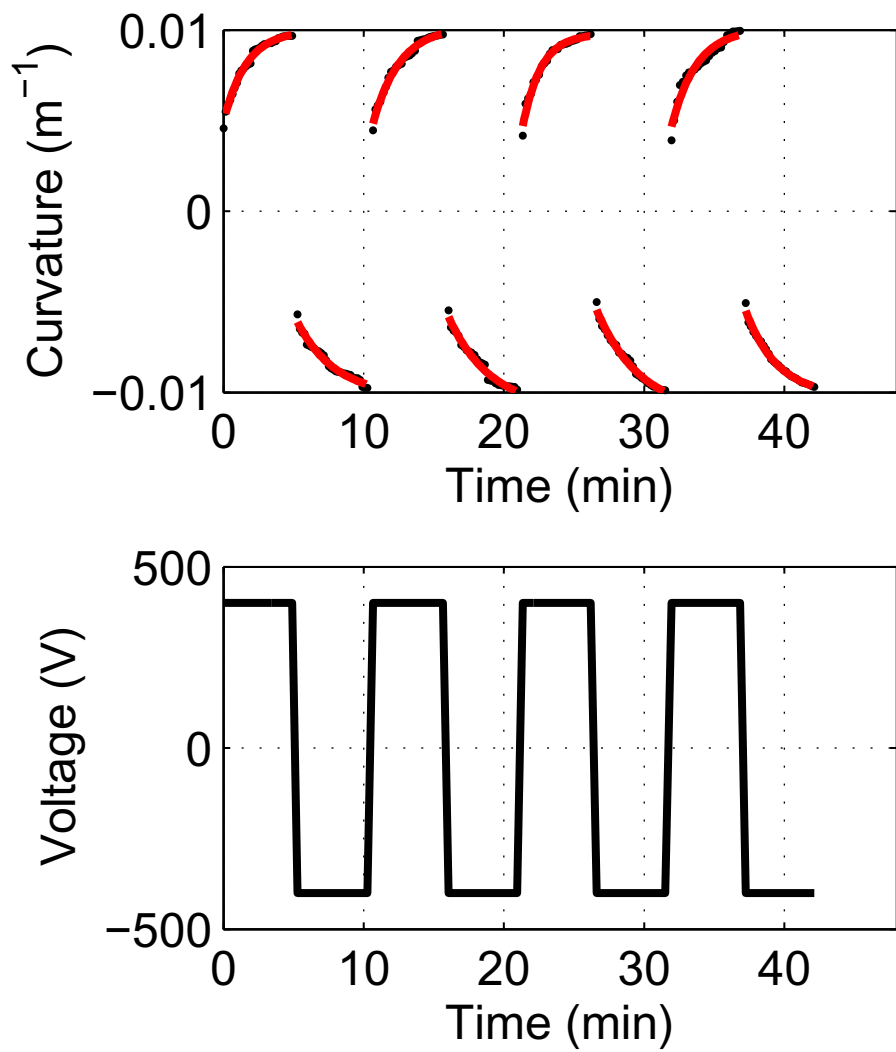


Figure 4.14: Laminate response to square wave voltage. Response indicates piezoelectric relaxation in the polymer. The average relaxation time was approximately 130 seconds.

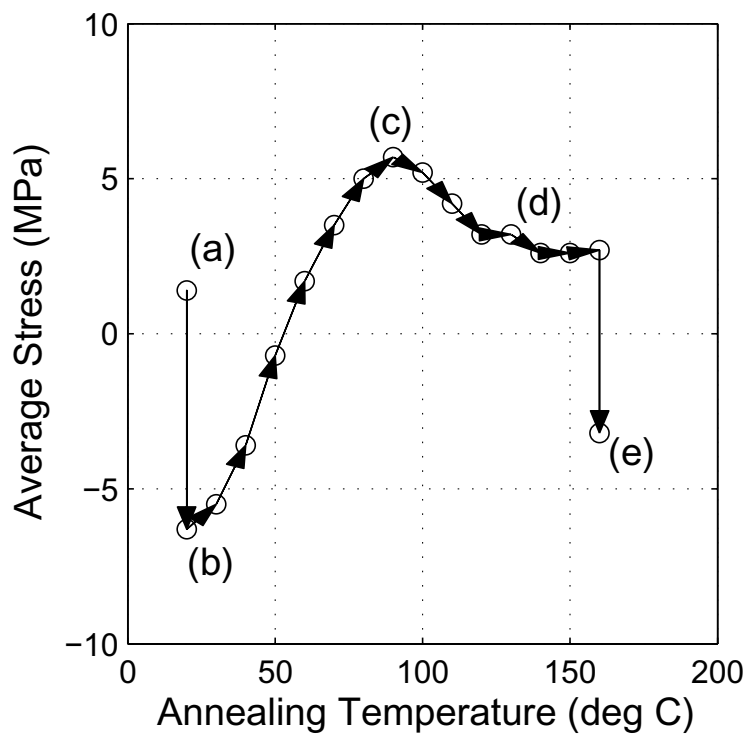
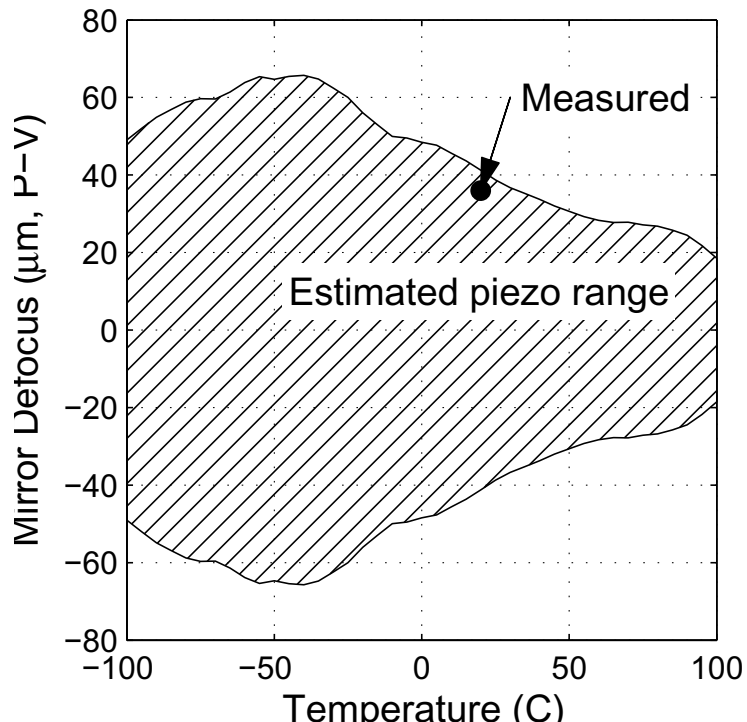
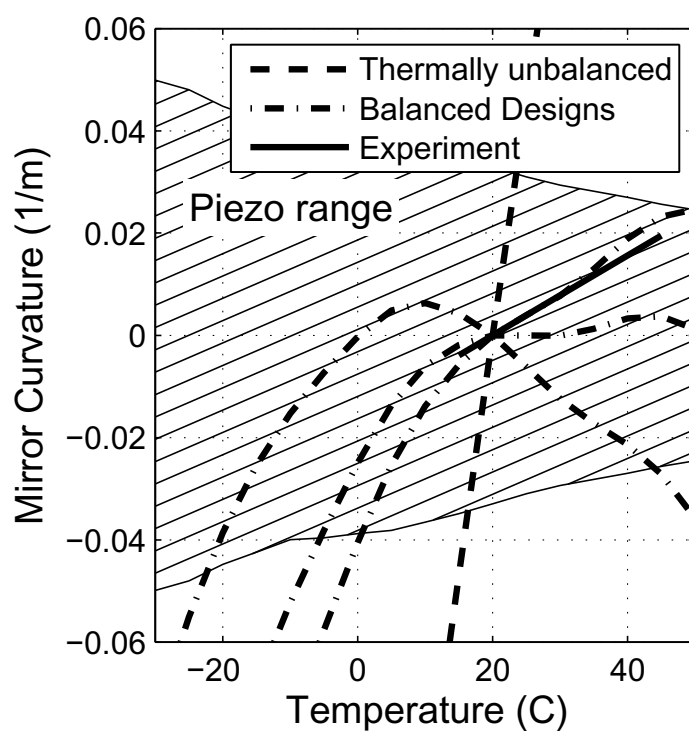


Figure 4.15: Annealing of the thermoplastic copolymer. The sample was successively annealed at higher temperatures. Stress measurements were taken at room temperature between each anneal. Significant points: (a) film as deposited; (b) poled; (c) Curie transition; (d) melting; (e) poled again.



(a)



(b)

Figure 4.16: Estimated laminate behavior for 20- μm copolymer film coated on 200- μm glass substrate across a wide temperature range: (a) estimated piezoelectric stroke, and (b) effect of thermal imbalance on allowable operating temperatures.

Chapter 5

Deformable Mirror Modeling and Optimization

This chapter discusses the modeling of the deformation control of the mirror using the piezoelectric layers. This enables the study and optimization of the electrode pattern geometry.

5.1 Mirror Shape Control

The root-mean-square (RMS) surface error (deviation from nominal shape) is a simple scalar measure of the shape-related performance of a mirror that is particularly convenient for comparison purposes; it will be utilized as a criterion for mirror design [2]. It should be noted that the high spatial frequency components of the RMS error will be governed by the mirror surface roughness, which is related to manufacturing techniques and processes that cannot be addressed with shape correction. On the other hand, minimization of the low-to mid-frequency components of the RMS error may be achieved through the use of a sufficient number of actuators that bend the mirror into the desired shape. These effects are addressed in this section, together with the numerical techniques for mirror surface control.

Consider m sampling points (nodes) distributed on the surface of a general mirror surface, and an associated control system with n actuators. Associated with the i^{th} actuator is a column vector, $\mathbf{a}_i \in \Re^m, i = 1..n$, obtained from the nodal deflections of the mirror due to a unit input (e.g., 1 volt) to the i^{th} actuator, while all other actuators are turned off. This column vector is known as the *influence vector* of actuator i , since it determines the influence that the actuator has on the mirror surface. It is linearly independent from the other $n - 1$ vectors, corresponding to the other actuators. Example influence functions are shown in Figure 5.2. The influence vectors are assembled into the *influence matrix*, \mathbf{A} :

$$\mathbf{A} = \begin{bmatrix} \mathbf{a}_1 & \mathbf{a}_2 & \dots & \mathbf{a}_n \end{bmatrix} \in \Re^{m \times n} \quad (5.1)$$

It is assumed that all deviations from the initial surface shape are small with respect to the diameter of the mirror. This assumption allows linear combinations of the influence vectors to be used to predict the mirror deflections. Hence, the influence matrix can be used to transform a *control vector*, $\mathbf{u} \in \Re^n$, consisting of the actuator input values, into a *shape deflection vector*, $\boldsymbol{\delta} \in \Re^m$, which contains the deflection of all nodal points of the mirror. Thus, the control vector and shape deflection vector are related via the influence matrix by:

$$\mathbf{A}\mathbf{u} = \boldsymbol{\delta} . \quad (5.2)$$

The correction of the mirror from its current shape, $\mathbf{s}_1 \in \Re^m$, to a desired shape $\mathbf{s}_2 \in \Re^m$ requires a deflection $\boldsymbol{\delta} = \mathbf{s}_2 - \mathbf{s}_1$. This deflection vector will, in general, not belong to the rangespace of \mathbf{A} . Therefore, the appropriate control vector is obtained from the least squares (LS) solution of Equation (5.2).

For generality, the nodal deflections are weighted by appropriate surface areas, S_i , to make the shape control formulation independent of meshing or sampling non-uniformities. In the present study, the values to S_i were found by calculating the Voronoi area [18] surrounding each node. These area weights are arranged along the diagonal of a matrix, $\mathbf{W} \in \Re^{m \times m}$, and Equation (5.2) is then modified to:

$$\mathbf{W}\mathbf{A}\mathbf{u} = \mathbf{W}\boldsymbol{\delta} . \quad (5.3)$$

The weighted, least squares solution of Equation 5.3 can be calculated using the QR factorization or other methods, and software packages such as MATLAB have in-built functionality to compute these solutions efficiently. If the available actuator inputs are constrained to a certain range, then a constrained, weighted, linear least squares solution would be required to find the optimal \mathbf{u} .

Once the solution \mathbf{u} has been determined, the difference between the approximation and the original is the residual vector or *residual shape error*, $\mathbf{r} = \mathbf{A}\mathbf{u} - \boldsymbol{\delta} \in \Re^m$ or, accounting for the weights in the residual,

$$\hat{\mathbf{r}} = \mathbf{W}\mathbf{A}\mathbf{u} - \mathbf{W}\boldsymbol{\delta} \in \Re^m . \quad (5.4)$$

For convenience, the weights in \mathbf{W} can be re-defined as the square roots of S_i non-dimensionalized by the total mirror surface area. Thus, the 2-norm of $\hat{\mathbf{r}}$ (usually with piston, tip and tilt removed) is then equivalent

to the RMS surface error:

$$\|\hat{\mathbf{r}}\|_2 = \sqrt{\hat{\mathbf{r}}^T \hat{\mathbf{r}}} = \sqrt{(\mathbf{A}\mathbf{u} - \boldsymbol{\delta})^T \mathbf{W}^2 (\mathbf{A}\mathbf{u} - \boldsymbol{\delta})} \quad (5.5)$$

$$\equiv \sqrt{\frac{\sum_i r_i^2 S_i}{\sum_i S_i}}. \quad (5.6)$$

5.2 Electrode Design

To minimize print-through effects on the front (mirror) surface of the laminate, the active material layer is coated uniformly over the entire substrate, and then patterned electrodes are deposited on top. This provides a range of individually addressable actuator regions. See Figure 5.1(a) for an example design with a glass substrate and annular electrode pattern. Complementary sets of actuation modes could potentially be created by stacking multiple active layers within the laminate, each with its own set of unique electrode patterns, although this has not been demonstrated experimentally yet at the time of this writing. For example, the design in Figure 5.1(b) shows large annular electrodes to provide broad, low order corrections with relatively large stroke capability, while a high density lattice of smaller electrodes in an upper active layer provides localized corrections at shorter length scales, albeit with lower stroke capability. See Figure 5.2 for example influence functions generated by selected electrodes from the low and high density patterns of Figure 5.1(b).

The topology and geometry of the high density electrode pattern were selected from a trade study that considered several different patterns. Figure 5.3 shows six designs grouped in two families of patterns with varying actuator densities. The substrate is 200- μm -thick silicon, and the actuation layer is a continuous 20- μm layer of P(VDF-TrFE). The first pattern type, Figure 5.3(a-c) consists of rectangular strips arranged in a triangular lattice similar to that shown in Figure 5.1. The second pattern type, Figure 5.3(d-f), is a hexagonal tessellation.

A finite element model was set up for each of these patterns, to compare their performance in making arbitrary corrections. The model was constructed in the software package Abaqus using S3T and S4T thermoelastic shell elements. Linear thermal expansion was used as a surrogate for the linearized piezoelectric effect, with the temperature field used as a substitute for the electric field, and the thermal expansion coefficient as a replacement for the d_{31} piezoelectric coefficient. The value of d_{31} in the model was scaled so as to make a temperature change of 1 degree K equivalent to the application of 1 V. This model was used to calculate the influence modes of each individual actuator (in units of m/V), by computing the mirror deflections due to a unit temperature change. The analysis assumed small deflections (geometrically linear response), and the material properties of the substrate and active layer were as given in Table 5.1. The results were then imported into and post-processed in MATLAB for constructing the influence and

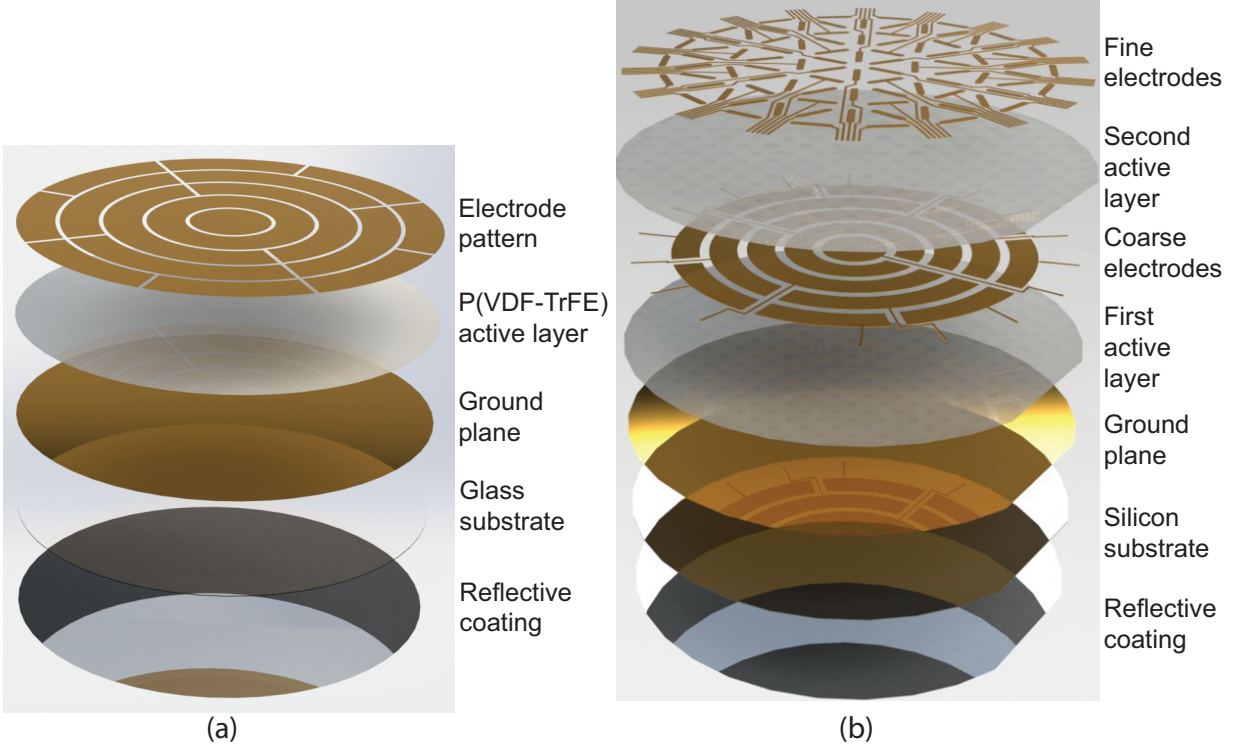


Figure 5.1: Exploded views of two example mirror designs that were explored at various points during this research: (a) single active layer design and (b) double active layer design.

weighting matrices, and calculating the performance of the mirror.

Table 5.1: Material properties.

Material	Property	Value
Si	Biaxial modulus M CTE α	180 GPa 2.6 ppm/K
P(VDF-TrFE)	Elastic modulus, E Poisson's ratio, ν	1.5 GPa 0.34
	Biaxial modulus, M	2.3 GPa
	Piezoelectric coefficient, d_{31}	16 pm/V

Shape errors in circular apertures are analyzed in terms of Zernike modes [3], which are a set of orthogonal polynomials defined over the unit disk. For each Zernike mode, Z_b^a with azimuthal and radial indices a and b , all mirror designs were evaluated for how well they can correct an error in the shape of the chosen mode; the maximum RMS amplitude that can be corrected prior to saturating any of the actuators was also evaluated. The correctability, C_b^a , of the mirror for each Zernike mode is defined as the ratio of the RMS amplitude of a desired Zernike deflection to the RMS amplitude of the residual (corrected) error, without considering the effects of actuator saturation. In other words, with the desired deflection vector set equal to the Zernike:

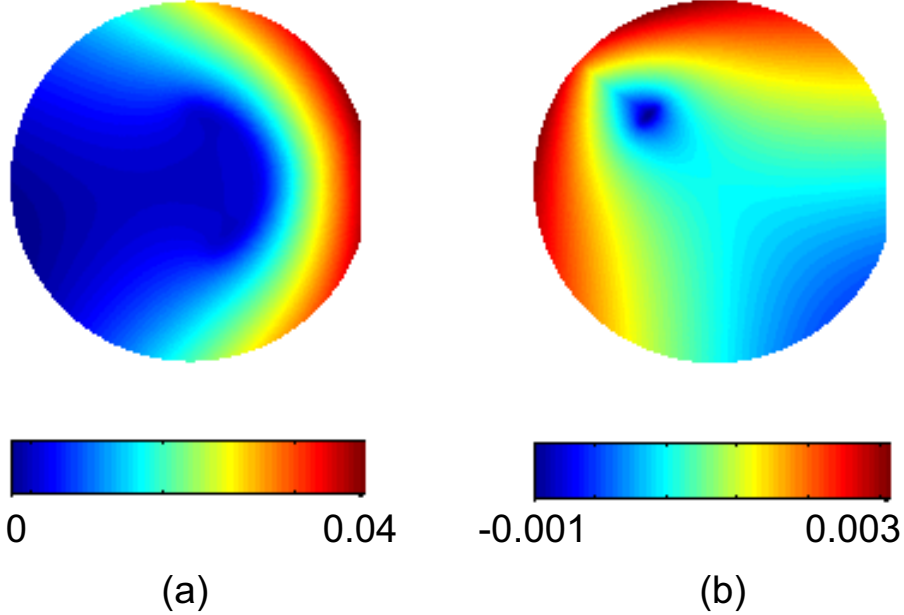


Figure 5.2: Finite element predictions of influence function shapes for selected electrodes from (a) coarse and (b) fine patterns of Figure 5.1. Units are $\mu\text{m}/\text{V}$.

$$C_b^a = \frac{\|\mathbf{W}\delta\|_2}{\|\hat{\mathbf{r}}\|_2} = \frac{\|\mathbf{WZ}_b^a\|_2}{\|\hat{\mathbf{r}}\|_2} . \quad (5.7)$$

Figure 5.4 shows the correctability, in the first thirty Zernike modes, for the six high-density electrode patterns presented in Figure 5.3.

The general relationship between a desired Zernike correction and the residual error is shown schematically in Figure 5.5. Initially, the relationship is linear with a slope in the curve equal to the inverse of the correctability. As the input amplitude increases, however, eventually a point is reached where one or more of the actuators reaches a limiting value and saturates. At this point and beyond, a constrained least squares solution is required. After this point, the slope becomes non-linear and curves upwards as the performance degrades. Eventually, all actuators will end up saturating at which point the relationship becomes linear once again with slope equal to unity. In other words, when all actuators are saturated, additional requested deflection will result in no additional correction, and the added input directly adds to the output.

The actual predictions for three important low-order modes (defocus, astigmatism and coma) are shown in Figure 5.6. Note that after partial saturation, the Hex43 residual RMS is lower for coma than the Hex91, due to the orientation of the mode with respect to the pattern of the electrodes.

The general trend is that for any chosen pattern, increasing the actuator density can improve both the

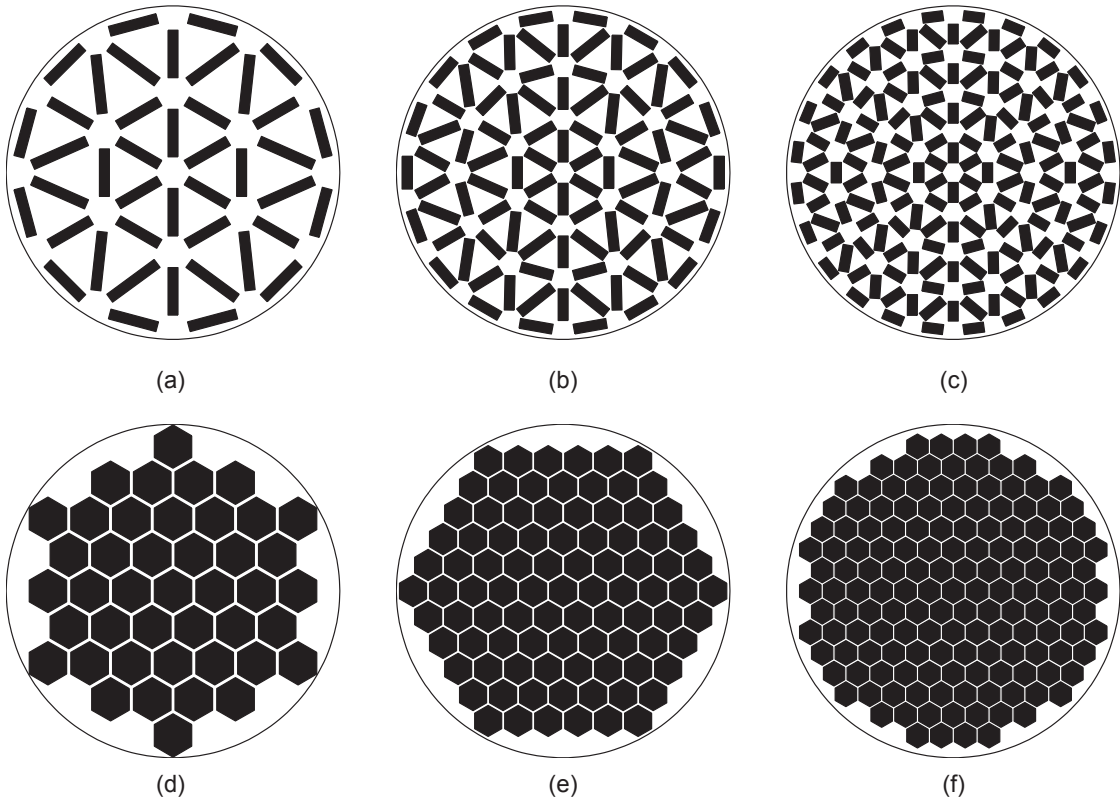


Figure 5.3: Electrode design patterns (a-c) triangular lattices with 42, 90, and 156 actuators; (d-f) hexagonal patch tessellations with 43, 91, and 151 actuators.

shape correction accuracy and available stroke, but this comes at the cost of increasing the complexity of the driving electronics. The choice of the electrode pattern is also important. Figure 5.3 shows that the triangular lattice pattern significantly outperforms the hexagonal pattern in terms of modal correctability, which can be explained by noting that placing the actuating strips in different orientations provides better control on the bending of the substrate in arbitrary directions. This aids in correcting shapes that require non-axisymmetric deformations. Figure 5.6 shows that the hexagonal pattern is able to achieve larger strokes before saturation, which can be explained by noting that the hexagonal pattern provides a higher coverage of the surface, and hence the total available actuation moment is higher. It would appear that a combination of these two patterns, where the unutilized area in the lattice patterns is filled in with triangular and hexagonal patches, may provide a good compromise between stroke and correctability.

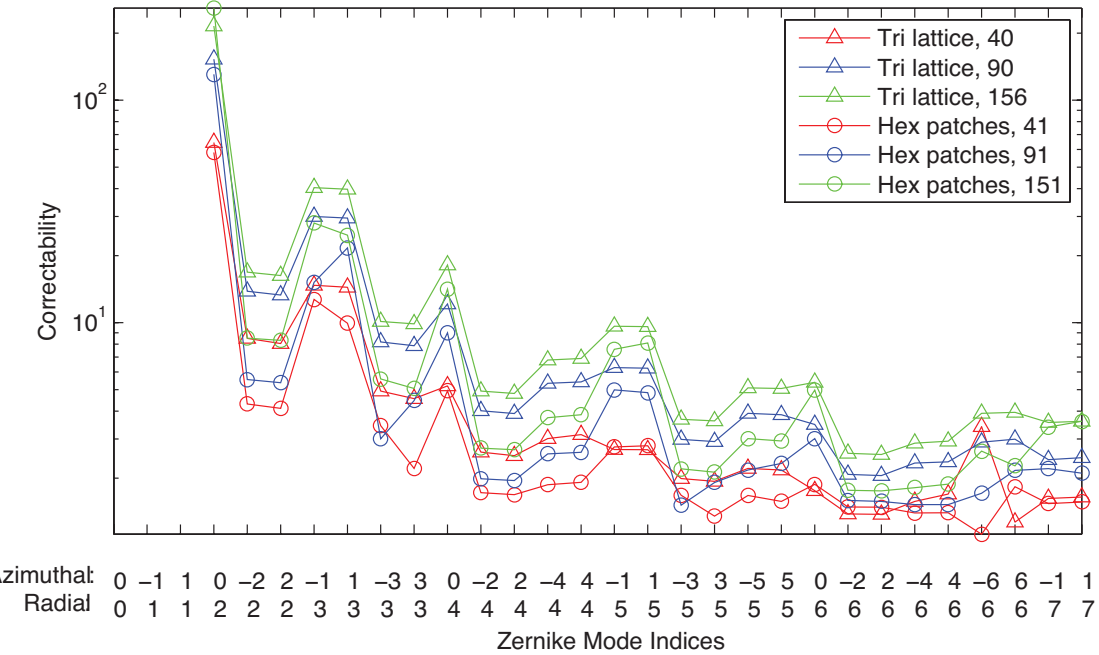


Figure 5.4: Correctabilities of six actuation patterns in Figure 5.3, for first 30 Zernike modes.

5.3 Optimized Pattern

When considering the lowest-order modes, defocus is easy to achieve with both high strokes and high correctability so long as the actuator pattern fills the mirror densely with few gaps or holes. However, astigmatism, which is very prevalent in the optical system from misalignments or mirror decenters, is much more difficult to correct. This is because the astigmatism is a mechanical twisting of the mirror, and since the actuation material and substrate are isotropic in the plane, the actuators don't naturally produce twisting effects in the substrate. A straightforward way to produce a twist would be using externally applied forces on the rim of the mirror. However, this would require a complex mounting and control scheme with precision assembly and alignment, which is undesirable.

Instead, another way is to emulate the effect of external edge loading by placing many narrow electrodes along the circumference of the mirror, similar to the outermost electrodes in the triangular lattice patterns. A numerical study [21] was done in which overlapping, parameterized ellipses were used to partition the electrodes on the mirror in order to produce these narrow-edge electrodes, without producing unused gaps in the pattern as in the previously discussed lattice. The resultant design, shown in Figure 5.7, was dubbed the “Notre Dame” design because of its similarity to the iconic window of the cathedral. This pattern improved on the astigmatism performance while retaining good performance in other modes. The correctability of astigmatism was improved even further by trimming several millimeters from the mirror pupil at the edge.

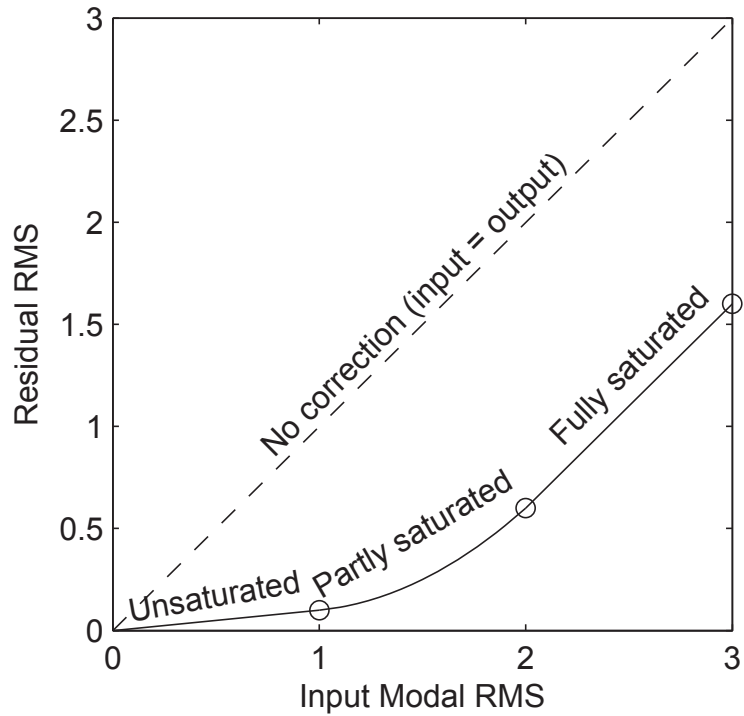


Figure 5.5: General relationship between residual and input error in any chosen mode.

Figure 5.8 shows the correctabilities of the design using a 95-mm pupil diameter. The strokes and saturation response for the lowest modes are also shown in Figure 5.9.

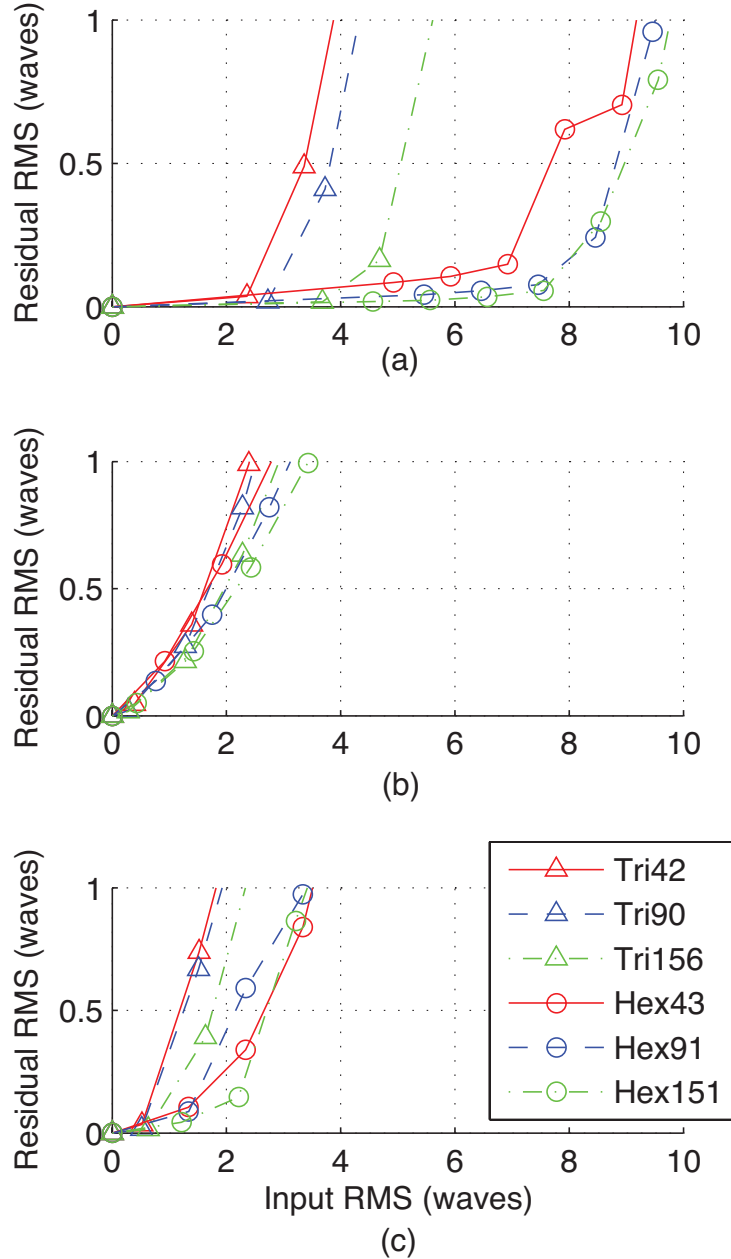


Figure 5.6: Variation of residual RMS error with RMS error in three chosen modes for the six actuation patterns in Figure 5.3; (a) Mode Z_2^0 defocus; (b) Mode Z_2^{-2} astigmatism; (c) Mode Z_3^{-1} coma. Reference wavelength is 633 nm.

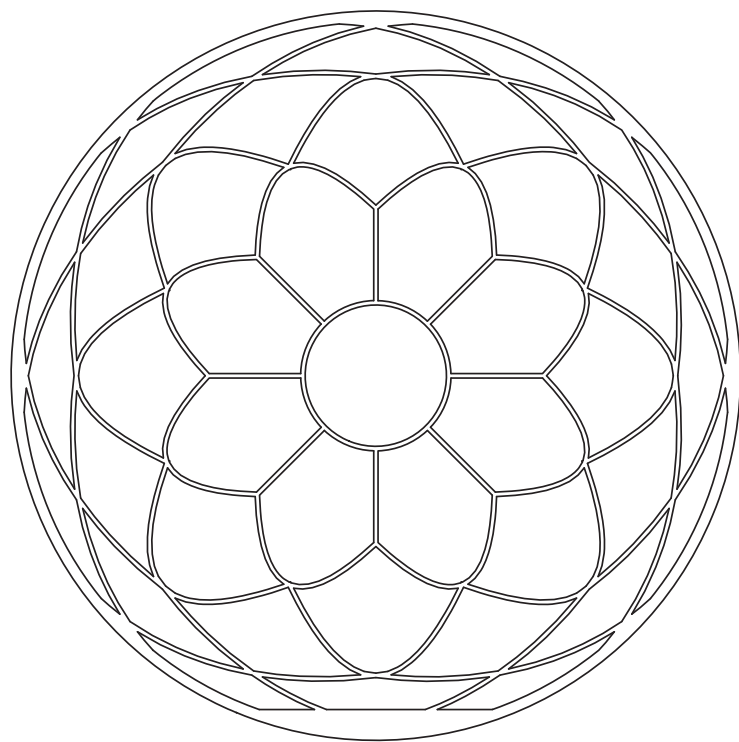


Figure 5.7: Optimized “Notre Dame” electrode pattern design with 41 actuators filling most of the 100-mm-diameter area with small gaps for fabrication purposes.

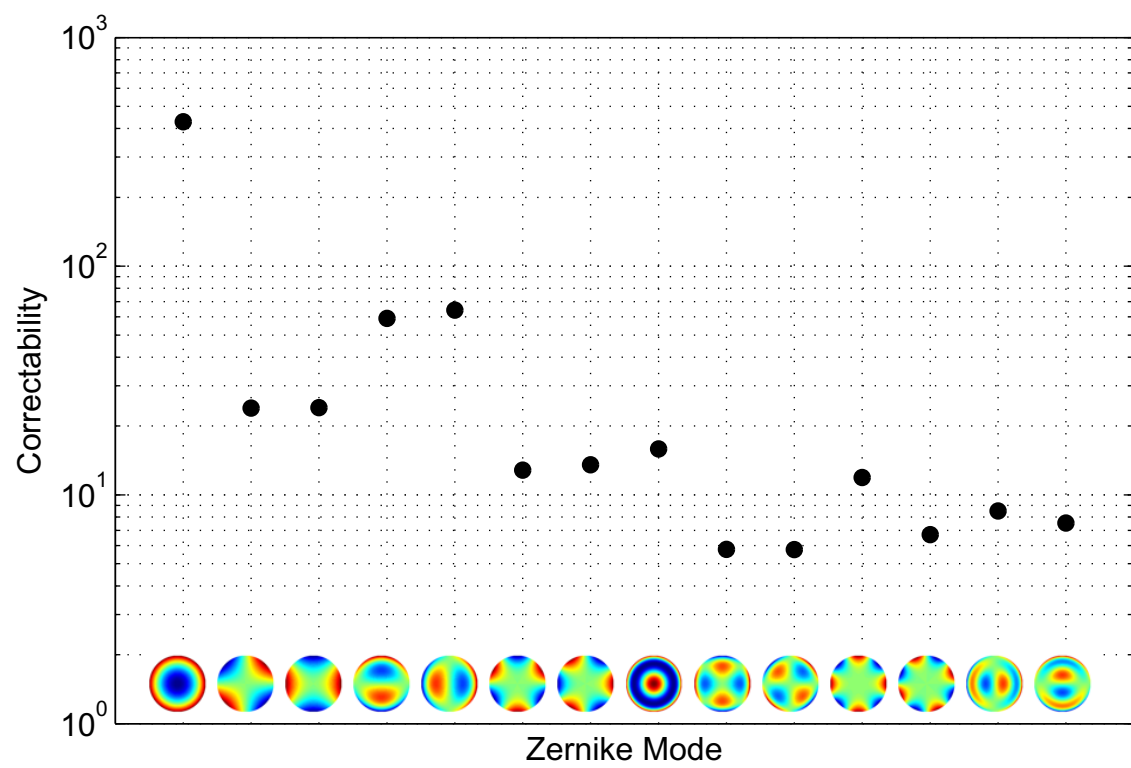


Figure 5.8: Modal correctabilities for the lowest Zernikes for the optimized "Notre Dame" pattern.

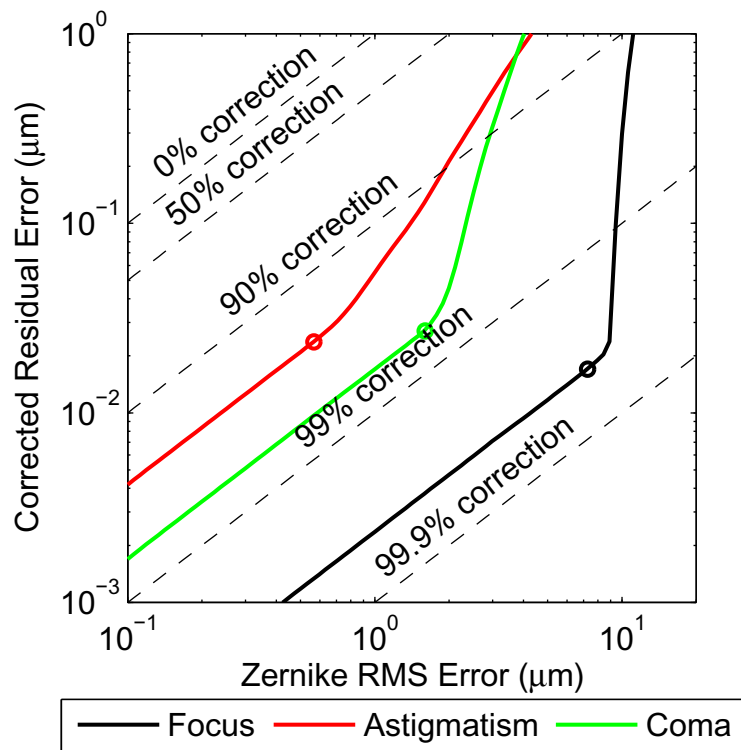


Figure 5.9: Stroke and correctability performance for the low order shape modes: focus, astigmatism, and coma. The points of first actuator saturation are marked on the plot with circles.

Chapter 6

Mirror Experiments

The chapter reviews some shape control experiments that were performed on various iterations of the deformable mirror design.

6.1 Measurement Testbed

In order to measure mirror shapes, an optical testbed based around a ThorLabs WFS150-7AR Shack-Hartmann wavefront sensor was used. The sensor utilizes an array of lenslets to form an array of spots on an image sensor; the deviation of the spots from a perfect grid is proportional to the local slope error in the wavefront [33]. Figure 6.1 shows a diagram of the experimental setup, and Figure 6.2 shows a photograph of it. It consists of a 633-nm laser beam filtered with a pinhole, collimated, reflected off the deformable mirror under test, and then passed to the wavefront sensor by means of a beamsplitter and lens. This arrangement was chosen so as to reimaging the mirror pupil to a smaller size that will fit inside the sensor aperture. With a good alignment of all components, the wavefront sensor provides a measurement of the surface figure of the mirror. The Shack-Hartmann sensor was calibrated by the manufacturer. A thick, flat mirror was used to align the setup; the deformable mirror was substituted in, and the Shack-Hartmann sensor was moved in piston to zero the defocus and capture the image of the pupil (mirror). In other words, the shape measurement was relative to the closest sphere.

Two 100-mm-diameter prototypes have been tested at room temperature using this setup. The first was a simple 16-channel design with an electrode geometry, as shown in Figure 6.5, on a 200- μm single crystal silicon (1-0-0) substrate with a 20 μm P(VDF-TrFE) coating. The 16-channel electrode pattern was originally just a preliminary design to be used with a finer scale pattern in a multi-layer mirror (see [28]). However, this prototype only included the coarse pattern layer. The second mirror prototype was a 41-channel design with the “Notre Dame” optimized electrode pattern as shown in Figure 6.7, done in cooperation with Dr. Laslandes (see [21]). This mirror had a 235- μm borosilicate glass substrate with a

10- μm P(VDF-TrFE) coating. The measurement area of the first prototype was constrained by the clear aperture of a 75-mm-diameter objective lens. The second prototype test used a 100-mm objective, and was limited by the Shack-Hartmann aperture. The measurements on the second mirror were limited to a 100-mm-by-80-mm image area, and trimmed down to an 80-mm pupil size. Neither mirror prototype was thermally balanced; they only had thin reflective coatings. Therefore, changes in lab temperatures were able to affect the mirror shape.

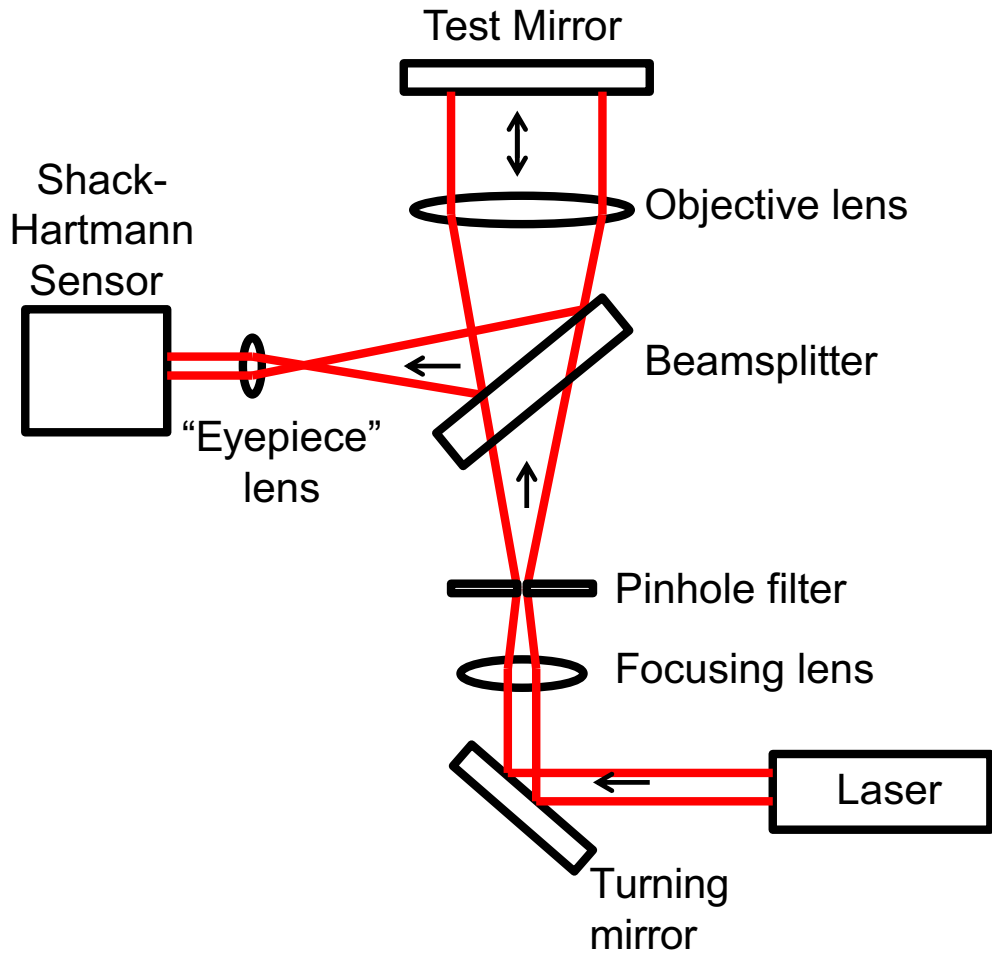


Figure 6.1: Schematic diagram of experimental measurement setup.

6.2 Control Implementation

A high voltage multiplexer was prototyped for use in controlling the mirrors. To be consistent with the overall approach of minimizing the mass of the mirror, the mass and volume of the control electronics should also be as low as possible. Therefore, rather than using a high voltage amplifier for each channel, a single

amplifier was used to control all channels, following the scheme shown in Figure 6.3(a). For lab testing, a single Trek 10/10B high voltage amplifier was used as the sole amplifier.

The mirror controller is based partly on a design proposed by Song et al [39]. It consists of a microcontroller whose analog output is amplified to the range -500 V to +500 V by a single high voltage amplifier, and then multiplexed into the individual actuator channels that electrically act like capacitors. The controller cycles through each actuator and sets the channel voltage. The voltage level is then held with some minor leakage until the next refresh cycle. This allows control over a large number of actuators using a single controller board and amplifier board at the expense of control frequency bandwidth, which is ideal for low frequency disturbances that would be expected in the space environment, such as static manufacturing error, thermal changes and viscoelastic creep. The multiplexing concept is illustrated in Figure 6.4, and a photo of a prototype 42-channel multiplexer is shown in Figure 6.3(b). The controller operates around 1 Hz, and would therefore be unable to compensate vibrational disturbances. Instead, vibrations should be accounted for passively in the design scheme or lab setup.

6.3 Measured Influence Functions

6.3.1 16-Channel Prototype

Figure 6.6(a) shows the measured, individual influence functions from the various channels. The channel numbers are defined in Figure 6.5. These measurements were obtained by taking the difference in shape between a reference measurement with all channels off, and a new measurement with a single channel turned on and set to 400 V. Figure 6.6(b) shows the corresponding predictions obtained from the finite element model described in Chapter 5. Visually, there is a reasonable match between measurements and predictions, but quantitatively the discrepancies were such that experimentally-based influence functions would be required for accurate shape control. The discrepancies were likely due to beam misalignments as well as thermally-induced disturbances of the unbalanced laminate. For example, channel 9 shows evidence of astigmatism in the experimental measurement, due to residual misalignments.

6.3.2 41-Channel Prototype

Figure 6.8 shows influence functions from the 41-channel prototype mirror with optimized electrode pattern. Due to the thinner piezo layer, which was more sensitive to defects, this mirror suffered from four shorted channels after poling, assembly, and wirebonding. Several more channels were later shorted during testing due to an accidental over-voltage. Luckily, however, at least one channel remained operational from each uniquely shaped electrode set. The channel numbers are defined in Figure 6.5. These measurements were obtained by taking the difference in shape between a reference measurement with all channels off, and a

new measurement with a single channel turned on and set to 500 V. The corresponding FEM predictions are shown alongside each measurement. Visually, there is a very good match between measurements and predictions for both shape and amplitudes. A more detailed comparison between the amplitudes of the influence functions' Zernike components is shown in Figure 6.9.

The better agreements this time were likely due to increased attention to setup alignment. This gives reasonable confidence that the modeling is good enough for design optimization work and performance predictions. Although again, the discrepancies are such that experimentally-measured influence functions should be used during actual telescope operation for shape control, due to the ease of measuring them in situ.

6.4 Focus Control

This test consisted of using all 16 channels of the first prototype to control a single mode. The mode chosen was defocus, i.e., the axisymmetric base curvature component of the mirror surface. A simple, proportional derivative (PD) feedback controller was implemented with non-optimized gains and, for simplicity, the same voltage value was assigned to all channels. An experiment was carried out in which a step defocus change of 2 waves (at 633 nm) with a long hold was requested; the step response of the controlled mirror is shown in Figure 6.10 along with the applied voltage of the controller output.

In the figure, note that after a settling period, dependent on the controller gains, the mirror defocus was controlled well within a small fraction of a wavelength. The long term drift and oscillation in the control voltage were likely in response to the uncontrolled lab thermal environment, creep, and lightly damped controller feedback.

6.5 Shape Control

6.5.1 16-Channel Prototype

A more complex scenario is to control many response modes using all of the available actuation channels in order to reduce the mirror aberrations: for example, to make the mirror as flat as possible. In this test, the lowest 66 Zernike modes were minimized in a least squares sense with 16 independent voltages of the first prototype. The control algorithm was implemented by decomposing each of the 16 measured influence functions for the mirror into its Zernike components, and then implementing a PD feedback controller that reduces the magnitudes of the measured Zernike components of the actual mirror shape. At each step, the control solution was obtained by computing a constrained least squares solution of Equation 5.2, and multiplying it by a factor less than unity to ensure a damped response without overshoot, and to reduce

possible material hysteresis effects. The influence functions of the mirror were assumed to be constant and independent of voltage throughout the test.

Figure 6.11 shows the evolution of the measured RMS error during this test. The initial RMS error was 5.2 waves (at 633 nm), which was reduced to about 2.3 waves (an improvement of about 55%) in about 4 steps. The controller was left running for about 10 minutes to verify its ability to maintain this low error. Note that most of the channels hit the controller limits of ± 400 V, which indicates that the actuation stroke would have needed to be improved in order to further reduce the error. However, this simple design was not expected to reach diffraction-limited performance, and was instead an exercise in implementing the feedback shape control.

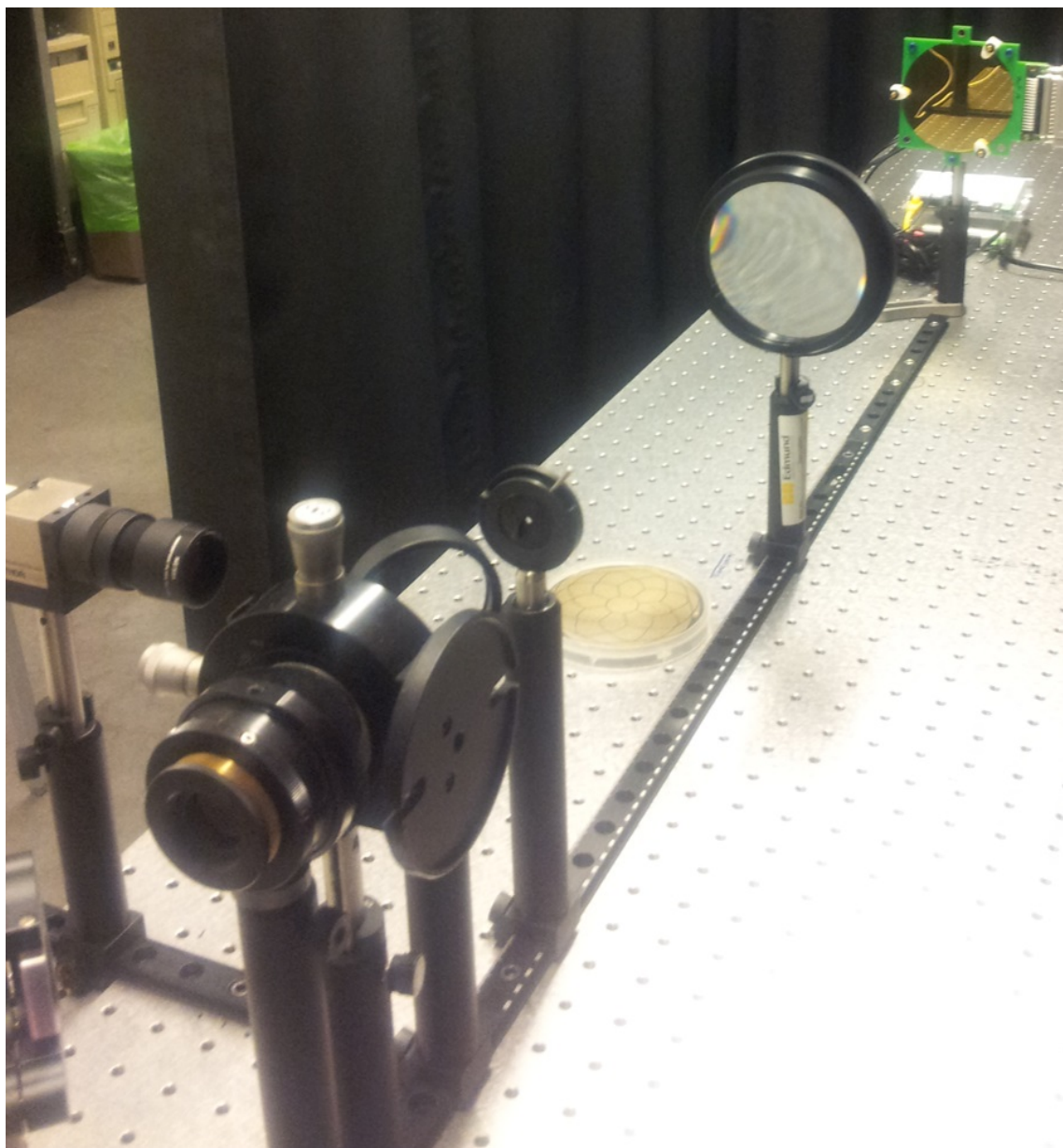


Figure 6.2: Photo of experimental measurement setup.

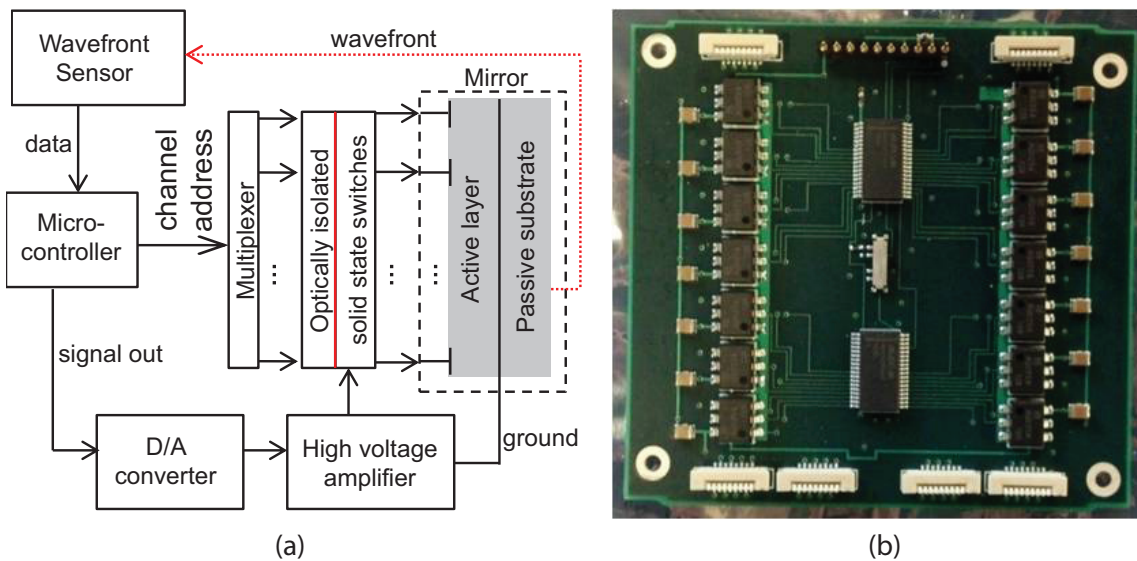


Figure 6.3: (a) Schematic diagram of control system showing wavefront feedback from the mirror passed to a controller; the controller then uses a high voltage amplifier and multiplexer to apply a new set of voltages to the mirror electrodes. (b) Photo of a 10-cm-by-10-cm prototype high voltage multiplexer board populated with solid state switches is shown on the right; it is capable of running 42 channels to +/- 500 V.

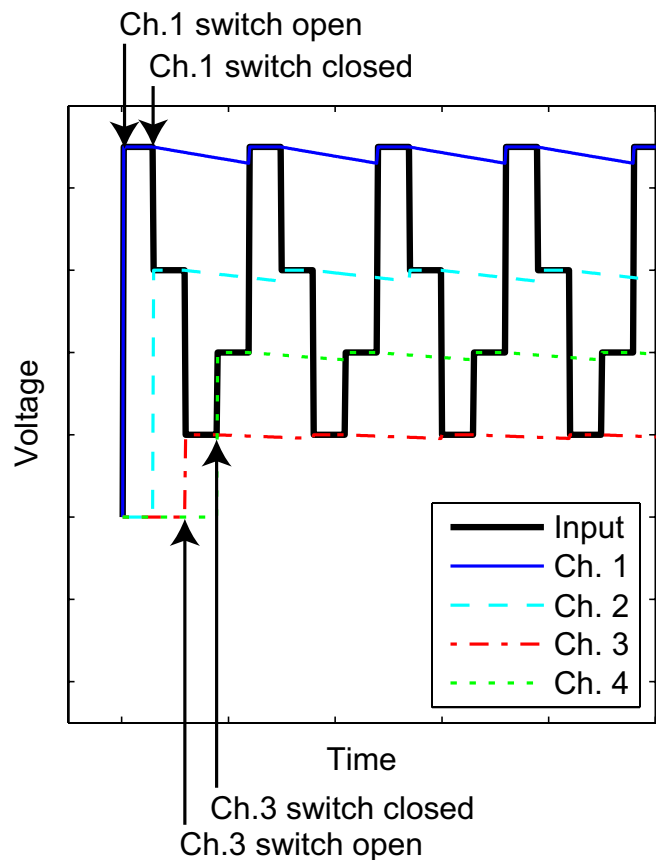


Figure 6.4: Traces showing time-varying high-voltage input (heavy, black) and multiple actuator channels (light, colored) with a steady quasi-DC level. Channel decay between refresh points is exaggerated for illustration purposes.

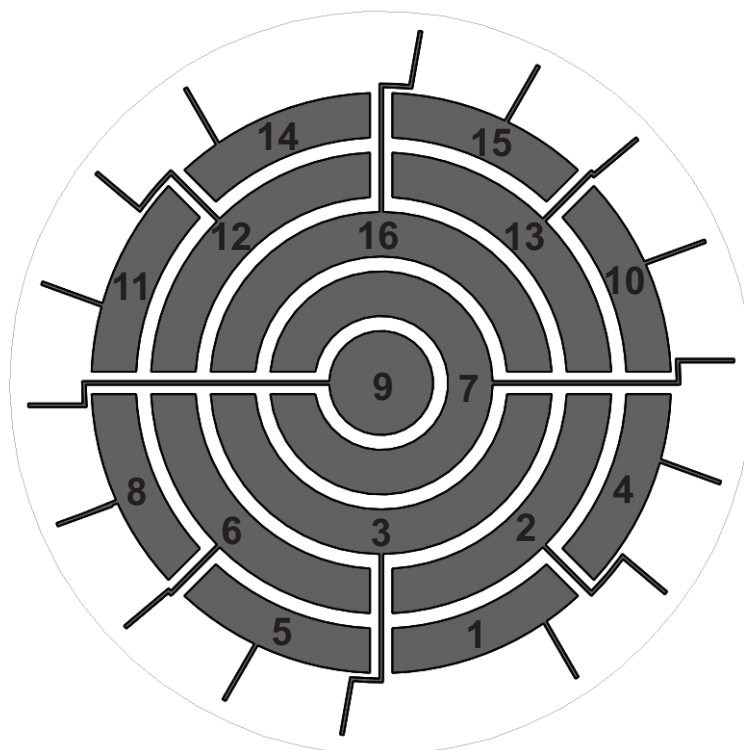


Figure 6.5: Definition of actuator numbers for 16-channel prototype.

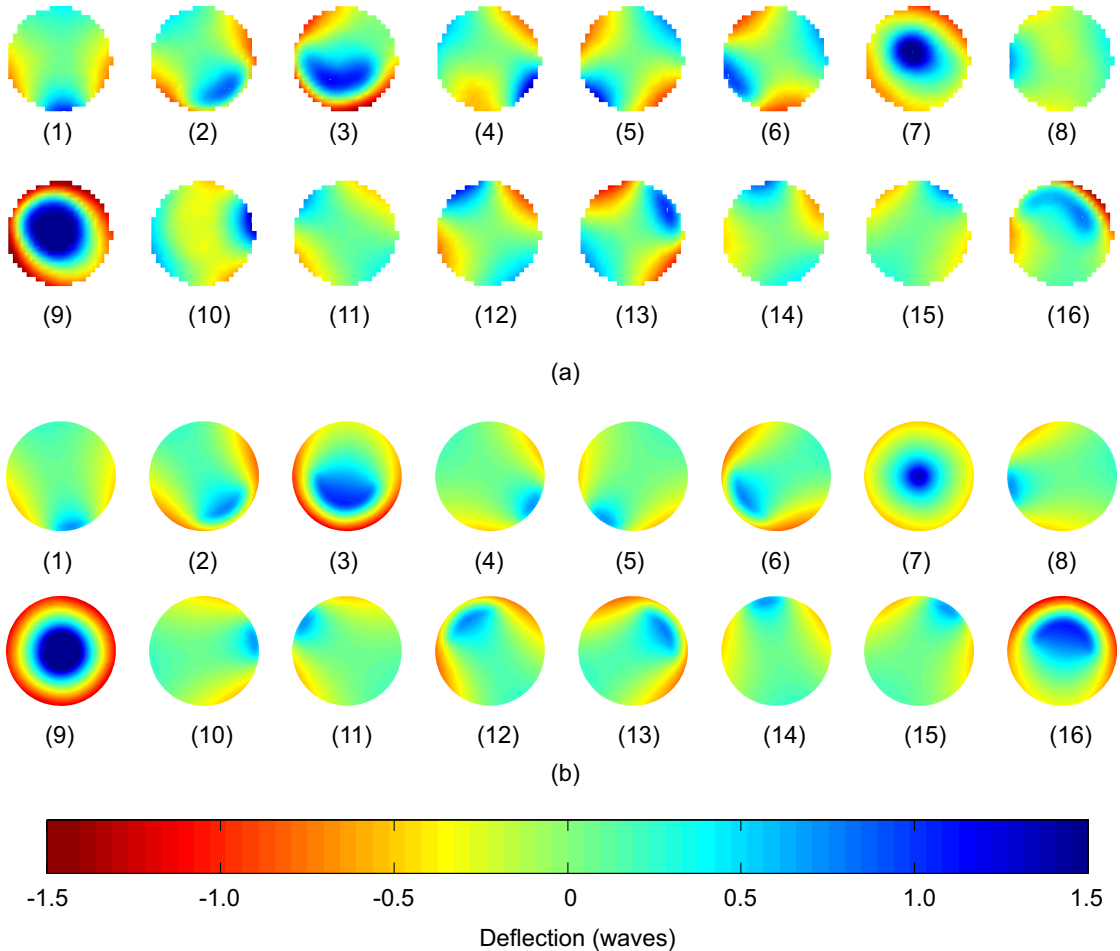


Figure 6.6: Influence functions of preliminary 100-mm mirror prototype with 16 channels with the pattern in Figure 6.5. (a) experimental measurements and (b) finite element predictions due to 400-V inputs. Deflection color scale is in units of waves at 633 nm. The diameter of the images is only 75 mm, due to objective lens size constraints.

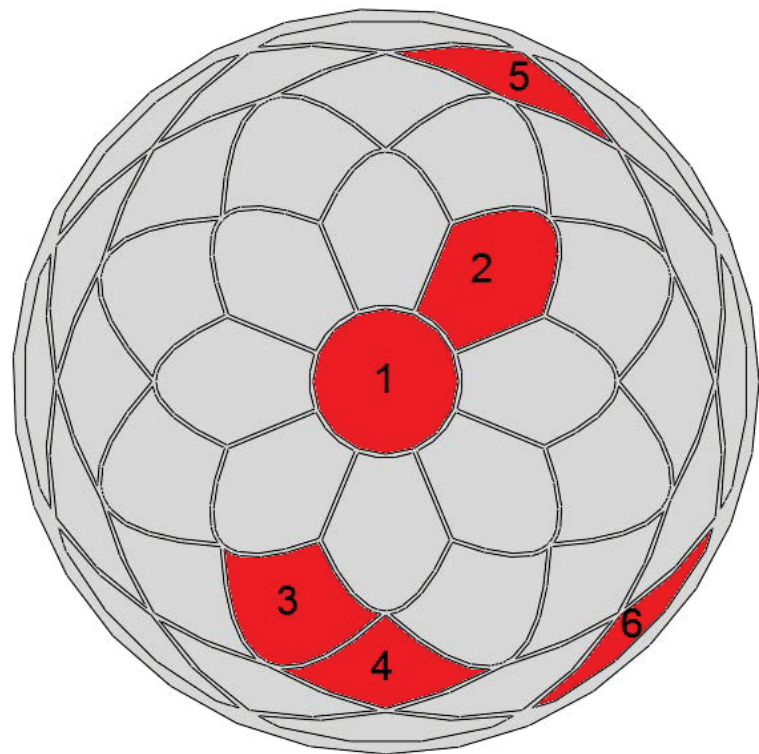


Figure 6.7: Numbering definition of unique actuators for 41-channel prototype used in Figure 6.8.

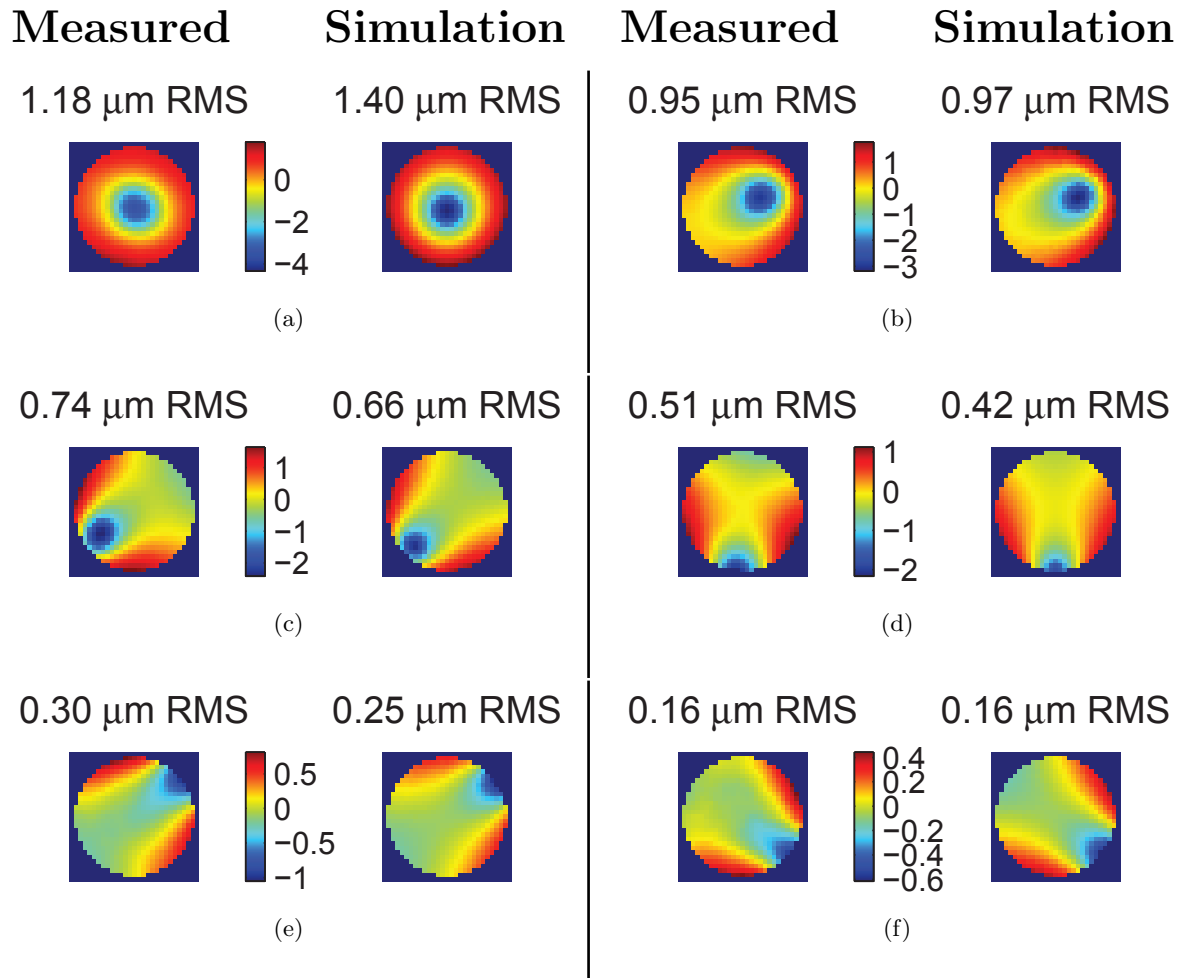


Figure 6.8: Side-by-side comparisons of the 6 unique influence functions in the 41-channel actuation pattern as measured (left side) and as simulated (right side). (a)-(f) correspond to labels 1-6, as shown in Figure 6.7. Units are micrometers.

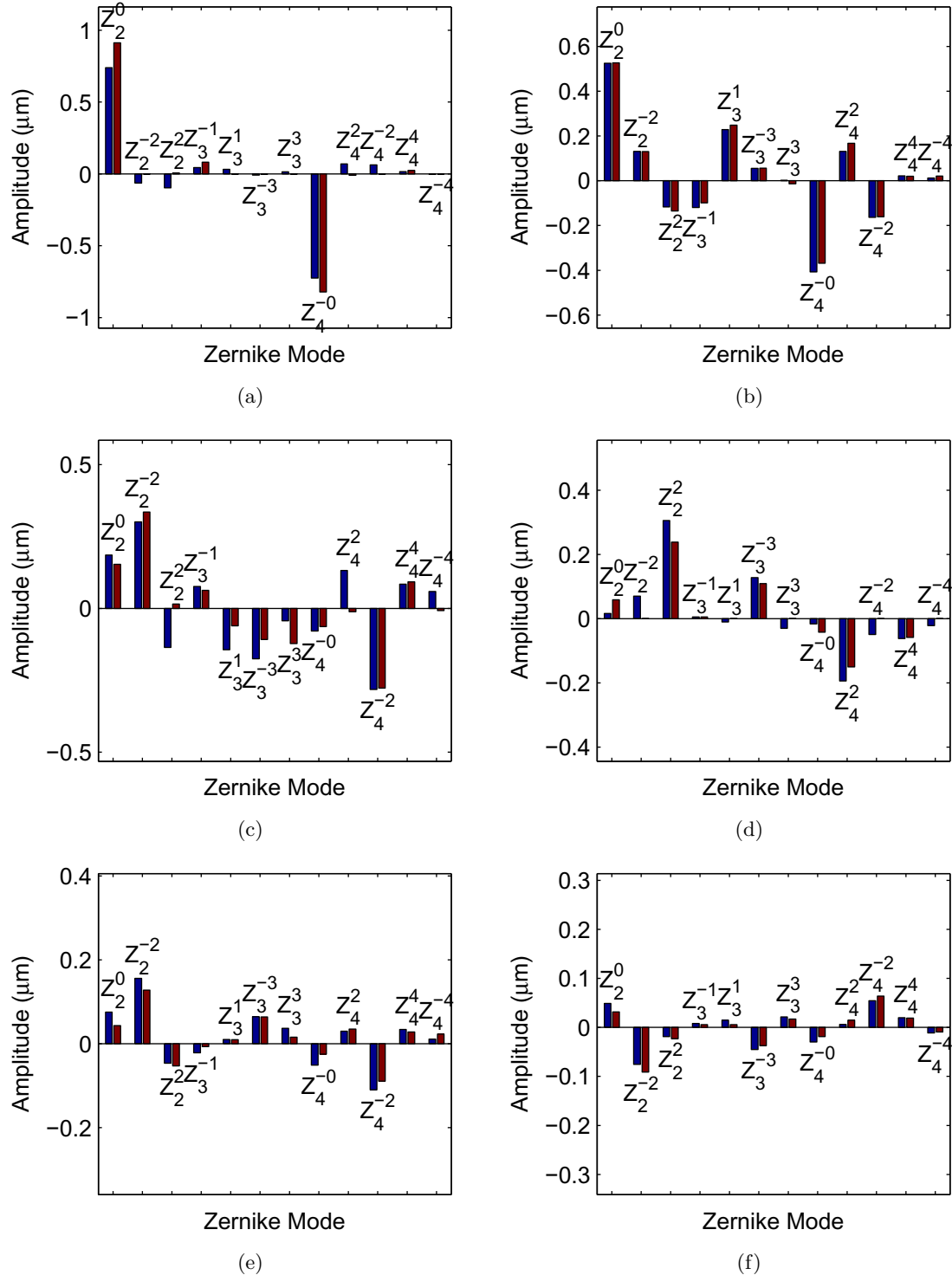


Figure 6.9: Comparisons of the Zernike components of the 6 unique influence functions in the 41-channel actuation pattern as measured (blue columns) and as simulated (red columns). (a)-(f) correspond to labels 1-6 as shown in Figure 6.7. Units are micrometers.

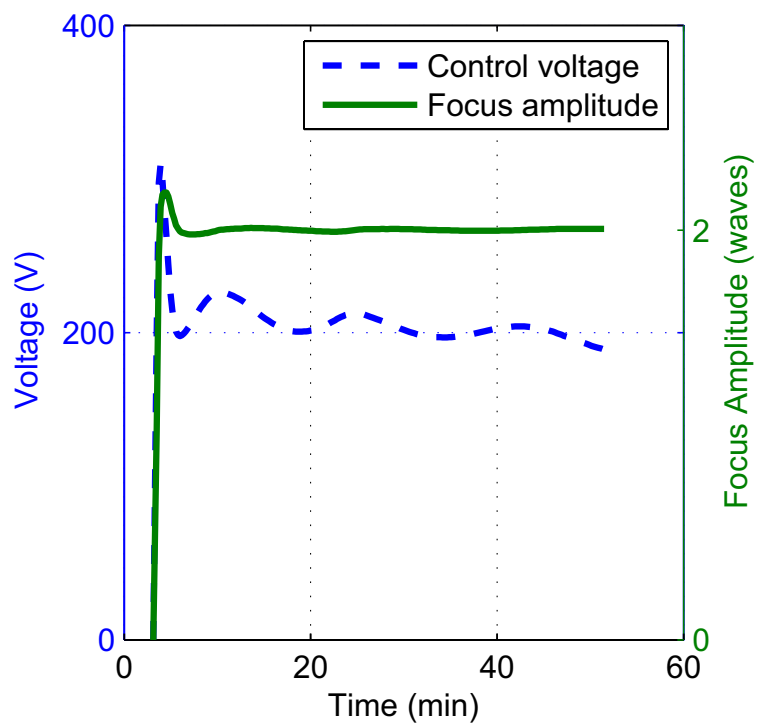
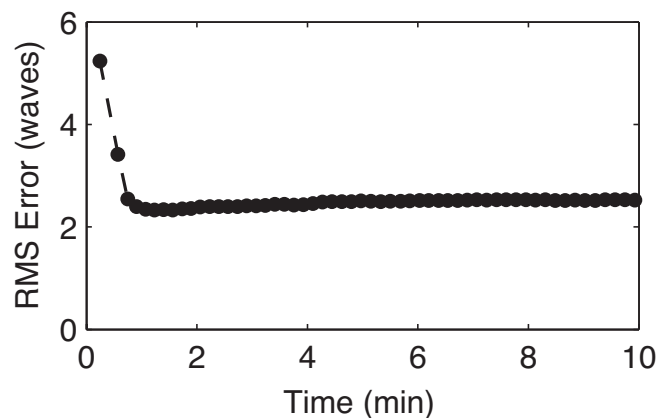
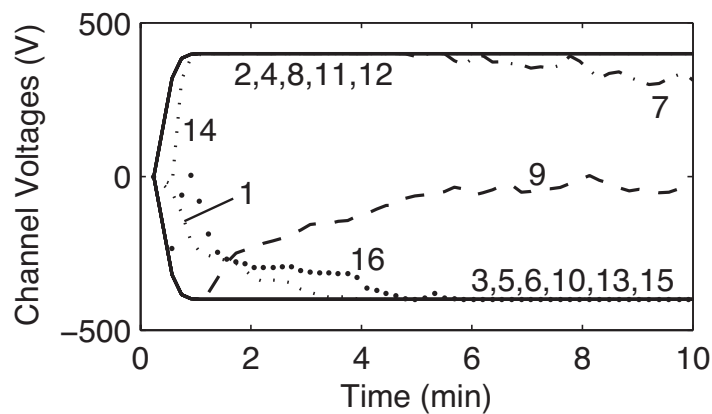


Figure 6.10: Demonstration of defocus control using a single input voltage.



(a)



(b)

Figure 6.11: (a) Reduction of static RMS shape error using 16 channels and (b) evolution of channel voltages.

Chapter 7

Mirror Performance Analysis

This chapter covers the behavior and performance of the mirror in the launch and space environments, subject to vibrational loading, viscoelastic creep, and thermal effects. A model is also built to show the closed-loop wavefront control system performance in the AAReST telescope.

The design chosen for the performance analyses is shown in Figure 7.1. The reflective coating layer (1) is assumed to be the aluminum chromium laminate or similar, with thickness such that the mirror is optimally balanced at 0 °C and 20°C, with a thermal response as shown in the leftmost “Balanced Design” curve in Figure 4.16b. The substrate (2) is borosilicate glass with a thickness of 200 μm . The ground layer (3) is a laminate of 10 nm of titanium, 100 nm of gold, and 10 nm of titanium. The active layer (4) is 20 μm of poled P(VDF-TrFE). The electrodes are 10 nm of titanium and 100 nm of gold, and patterned into the “Notre Dame” design. The controller voltage limits are -500 V and +500 V. The mirror is assumed to be spherically curved with a nominal radius of curvature of about 1.2 m. Due to the small curvature, the mirrors are assumed to behave mechanically as circular flat plates. The assumed as-manufactured shape errors are given in Table 7.4.

7.1 Acoustics and Launch Survival

The mirrors are low mass objects with a relatively large surface area. This makes them especially prone to damage from acoustic pressures during the launch to orbit. Traditionally, mirrors are designed to be stiff enough to endure these loads without damage. However, this mirror design was driven instead by shape adaption performance and low areal density.. Therefore, the mirrors will be analyzed in a framework that could be used to determine the needed boundary conditions for launch survival, and these boundary conditions could later be realized using a temporary restraint system that releases the mirror on orbit, after acoustic loads are no longer a concern.

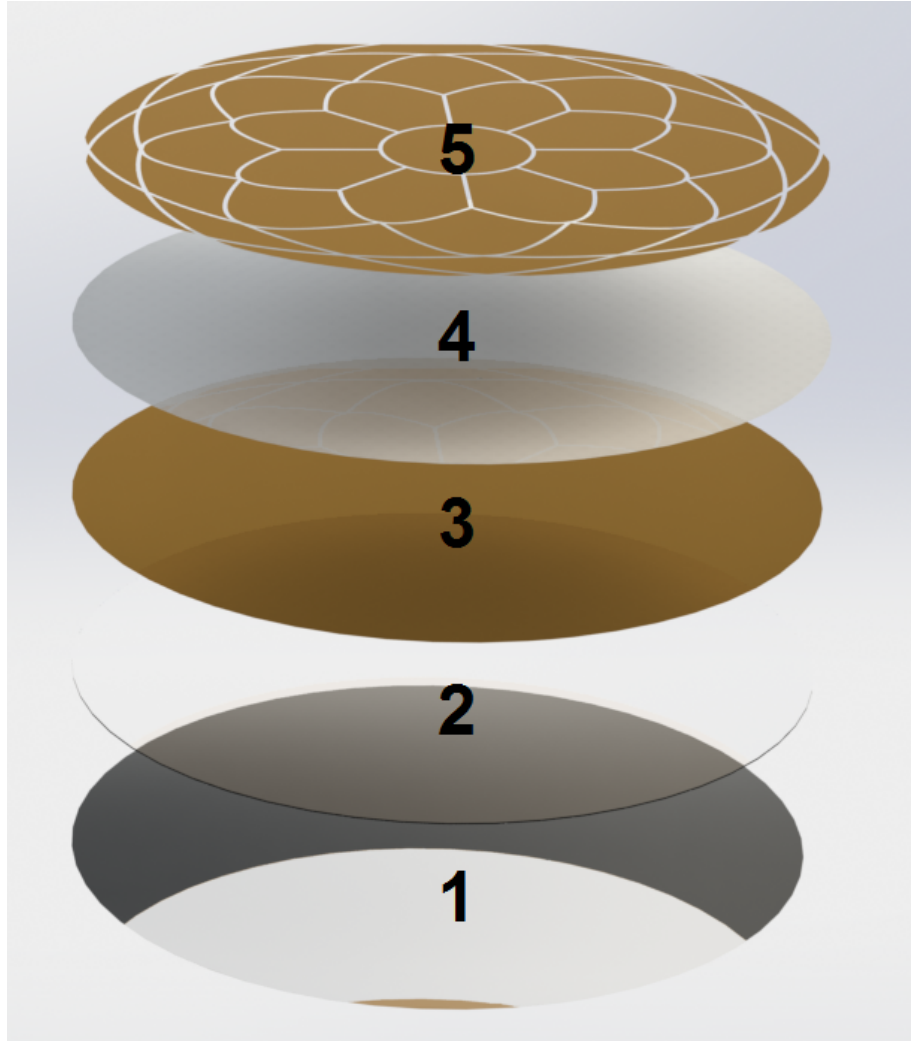


Figure 7.1: Design chosen for performance analysis. See text for layer descriptions.

7.1.1 Vibration Model

The mirror can be modeled as a thin, flat glass plate of diameter, $2R$, and thickness, h , subjected to time (denoted t) varying pressure loads, p , on its surface, and able to deflect in a direction normal to the surface. The coordinate system is aligned to the center of the mirror, with the \hat{z} axis normal to the surface pointing out of the reflective side. The other coordinates can be represented by \hat{x} and \hat{y} axes for a Cartesian frame, or \hat{r} and $\hat{\theta}$ for a cylindrical frame. The deflection is denoted as $w(x, y, t)$ or $w(r, \theta, t)$. The governing equation for a thin plate can be written as:

$$\rho h \ddot{w} + D \nabla^4 w = p , \quad (7.1)$$

where ρ is the mass density, D is the plate bending stiffness, defined as:

$$D = \frac{Eh^3}{12(1-\nu^2)} , \quad (7.2)$$

and ∇^4 is the biharmonic operator. In cartesian coordinates, the biharmonic operator can be expanded as:

$$\nabla^4 () = \frac{\partial^4 ()}{\partial x^4} + \frac{\partial^4 ()}{\partial y^4} + \frac{\partial^4 ()}{\partial x^2 y^2} . \quad (7.3)$$

For an axisymmetric case, with no dependence on \hat{z} or $\hat{\theta}$, the operator can be expressed in cylindrical coordinates as:

$$\nabla^4 () = \frac{\partial^4 ()}{\partial r^4} + \frac{2}{r} \frac{\partial^3 ()}{\partial r^3} - \frac{1}{r^2} \frac{\partial^2 ()}{\partial r^2} + \frac{1}{r^3} \frac{\partial ()}{\partial r} . \quad (7.4)$$

The analytical solution for the freely vibrating case can be found by modal analysis and separation of variables. The deflection is written in the form $w(r, t) = \sum_{n=1}^{\infty} \phi_n(r) \eta_n(t)$, where ϕ_n is the unitless n^{th} natural mode shape and η_n is the time dependent modal amplitude with units of deflection. For each mode, separation of variables yields:

$$\frac{D}{\rho h} \frac{\nabla^4 \phi_n}{\phi_n} = - \frac{\ddot{\eta}_n}{\eta_n} = \omega_n^2 . \quad (7.5)$$

For the axisymmetric case, the solution is found to be:

$$\phi_n(r) = A_n J_0(\lambda_n r) + B_n I_0(\lambda_n r) \quad (7.6)$$

$$\eta_n(t) = C_n e^{i\omega_n t} + D_n e^{-i\omega_n t} \quad (7.7)$$

$$w(t, r) = \sum_{n=1}^{\infty} (A_n J_0(\lambda_n r) + B_n I_0(\lambda_n r)) (C_n e^{i\omega_n t} + D_n e^{-i\omega_n t}) , \quad (7.8)$$

where J_0 is the 0^{th} order Bessel function of the first kind, and I_0 is the 0^{th} order modified Bessel function of the first kind. The constants A_n and B_n can be computed from the applicable boundary conditions. C_n and D_n are determined by the initial conditions. λ_n and ω_n are the spatial and temporal eigenfrequencies, respectively, and are strictly positive real numbers, and are related via $\lambda_n^4 = \omega_n^2 \rho h / D$.

7.1.2 Forced Vibrations

In order to analyze the forced vibration case, it helps to define the inner product of two spatial functions over the plate domain:

$$f(r) \cdot g(r) = \int_0^R f(r)g(r)r dr . \quad (7.9)$$

Additionally, the mode shapes are orthonormalized in the following sense:

$$\phi_n(r) \cdot \phi_m(r) = \int_0^R \phi_n(r)\phi_m(r)r dr = \begin{cases} 1, & \text{if } n = m. \\ 0, & \text{otherwise.} \end{cases} \quad (7.10)$$

This allows the governing equation 7.1 to be decoupled when the deflections and loading are projected onto the various modes. Assuming that the pressure loading can be separated into a spatial distribution and a temporal amplitude, $p(r, t) = \psi(r)\gamma(t)$, then it can be projected on the modal basis:

$$p(r, t) = \left(\sum_{n=1}^{\infty} \psi_n \phi_n(r) \right) \gamma(t) \quad (7.11)$$

$$\psi_n = \psi(r) \cdot \phi_n(r) = \int_0^R \psi(r)\phi_n(r)r dr \quad (7.12)$$

with the constants ψ_n representing the component of the loading that is present in each individual mode. ζ_n is the amplitude time history of the pressure loading.

Equation 7.1 can now be manipulated using 7.5 as follows:

$$\rho h \ddot{w} + D \nabla^4 w = p \quad (7.13)$$

$$\sum_{n=1}^{\infty} \rho h \phi_n \ddot{\eta}_n + \sum_{n=1}^{\infty} (D \nabla^4 \phi_n) \eta_n = p \quad (7.14)$$

$$\sum_{n=1}^{\infty} \rho h \phi_n \ddot{\eta}_n + \sum_{n=1}^{\infty} (\omega_n^2 \rho h \phi_n) \eta_n = p . \quad (7.15)$$

Now the convenient properties of the orthonormal modal basis are invoked to decouple the modes and remove the spatial dependence in the equation. The inner product is taken of both sides of Equation 7.15 with mode ϕ_m , and then reduced by orthogonality:

$$\int_0^R \phi_m \left(\sum_{n=1}^{\infty} \rho h \phi_n \ddot{\eta}_n + \sum_{n=1}^{\infty} (\omega_n^2 \rho h \phi_n) \eta_n \right) r dr = \int_0^R \phi_m p r dr \quad (7.16)$$

$$(\rho h \phi_m \ddot{\eta}_m + \rho h \omega_m^2 \eta_m) \left(\sum_{n=1}^{\infty} \int_0^R \phi_m \phi_n r dr \right) = \gamma \sum_{n=1}^{\infty} \psi_n \left(\int_0^R \phi_m \phi_n r dr \right) \quad (7.17)$$

$$\rho h \ddot{\eta}_m + \rho h \omega_m^2 \eta_m = \psi_m \gamma . \quad (7.18)$$

Now the equations are decoupled second-order ordinary differential equations (ODE) and only dependent on time. They can be solved quickly using tools such as MATLAB. Commonly, these types of ODE are computed using the Laplace transform operator, denoted $\mathcal{L}()$, and transfer functions. The Laplace variable is denoted as s . The transfer function between the transformed input, $\Gamma(s) = \mathcal{L}(\gamma(t))$, and output modal response transform, $H_m(s) = \mathcal{L}(\eta_m(t))$, can be written in the Laplace domain as follows:

$$\frac{H_m(s)}{\Gamma(s)} = \frac{\psi_m}{(\rho h)s^2 + (\rho h \omega_m^2)} . \quad (7.19)$$

The final mirror deflections can be computed by putting together the various modal responses. Depending on the desired number of modes, N , to be included in the model, the summation can be estimated:

$$w(r, t) \approx \sum_{m=1}^N \phi_m(r) \eta_m(t) \quad (7.20)$$

$$= \sum_{m=1}^N \phi_m(r) \mathcal{L}^{-1}(H_m(s)) \quad (7.21)$$

$$= \sum_{m=1}^N \phi_m(r) \mathcal{L}^{-1} \left(\frac{\psi_m \Gamma(s)}{(\rho h)s^2 + (\rho h\omega_m^2)} \right). \quad (7.22)$$

7.1.3 Modal Damping

The vibration model so far has only considered that the mirror is a homogenous glass plate. For obtaining the natural modes, this is a reasonable assumption since the soft polymer layer and thin metal coating layers do not contribute significantly to the overall stiffness or mass of the mirror. However, the glass substrate does not have significant damping, whereas the presence of the polymer on the outside of the substrate can contribute significantly to damping in the system.

To avoid needing to reconsider the governing equation with an included material damping term, the simplest way to include its effect is to introduce modal damping coefficients, ζ_m . The damping coefficients can be measured experimentally by using a logarithmic decrement method. This allows the free vibration modes to remain valid. Equations 7.18, 7.19, and 7.22 are expanded to include a viscous modal damping term:

$$\rho h \ddot{\eta}_m + 2\zeta_m \omega_m \rho h \dot{\eta}_m + \rho h \omega_m^2 \eta_m = \psi_m \gamma \quad (7.23)$$

$$\frac{H_m(s)}{\Gamma(s)} = \frac{\psi_m}{(\rho h)s^2 + (2\zeta_m \omega_m \rho h)s + (\rho h \omega_m^2)} \quad (7.24)$$

$$w(r, t) \approx \sum_{m=1}^N \phi_m(r) \mathcal{L}^{-1} \left(\frac{\psi_m \Gamma(s)}{(\rho h)s^2 + (2\zeta_m \omega_m \rho h)s + (\rho h \omega_m^2)} \right). \quad (7.25)$$

7.1.4 Example Case: Delta IV Launch

An example case is given here for a deformable mirror experiencing acoustics loads from a Delta IV launch vehicle. The mirror is assumed to be clamped on the edge (zero deflection and zero slope), and the center of the mirror is allowed to freely vibrate. The model parameters are displayed in Table 7.1. The natural modes are found by computing the appropriate A_n and B_n and λ_n for the functions in Equation 7.6. Note that this is a nonlinear root-finding step, and is very sensitive to the choice of initial search values. The first three computed modes are displayed in Figure 7.2 and normalized such that their inner product as defined in the previous Section is unity.

Table 7.1: Acoustic vibration model parameters.

	Value
Radius, R	50 mm
Glass thickness, h	0.2 mm
Density, ρ	2230 kg/m ³
Elastic modulus, E	65 GPa
Poisson's ratio, ν	0.2
Bending stiffness, D	0.0451 N-m

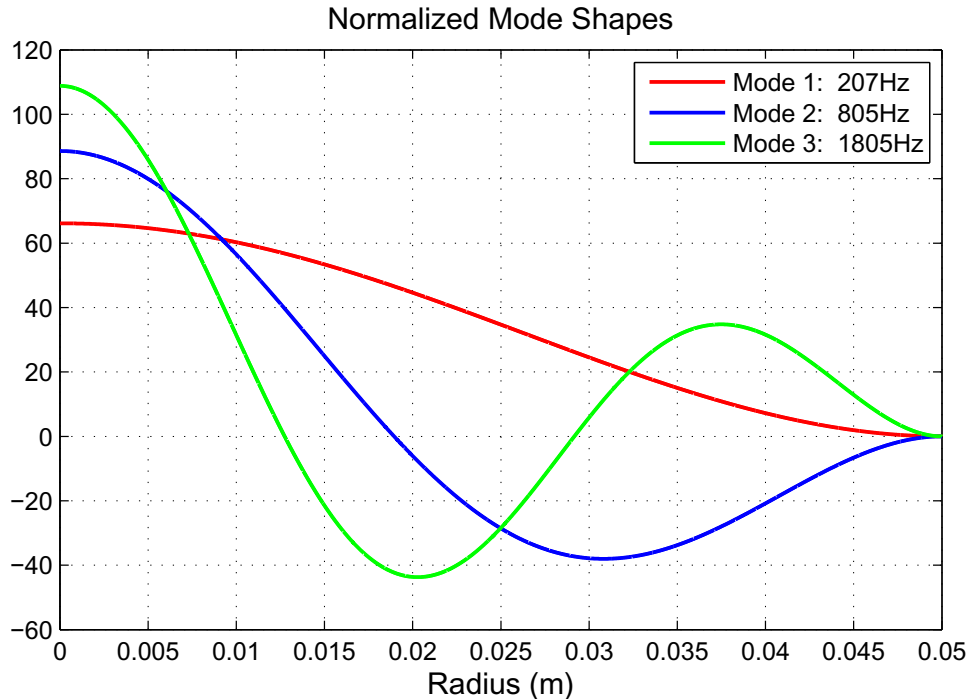


Figure 7.2: Axisymmetric vibrational modes of the deformable mirror. Scaled for a unity inner product over mirror disk.

7.1.4.1 Mirror Damping Estimation

The modal damping coefficient can be obtained by experimentally measuring the mirror impulse response data. The experiment was performed by holding the mirror in an upright position by holding it (pinned) at three points spaced 120° apart near the edge. A small metal sphere was tossed at the mirror and the natural modes were excited after it impulsively collided with the mirror surface. The center deflection of the mirror was monitored using a Keyence laser vibrometer. Several time histories of the deflections normalized by the peak value are plotted in the top left of Figure 7.3. The Fast Fourier Transform (FFT) of the data is shown to the right with three modes present below 300 Hz. The distribution of vibrational energy between the modes in each trial was dependent on the impact speed and location of the sphere, and so the relative

amplitude of the peaks varies.

For each trial dataset, a summation of three single degree-of-freedom response functions were fitted to the data. These response functions were of a form as shown in Equation 7.24, with parameterization for the amplitude, natural frequency, and modal damping coefficients. The complex amplitude of this function was then best fitted to the experimental data amplitudes using MATLAB’s “`nlinfit`” function. The fitted functions are show in the bottom right plot. The fitted amplitudes were then paired with the measured phase values and its inverse Fast Fourier Transform (iFFT) taken to reproduce the time histories in the bottom left.

The first two modes of this 3-point pinned mirror were not of interest here because they corresponded to twisting modes similar to optical trefoil. However, the third mode (221 Hz) was very similar to the first mode for the axisymmetrically clamped mirror (207 Hz). This was confirmed by checking the mode shapes of a 3-point pinned plate in an Abaqus FEM. The fitted damping coefficients (ζ_n) for the third mode were found to be in the range of 0.005 to 0.007, and will be used for the modeling of launch vibrations.

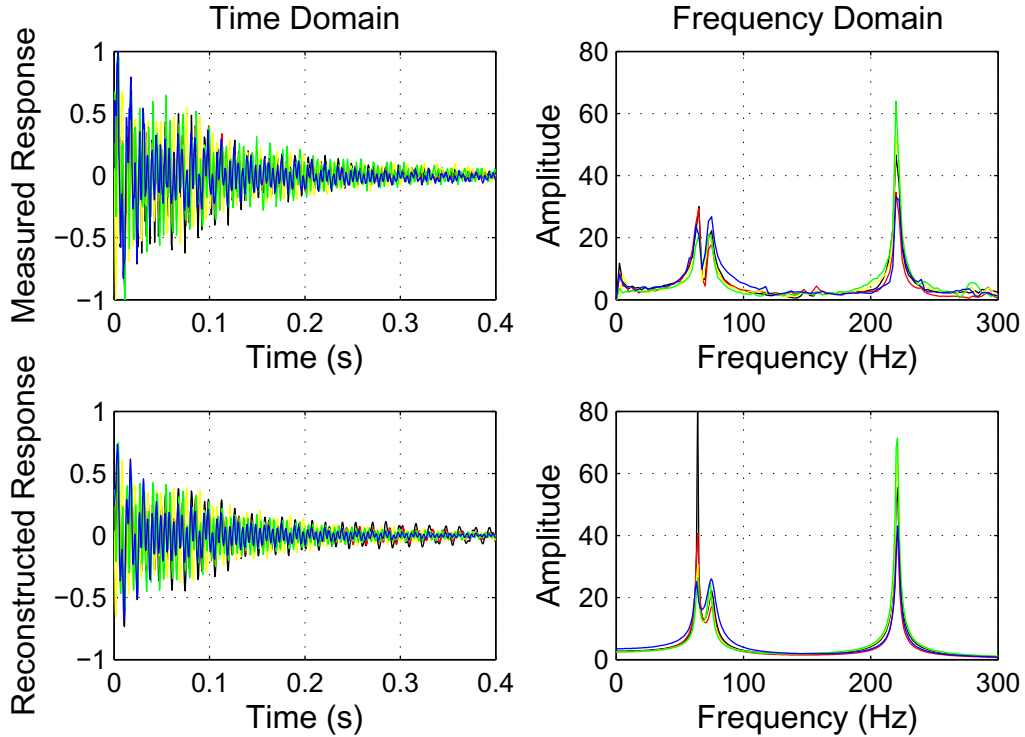


Figure 7.3: Measured impulse response of mirror in time and frequency domains (upper plots). Three single DOF vibration models were fitted to the data to reconstruct the behavior and extract modal damping estimates (lower plots).

7.1.4.2 Loads and Response

The acoustic pressure loads can be estimated based on launch environment specifications typically provided in the launch vehicle handbook provided by the rocket manufacturers. For this example, the chosen launch vehicle is the United Launch Alliance's Delta IV, with acoustic loads reported in the handbook [44]. The acoustic loads reported in the document are randomized by multiplying the design envelope magnitudes by random phases. The spectrum is then converted into a time history by taking the iFFT. An example random noise history is shown in Figure 7.4.

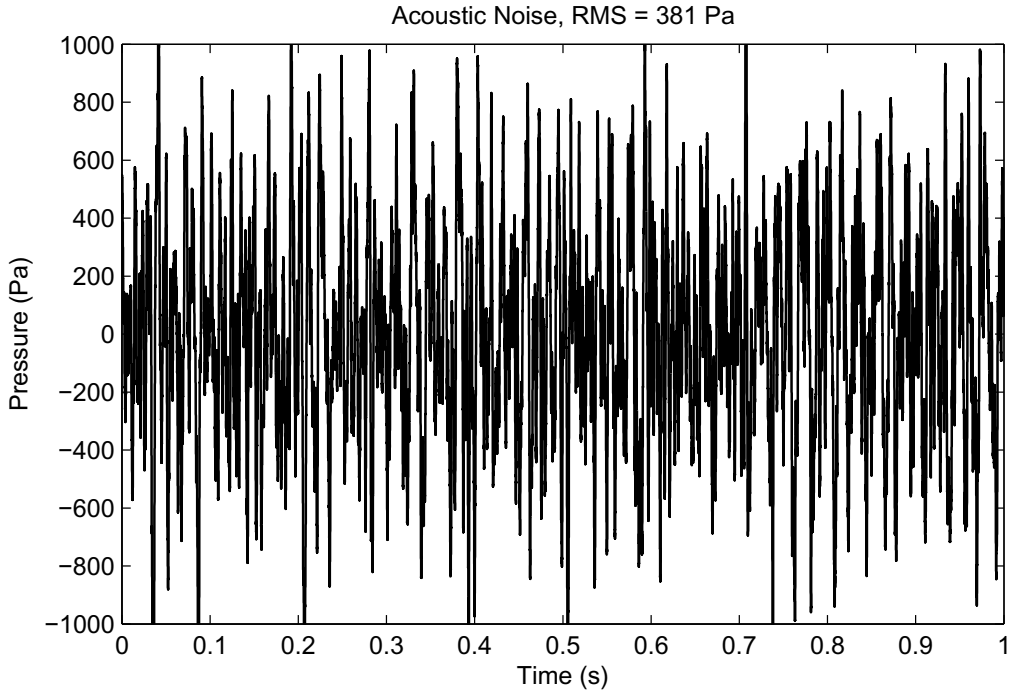


Figure 7.4: Representative random acoustic noise estimated from Delta IV launch environment specification.

The transfer functions from Equation 7.24 using damping values of 0.0067 are plotted in Figure 7.5 along with the acoustic spectrum. Note the orders of magnitude between each of the modal responses. A simple analysis with only the first mode is likely sufficient to capture the general behavior of the mirror. The deflection response of the mirror center point is plotted in Figure 7.6 in units of millimeters. The response of the first mode is orders of magnitude greater than the second mode and third mode. The RMS deflection is approximately 5.5 mm with some peaks over 15 mm. These are sufficiently large response predictions in this example to underscore concerns for thin mirror launch survivability.

Possible avenues to allow thin mirrors to survive launch include additional restraint points (boundary conditions), reduction of the acoustic loading through the means of a packaging scheme that attenuating the pressure loads that reach the mirror surface, and through active or passive use of the actuators to shunt

mechanical vibrational energy into electrical energy and then dissipated through resistive heating.

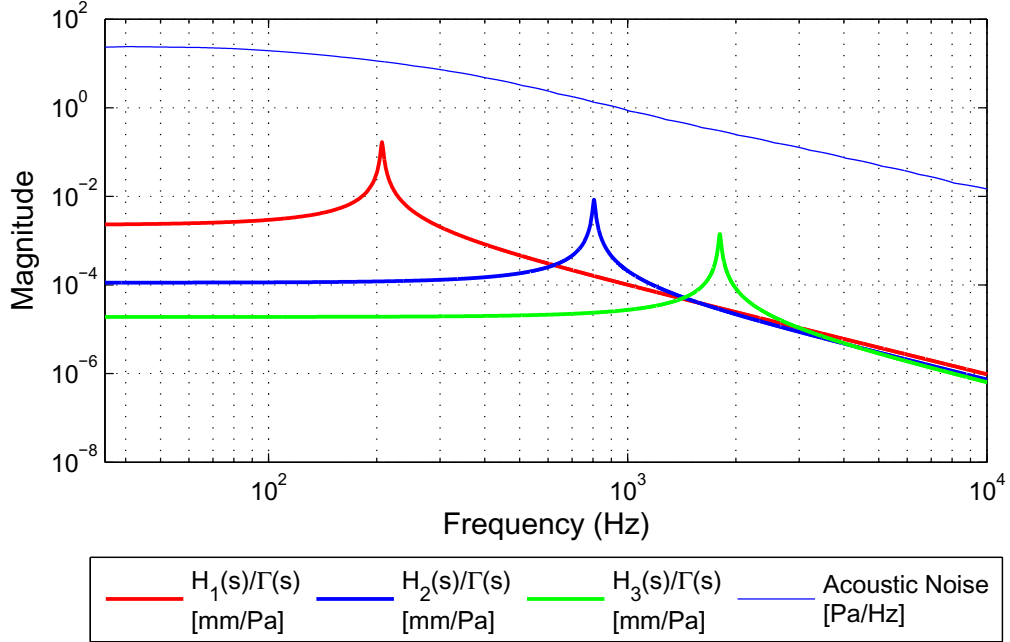


Figure 7.5: Mirror vibration transfer functions for first three modes. Also shown is the spectrum of the acoustic loading.

7.2 Mirror Shape Stability for Imaging

7.2.1 Vibrational Disturbances

The mirrors will experience disturbance vibrations on orbit from reaction wheels and other moving mechanisms. These vibrations could be in the form of accelerations of the mirror's boundary conditions that induce shape deformations via internal inertial forces. With only vacuum on the mirror surfaces, there are no externally applied pressure loadings. The analysis of the vibrational disturbances can proceed in a similar manner to the previous section, with some caveats.

In an imaging mode, the mirror will be held only at three points near the edge in order to allow for the active shape correction. These are different boundary conditions compared to the previous section, and our solution approach should now take into account the fact that the deflections need no longer be axisymmetric. The domain is now in Cartesian, x and y . Due to the complexity of solving for the eigenmodes in two dimensions, it is easier to use a FEM package (such as Abaqus) to compute the modes. The inner product is redefined then as:

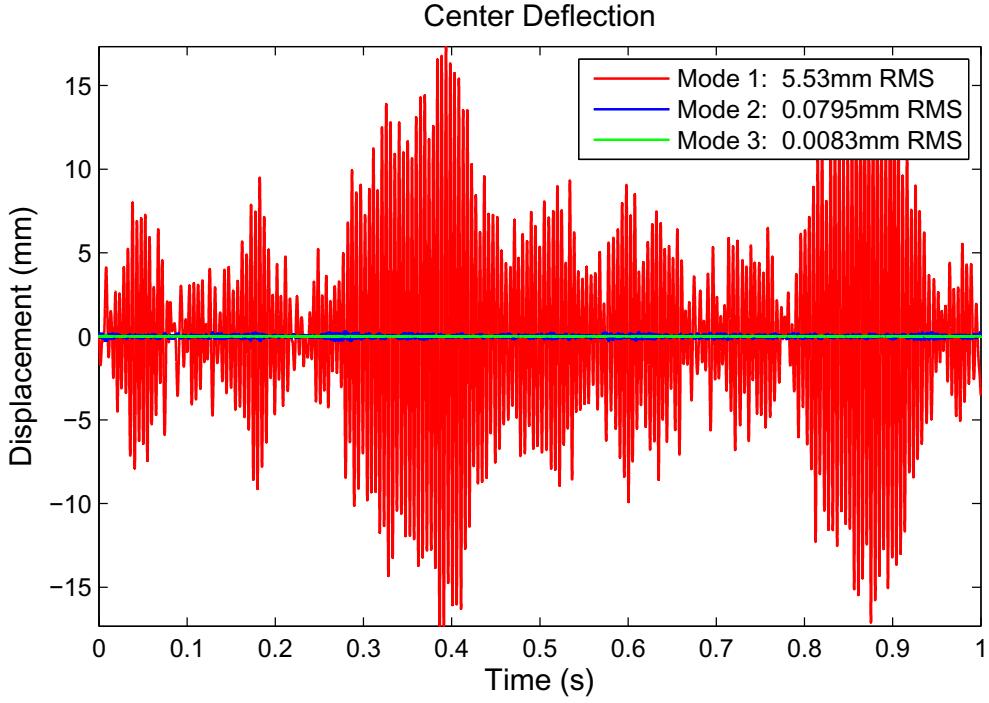


Figure 7.6: Mirror center deflection due to vibration input for the first three modes. The first mode dominates the response.

$$f(x, y) \cdot g(x, y) = \int_{-R}^R \int_{-R}^R m(x, y) f(x, y) g(x, y) dx dy, \quad m(x, y) = \begin{cases} 1, & \text{if } x^2 + y^2 \leq R^2 \\ 0, & \text{otherwise} \end{cases}. \quad (7.26)$$

The FEM eigenmodes can be read into MATLAB and resampled onto a desired domain grid using the function “`triscatteredinterp`”. They are then orthonormalized using the revised inner product definition.

The boundary accelerations can be accounted for by splitting the plate deflections into two components, $w = w_{flat} + w_{tilt}$, where w_{flat} is the mirror deflection assuming stationary boundary points, while w_{tilt} is in the form $ax + by + c$ so as to add the needed correction for the 3 boundary conditions. The governing equation for the plate is rewritten:

$$\rho h (\ddot{w}_{flat} + \ddot{w}_{tilt}) + D \nabla^4 (w_{flat} + w_{tilt}) = 0 \quad (7.27)$$

$$\rho h \ddot{w}_{flat} + D \nabla^4 (w_{flat}) = -\rho h \ddot{w}_{tilt} - D \nabla^4 w_{tilt}. \quad (7.28)$$

Note that by defining the tilt deflection as a plane, the stiffness term for w_{tilt} reduces to zero. This

makes sense because for small deflections a planar tilt is a rigid body motion and does not cause any internal stresses. The only remaining new term is $\rho h \ddot{w}_{tilt}$ which can be interpreted as the induced inertial loading caused by the boundary inputs. The analysis then proceeds in the same way as the previous section, except that now there are 3 inputs to the system rather than 1, and the system modal responses should be summed across all 3 inputs.

The loading accelerations from the spacecraft reaction wheels can be estimated by measuring their force and torque time histories due to wheel imbalances. To first order, the spacecraft can be modeled as a rigid body with a given mass and rotational moments of inertia. The linear and rotational accelerations of the rigid body spacecraft can be computed from the wheel loadings. The components of the linear motion that acts normal to the mirror surface can be input as the piston, c , term, and is uniformly distributed across the surface. The tip, a , and tilt, b , terms can be computed similarly from rotational accelerations that act in directions orthogonal to the mirror normal. Note that the distribution of tip and tilt accelerations across the mirror surface depend on the mirror's position relative to the spacecraft's center of mass, as well as the mirror orientation relative to the spacecraft. Therefore, the tip and tilt terms in general are not uniformly distributed across the mirror.

Greater accuracy in the model can be achieved by treating the spacecraft as a flexible body and measuring the accelerations of the mirror mounts. However, this is beyond the scope of this current research, and would require a detailed FEM of the spacecraft mechanical components.

7.2.1.1 Example Case: Reaction Wheel Vibration Effect on Image Quality

For now, a simple study was done assuming that the spacecraft is rigid. The force and torques of a reaction wheel were measured at various steady wheel speeds, and the accelerations on the mirror were estimated using conceptual mass and inertias of the spacecraft, and assuming that the spacecraft is equipped with 4 identical wheels in a tetrahedral formation near the center of mass. Exemplary time histories of the piston, tip, and tilt accelerations are plotted in Figure 7.7.

The modal responses of the mirror were computed in a fashion similar to the launch acoustics example, but using eigenmodes from an Abaqus finite element model. At each time step of the mirror response, the image PSF was estimated by the Fraunhofer intensity diffraction pattern from the mirror deflection errors. The Fraunhofer pattern can be computed by taking the 2D Fourier transform, denoted $\mathcal{F}()$, of the complex-valued mirror pupil function:

$$\text{PSF}(x', y', t) = \left| \mathcal{F} \left(m(x, y) e^{2\pi i \cdot 2w_{\text{flat}}(x, y, t) / \lambda} \right) \right|^2. \quad (7.29)$$

λ here is the wavelength of interest; 633 nm was used in this analysis. The image plane coordinates

are denoted x' and y' . The PSF intensities were then summed over a time interval to simulate a camera exposure. Two sets of cases are shown. The first set of images, shown in Figure 7.8, applied a 50-ms exposure for each case of the wheel speeds. The second set, shown in Figure 7.9, used an auto exposure time in the sense that every image had the same peak intensity. Note how, as the wheel speeds increase, the loading amplitudes increase, and the loading frequencies approach the mirror's natural frequencies. This causes the mirror vibration modes to become excited and produce the aberrations shown in the images. This causes both a loss of peak intensity and contrast, as best exhibited in the first set, and a loss of resolution as best exhibited in the second set.

This simple analysis suggests that the mirror's low natural frequencies may cause jitter to be a concern if the spacecraft reaction wheels or other disturbance generators are operating during an imaging mode. Ideally, the mirror wheels should be despun to the lowest practical speeds in order to minimize resonances with the flexible mirrors. If the mirror's natural frequencies are too low, and/or it is impractical to lower the wheel speeds enough, then one possible mitigation is to use the actuators in a dynamic sense to suppress the resonance. However, this would require additional complexity and mass of shunting electronics, which would need to be folded into the mirror control boards.

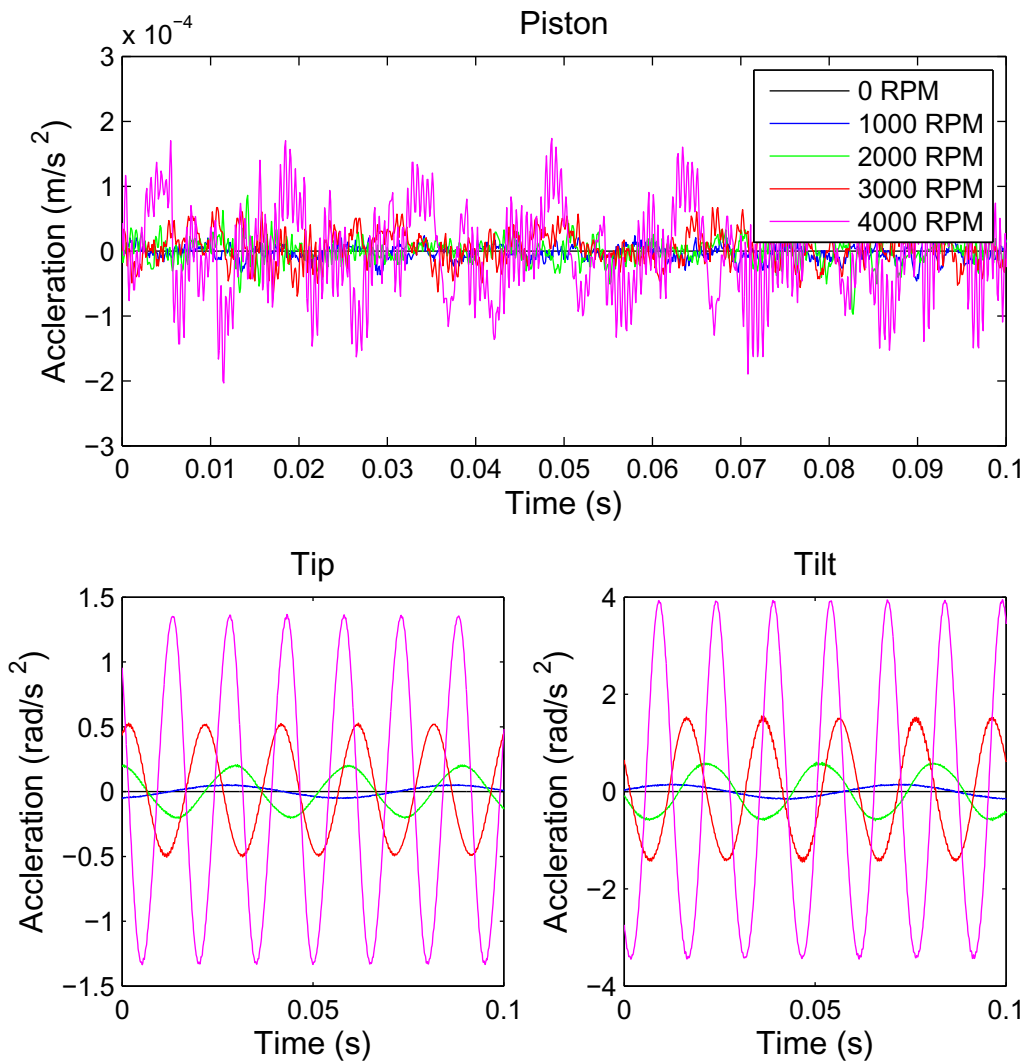


Figure 7.7: Time histories of piston, tip, and tilt accelerations used as imposed boundary conditions in mirror jitter model.

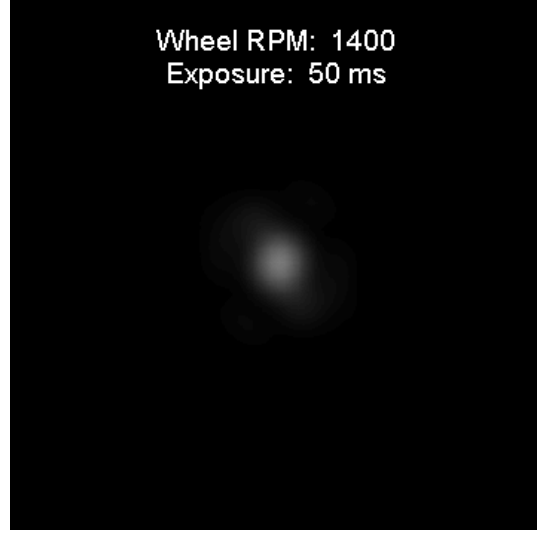
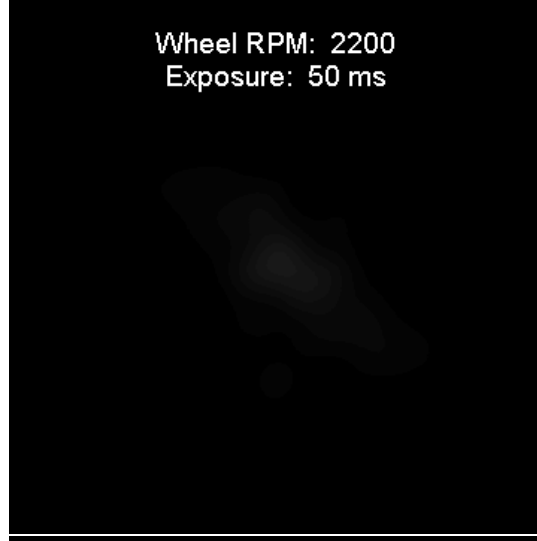
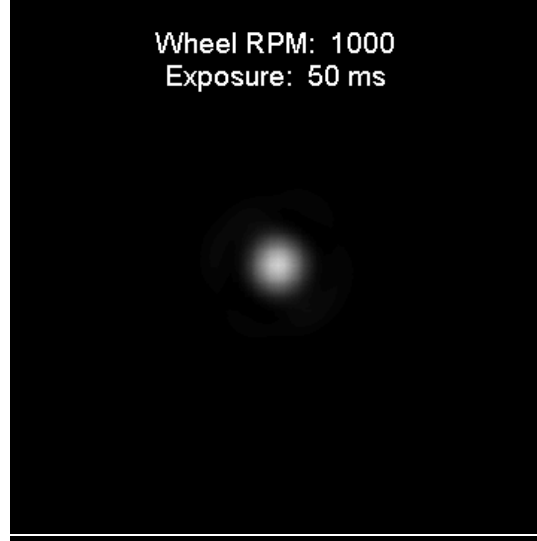
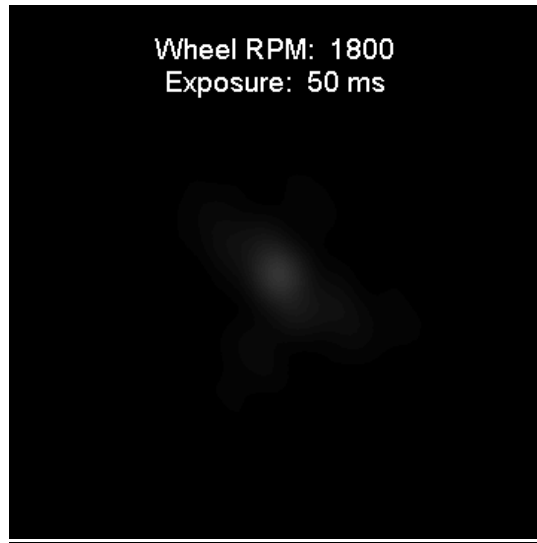
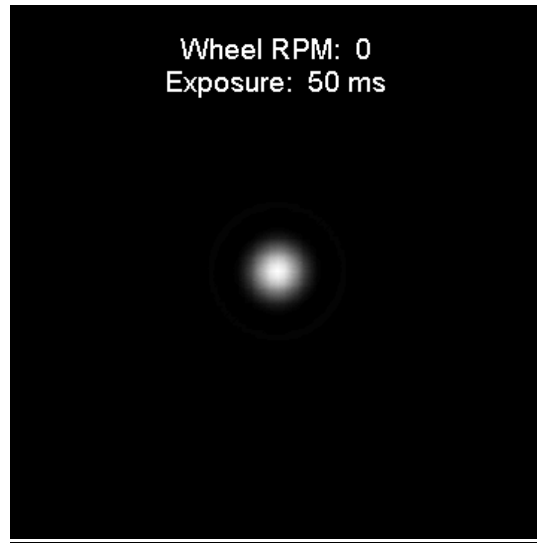


Figure 7.8: Simulated spot image blurring due to mirror jitter from reaction wheel vibrations with constant exposure times.

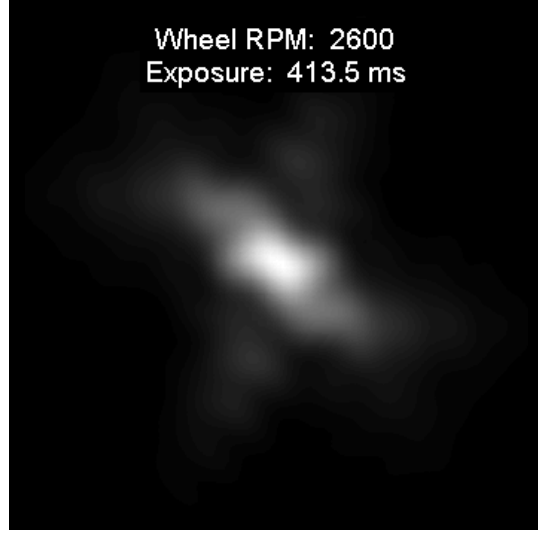
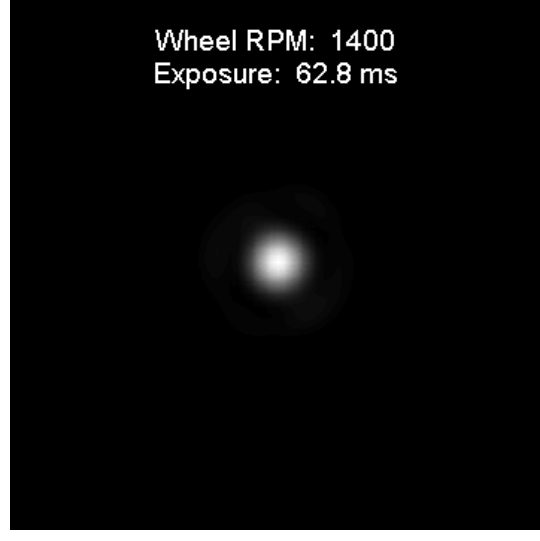
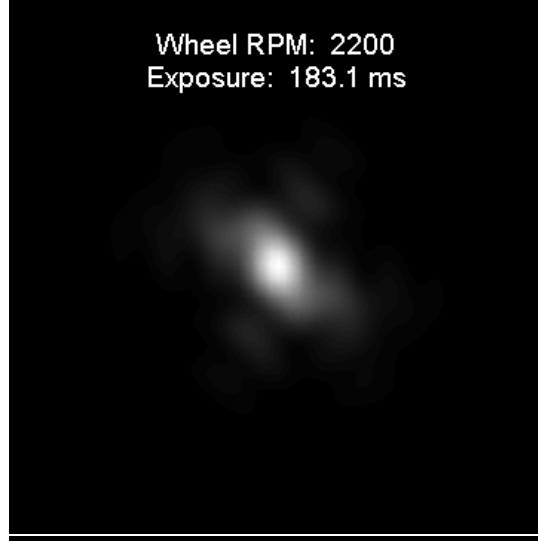
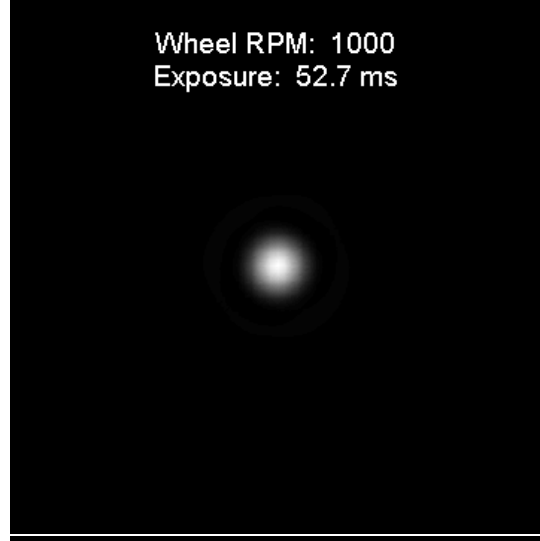
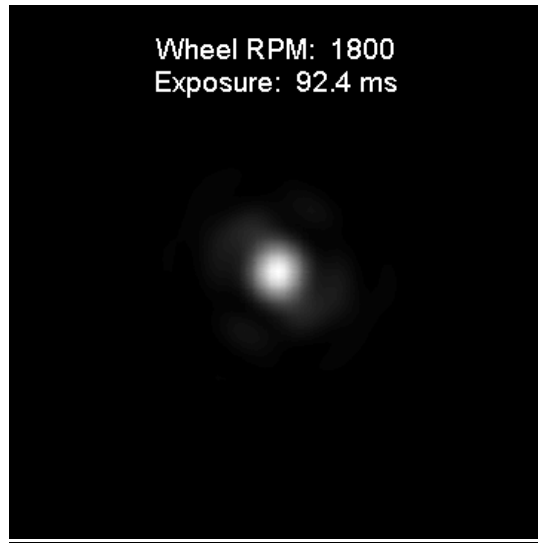
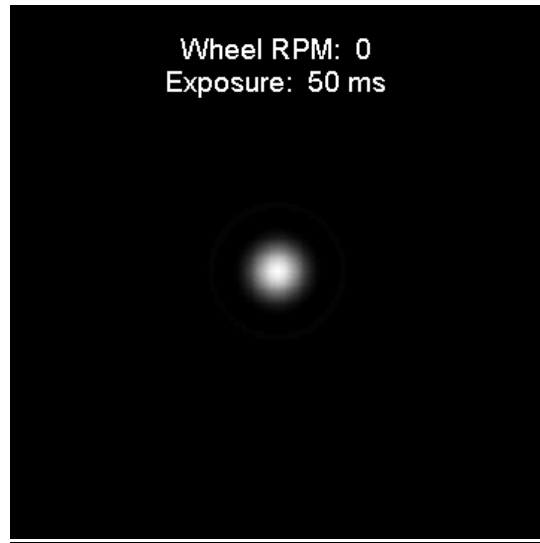


Figure 7.9: Simulated spot image blurring due to mirror jitter from reaction wheel vibrations with adjusted exposure times.

7.3 AAReST Closed-Loop System Performance Model

This section covers the numerical modeling of the deformable mirror's optical performance when inserted into the AAReST telescope system mentioned previously in Section 1.2.2. The model is used to predict the wavefront errors (WFE) and focused spot sizes for the actively controlled telescope. The optical properties of the telescope, misalignments, and temperature variations are included in the model. Shape control feedback from a Shack-Hartmann (S/H) wavefront sensor is used in order to close the loop with the mirror.

7.3.1 AAReST Telescope Operation Overview

The demonstration telescope is a prime focus design with the primary mirror divided up into a sparse aperture. A concept picture and optical schematic are shown in Figures 7.10 and 7.11. The primary segments are an arrangement of four 10-cm-diameter mirror packages attached to 3-unit sized Cubesats. Two of the mirrors are rigid reference mirrors, and two of them are active. All are mounted on gimballed piston/tip/tilt stages. A combined mirror package and Cubesat is called a “mirrorcraft”. The telescope will be launched as a small secondary payload in a stowed state, in which the camera package will be stowed by folding up a lightweight, deployable carbon fiber boom. The camera package includes an imaging detector, used to align the telescope segments and to collect PSF data, a Shack-Hartmann wavefront sensor to measure the mirrors' shapes, lenses for reimaging the pupil and focusing star images, as well as an adjustable mask for stray light control.

For calibration, the AAReST telescope will be pointed to a bright star. The image of the star from each segment is positioned on the detector and its size coarsely minimized by adjusting each segment through piston, tip and tilt corrections. Then, the wavefront error, as measured by the Shack-Hartmann, is minimized by adjusting the shape of each deformable mirror. During this process, each mirror must generate a unique aspheric shape corresponding to its position in the parent aperture. Each ideal shape is not uniquely defined; rather, it is a function of the telescope camera design lenses, any boom misalignments, and system thermal disturbances. The desired goal is to bring the wavefront error to $\lambda/10$ (for $\lambda = 540$ nm), and in turn, bring the measured spot sizes down to the order of the diffraction limit.

Once the initial calibration demonstration is completed, two of the mirrorcraft with the active segments will detach from the mirror cluster, perform a maneuver to reposition themselves at a new location in the array, and then redock to the cluster. If successful, this would demonstrate an analogue to autonomous on-orbit assembly of the mirrorcraft. Once the cluster is reassembled, the mirror calibration and imaging steps would be performed again in order to show the capability of the mirrors in various positions.

The telescope is launched in a narrow configuration, with a primary mirror total diameter of 34 cm, and it is reconfigured into a wide configuration, which is 58 cm in diameter. The focal length of the primary mirror is 1.2 m, and the camera package is designed to have a 0.4° field of view and to work in the visible

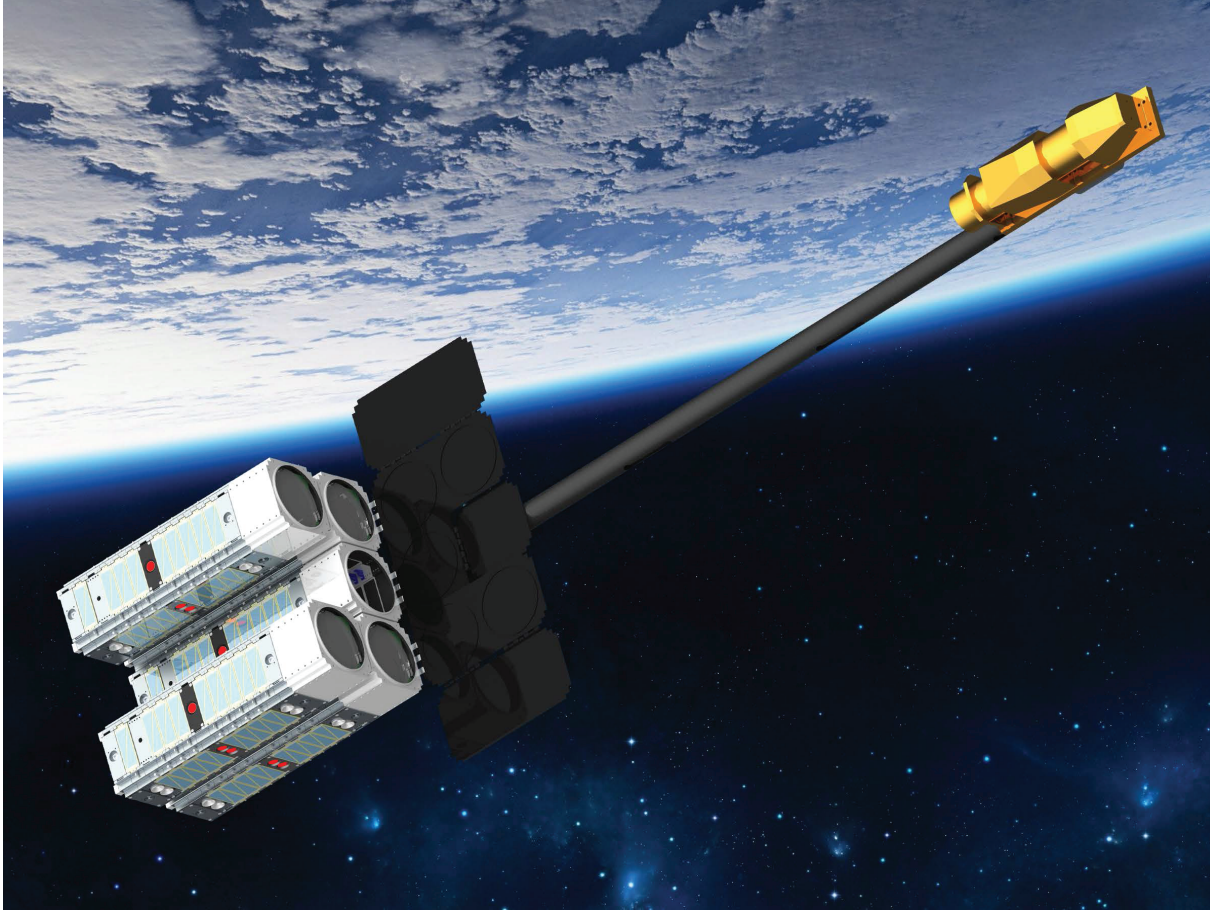


Figure 7.10: AAReST mission concept illustration.

wavelengths. Each active mirror is 100 mm diameter with a design discussed at the beginning of this chapter, and a 90-mm central clear aperture for each mirror.

The camera includes a set of lenses for light collimation, a mask for stray light, a beamsplitter, Shack-Hartmann wavefront sensor, a set of lenses for refocussing the collimated beam, and a detector. The optical model includes the lenses and the two light paths to either the Shack-Hartmann or to the camera. The optical elements and spacings for the Shack-Hartmann path are provided in Table 7.2. An equivalent table is given for the camera path in Table 7.3. Note that the two paths share the same primary element (the mirror), and the collimating lenses. The mask element is not included in the modeling, since it is only used for stray light control, and does not affect a single mirror element.

7.3.2 System Modeling

As each segment will operate in separate control loops, a single, spherically shaped mirror was modeled with an off-axis position corresponding to the compact or wide configurations of the telescope. The first step was

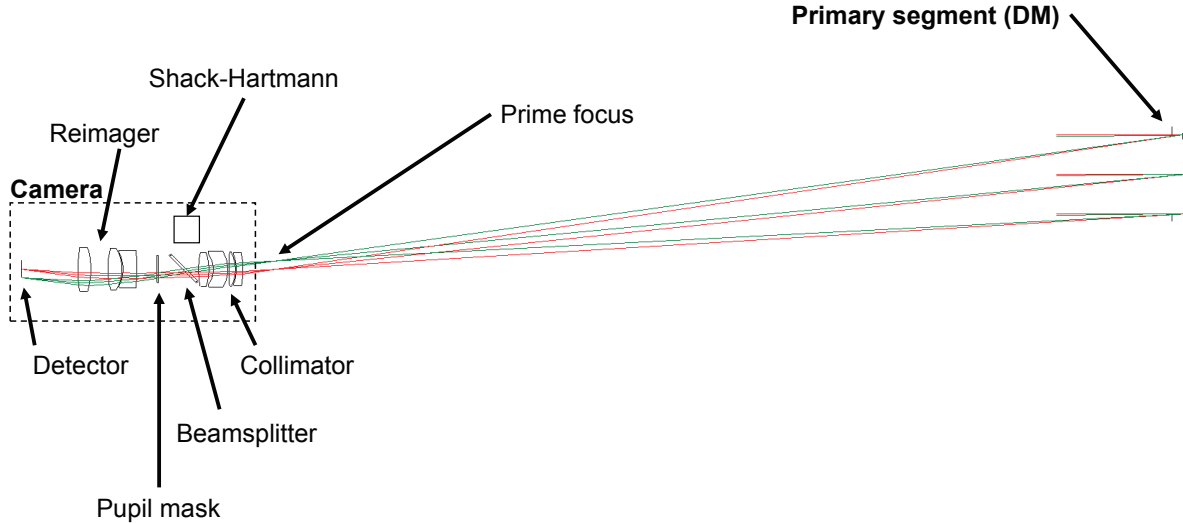


Figure 7.11: AAReST mission optical design layout.

to measure the performance of the perfectly spherical mirror in the as-designed system with no perturbations. Then, perturbations were introduced in the model, and the ability of the mirror to compensate for them was characterized. The considered sources of error for the current study capture the boom deflections that move the camera in a rigid body sense, thermal expansion of the camera's optical bench, mirror as-manufactured shape errors, and mirror thermal bending effects. Their current best estimates are presented in Table 7.4 from experiments and modeling, and were used in the model. As each source of error is assumed to be independent, a Monte Carlo analysis was performed to define numerous sets of perturbations to get representative statistics. The current study used 100 trials in the Monte Carlo runs.

The following set of software packages were used for the modeling: Code V for telescope ray tracing and sampling the Shack-Hartmann wavefront, Abaqus for finite element analysis, and MATLAB for running the Monte Carlo analysis and controlling the other software packages. The deformable mirror structure was modeled with finite element analysis, as explained in previous chapters. Note that the mirror is very slightly spherically curved in the application (≈ 1.2 m radius of curvature), but it was regarded as flat in the previous chapters for modeling and testing. The difference in the influence functions' shapes due to slight mirror curvature is assumed to be minor and is neglected for this analysis. Therefore, the recovered influence functions from the FEM were used in the loop simulation. The influences were converted into Zernike coefficients, and "measured" by the Shack-Hartmann in the raytrace model. A flowchart showing the inputs and outputs of the Monte Carlo sample trials is shown in Figure 7.12.

Table 7.2: Optical prescriptions for the path to the Shack-Hartmann sensor. Dimensions are in mm. Negative thicknesses are due to the change of direction after reflection from the deformable mirror.

No.	Surface	Radius	Thickness	Material	Diameter
0	Object	∞	∞	-	-
1	Entrance Pupil	∞	20	-	100
2	Deformable Mirror	-2326.1	-1163.05	-	100
3	Prime Focus	∞	-37.217	-	20
4	Collimator1	-96.807	-8.516	SF57_SCHOTT	40
5		-51.117	-1.21	-	40
6	Collimator2	-47.566	-8.12	NBK10_SCHOTT	40
7		219.174	-1.478	-	40
8	Collimator3	-44.604	-18.355	NZK7_SCHOTT	40
9		-32.717	-5.53	-	40
10	Collimator4	-63.758	-13.081	NBAK4_SCHOTT	40
11		107.869	-20	-	40
12	Beamsplitter	∞	-28.1615	-	60
13	Shack-Hartmann	∞	-	-	30

The effect of each source of error must be preliminarily characterized in order to be realistically simulated in the optical model. The following describes the various sources of error that were included. The boom is a flexible structure and will induce relative displacements and rotations between the mirror segment and the camera. It is simulated by moving the camera components around in 3 translational and 2 rotational degrees of freedom. It is assumed that rotation about the telescope axis does not have a significant effect on wavefront errors. Secondly, the modeled effect of temperature variation on the camera is a uniform modulation of the spacings of the optical elements based on an assumed CTE ($\alpha = 8.6\text{ppm}/^\circ\text{C}$) of the camera's titanium structure. This length scaling factor is $(1 + \alpha)(T - 20^\circ\text{C})$. The temperature of the mirror itself can produce bulk curvature changes due to thermal bending effects, as mentioned in previous chapters. The mirror as-manufactured error is modeled by adding Zernikes to the nominal spherical surface. The ranges are estimates based on preliminary experience with surface quality of several mirror prototypes made so far. These will likely need to be refined as the mirror design and fabrication process are finalized.

Once the perturbed optical performance is computed, the correction loop is closed, using the wavefront error in the pupil plane. To simulate the Shack Hartman (S/H) measurement, the wavefront optical path difference in the Shack-Hartmann plane is sampled in on a grid with spacing determined by the lenslet pitch. A smaller pitch allows measurement of higher spatial frequencies and a more accurate wavefront measurement, at the cost of decreased collecting area per lenslet and potentially reduced signal to noise ratio.

The S/H measurements are filtered to remove piston, tip, and tilt terms that correspond to rigid body motions of the mirror. The filtered measurement is used to feed the shape correction algorithm, while the tip and tilt are used in the mirror pointing controller. The system's "measured" influence functions are

Table 7.3: Optical prescriptions for the path to the imaging camera. Dimensions are in mm. Negative thicknesses are due to the change of direction after reflection from the deformable mirror.

No.	Surface	Radius	Thickness	Material	Diameter
0	Object	∞	∞	-	-
1	Entrance Pupil	∞	20	-	100
2	Deformable Mirror	-2326.1	-1163.05	-	100
3	Prime Focus	∞	-37.217	-	20
4	Collimator1	-96.807	-8.516	SF57_SCHOTT	40
5		-51.117	-1.21	-	40
6	Collimator2	-47.566	-8.12	NBK10_SCHOTT	40
7		219.174	-1.478	-	40
8	Collimator3	-44.604	-18.355	NZK7_SCHOTT	40
9		-32.717	-5.53	-	40
10	Collimator4	-63.758	-13.081	NBAK4_SCHOTT	40
11		107.869	-20	-	40
12	Beamsplitter	∞	-3	SILICA_SPECIAL	60
13		∞	-51.1615	-	30
14	Reimager1	-39.974	-30.004	NPSK53_S	40
15		59.352	-3.046	-	???
16	Reimager2	40.624	-2.999	SF1_SCHO	40
17		-213.448	-49.749	-	40
18	Reimager3	-14.022	-7.989	LAK33_SC	40
19		-13.8	-5	-	40
20	Detector	∞	-	-	10

sampled in the same way, and they must be combined in order to minimize the wavefront error. The optimal voltages are computed with a damped, constrained, least squares algorithm. The resulting mirror shape at each iteration is then injected into the optical model as Zernikes, and the corrected optical performance is computed. Once 5 iterations are completed, the camera detector is then moved in piston in order to do a final minimization of the image spot size. In practice, the mirror could be moved in piston instead of the detector for similar purposes.

7.3.3 Closed-Loop Performance Estimates

Eight different cases of the telescope configuration were considered with 100 Monte Carlo trials run for each. The variations between the cases were the compact or wide positions of the mirror, unlimited mirror voltages or ± 500 V limits, and sampling in the Shack-Hartmann of either 0.5 mm (≈ 10 samples per mirror diameter) or 0.2 mm (≈ 28 samples per mirror diameter). These various cases are used to gain insight into the importance of the S/H sampling on spot size performance, as well as the limitations of the mirror finite stroke.

The ideal goal is a measured wavefront error about $\lambda/10$ RMS and spot size close to the diffraction limit. Note that the measured wavefront error may not actually be the true value due to the limitation of

Table 7.4: AAReST performance modeling: injected errors range.

Error source	Min	Max
Temperature (°C)		
Mirror	-20	+20
Camera	-20	+20
Boom deflection: translation (mm)		
x translation	-0.625	+0.625
y translation	-0.625	+0.625
z translation	-0.127	+0.127
Boom deflection: rotation (°)		
Tip	-0.04	+0.04
Tilt	-0.04	+0.04
Mirror initial shape error (μm)		
Focus (Z4)	-0.005	+0.005
Astigmatism3 (Z5&Z6)	-0.002	+0.002
Coma3 (Z7&Z8)	-0.001	+0.001
Spherical3 (Z9)	-0.001	+0.001
Trefoil5 (Z10&Z11)	-0.001	+0.001
Tetrafoil7 (Z17&Z18)	-0.0005	+0.0005
Astigmatism5 (Z21&Z22)	-0.0005	+0.0005
Higher order terms (up to Z66)	-0.0001	+0.0001

Nyquist sampling in the spatial domain. However, the measured wavefront is important for the mirror shape control and has an effect on the spot size performance. The spot sizes were estimated using a highly sampled geometric spot diagram raytrace to the image plane. A circle centered on the centroid of the spots in the image plane was sized in order to capture 80% of the rays. This definition is used for the spot size. Note that this spot size estimator is geometric in nature and does not take into account diffraction effects, which become important close to the diffraction limit.

7.3.3.1 Wavefront Flattening

An example of a Monte Carlo trial is shown in Fig 7.13. We can note that it takes several iterations to converge to the optimal shape; this is due to a damping gain used in the correcting loop, allowing it to handle possible geometrical nonlinearity in the model, prevent overshoot, and to more closely emulate the algorithm that would likely be used in the mission.

Figure 7.14 presents the obtained wavefront performance results in the compact and wide modes. The correction in the compact mode for all 4 cases is roughly between 98% and 99.5% of the input error. The corrected wavefronts were extremely likely to come below $\lambda/10$. The results for the coarse (0.5 mm) S/H sampling tended to be artificially better than the finer (0.2 mm) S/H sampling, due to the invisibility of high spatial frequencies. The removal of voltage limits on the mirror allowed the wavefront performance to improve over the limited cases.

The correction in the wide mode was a bit worse than the compact case. Here the correction for all 4

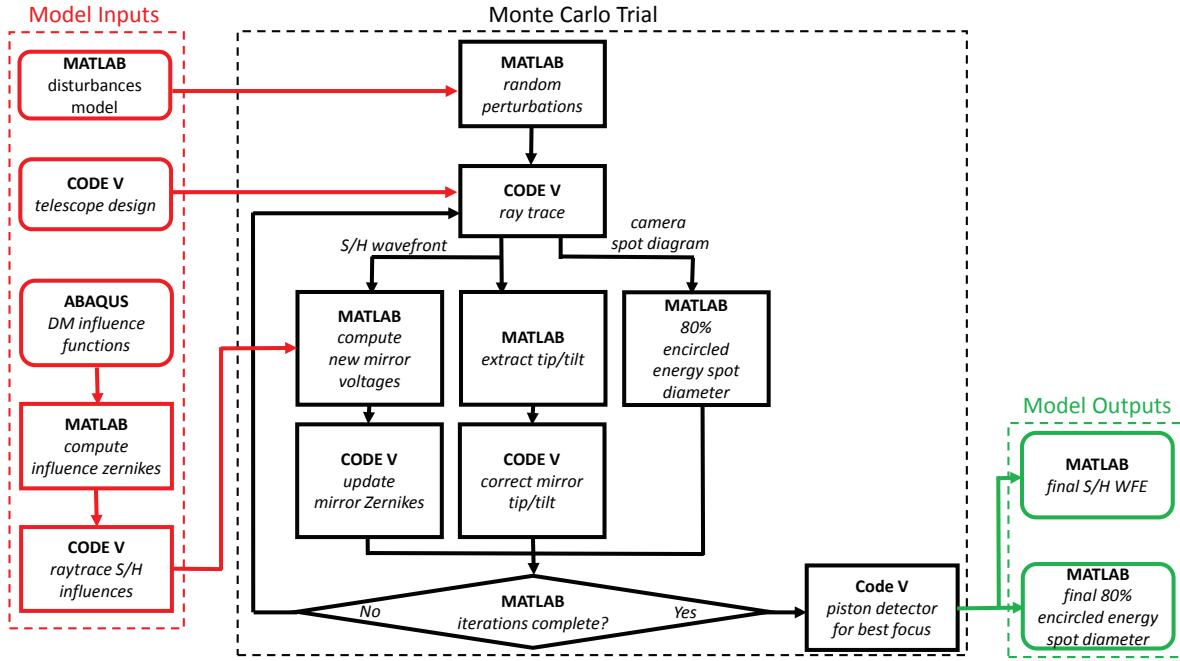


Figure 7.12: Flowchart showing how the telescope performance Monte Carlo model runs using three software packages: Abaqus, MATLAB, and Code V.

cases ranged between about 95% to 99.5%, with most final wavefront values below $\lambda/5$. This is due to the more challenging astigmatism requirement for the wide case, along with greater sensitivity of the system to disturbances. Again, measured wavefronts were artificially higher for the coarser S/H sampling, and could notionally be improved by unconstraining the mirror voltages.

7.3.3.2 Spot Size Reduction

Figure 7.15 presents the obtained spot diameter performance results in the compact and wide modes. The spot size reduction in the compact mode for all of the cases ranges between 85% to over 99% of the initial size. The corrected wavefronts were extremely likely to come below 4 times the diffraction limit. Finer sampling of the wavefront improved the spot size by preventing the mirror controller from over-correcting the low spatial frequencies at the expense of the higher frequencies. The removal of voltage limits also improves the performance, as expected.

Similar to the wavefront results, the spot sizes in the wide mode were worse than the compact case. Here the correction ranged between about 80% to over 99%, with most final spot sizes on the order of 4 times the diffraction limit or better. Again, finer S/H sampling allowed for improvement in the spot size control, especially in the unlimited voltage case, and less so in the constrained voltage case, indicating that

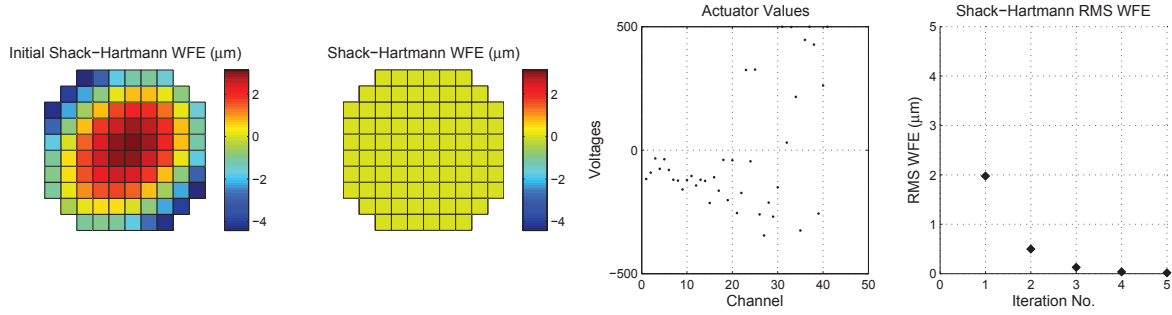


Figure 7.13: Example trial in the Monte Carlo system performance analysis.

the mirror may be running into stroke issues in the wide case.

7.4 Performance Summary

Both the wavefront and spot size results are satisfactory and give confidence in both mirror design and telescope optical configuration. Assuming that the input perturbations are realistic, then the mean wavefront performance can reasonably be expected to be about $\lambda/20$ for the compact configuration and $\lambda/10$ for the wide configuration. The spot sizes are on the order of 2 times the diffraction limit for the compact configuration and 4 times the diffraction limit for the wide configuration. The model has shown the importance of finely sampled S/H wavefront measurements, as well as the limitations of the mirror stroke in the wide configuration. Furthermore, the model has allowed the testing and verification of the wavefront control strategies, and could be used in the future to inform both further mirror fabrication and testing, as well as operational planning of the telescope.

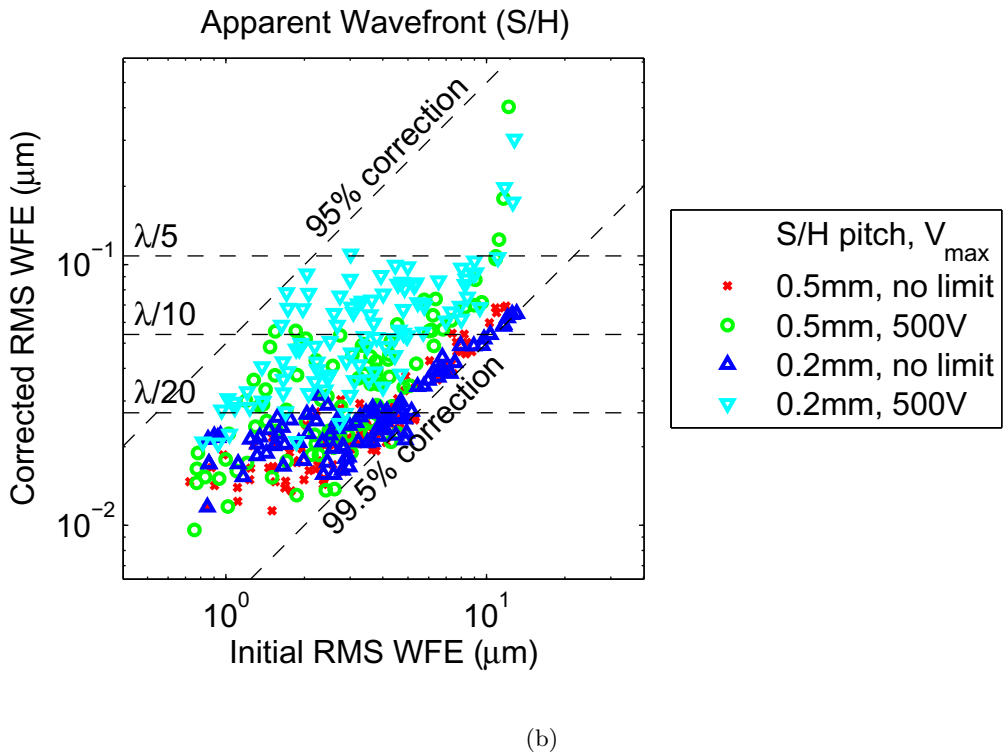
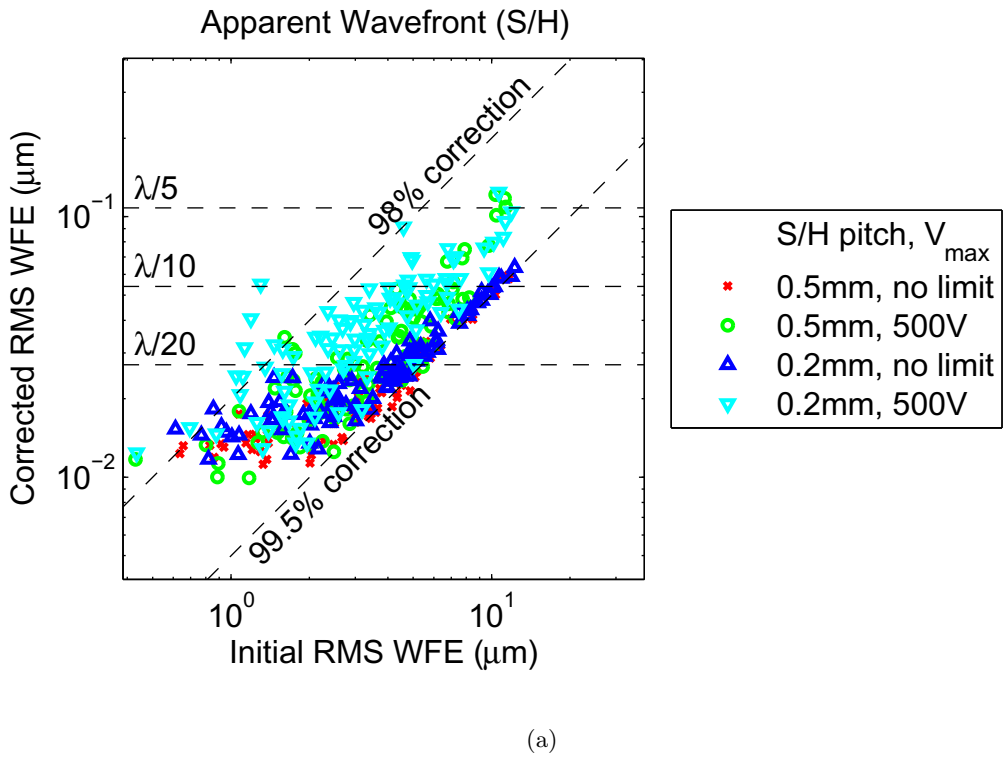
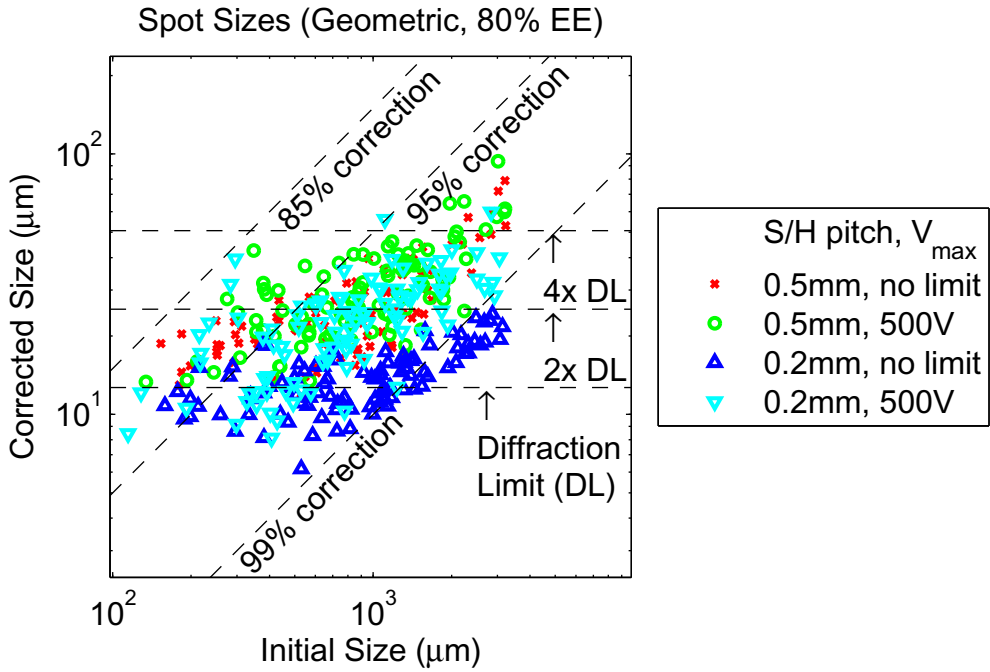
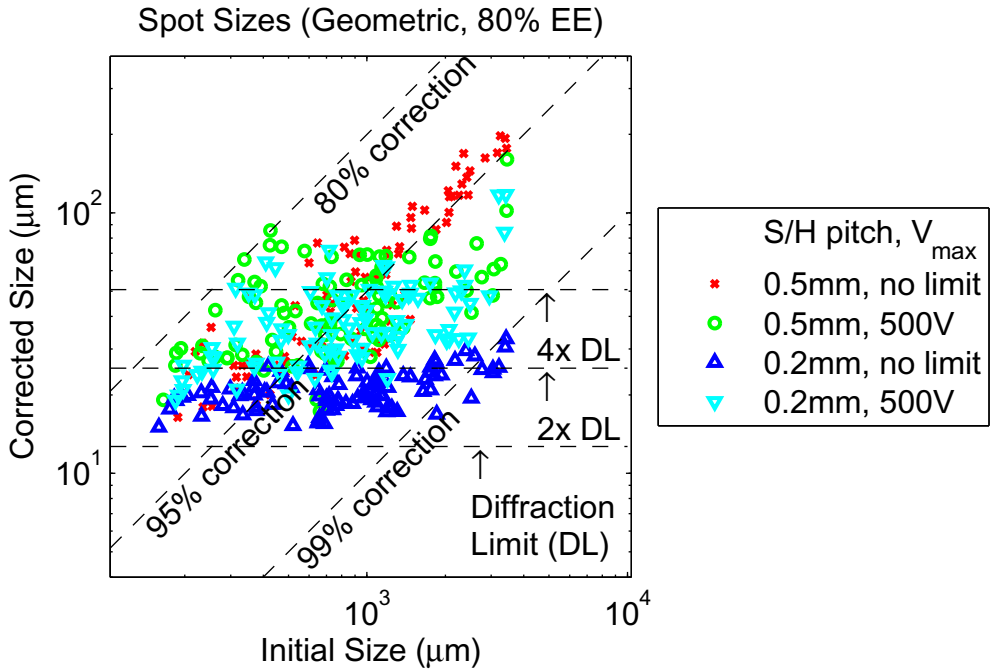


Figure 7.14: Telescope wavefront control performance, as measured by the Shack-Hartmann, of the (a) compact and (b) wide configurations for different cases of Shack-Hartmann sampling and mirror voltage limits. The reference wavelength is 540 nm.

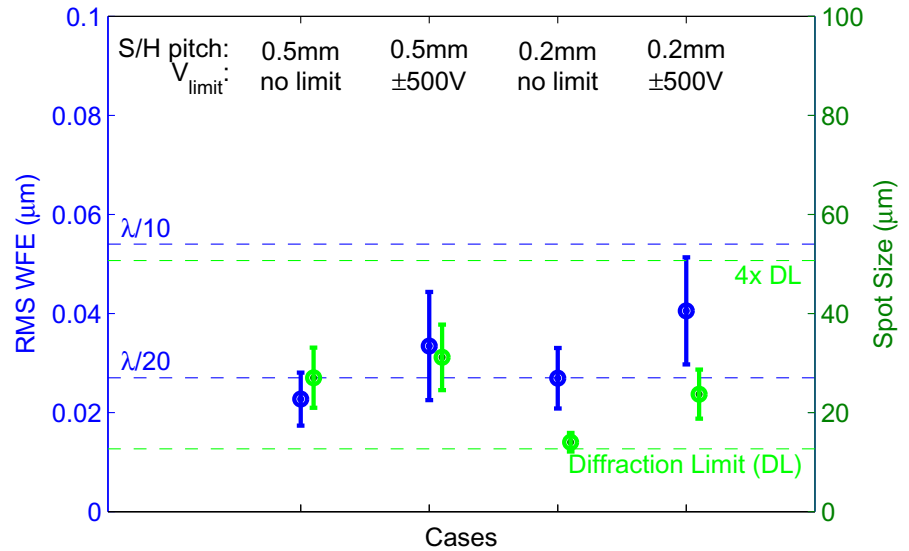


(a)

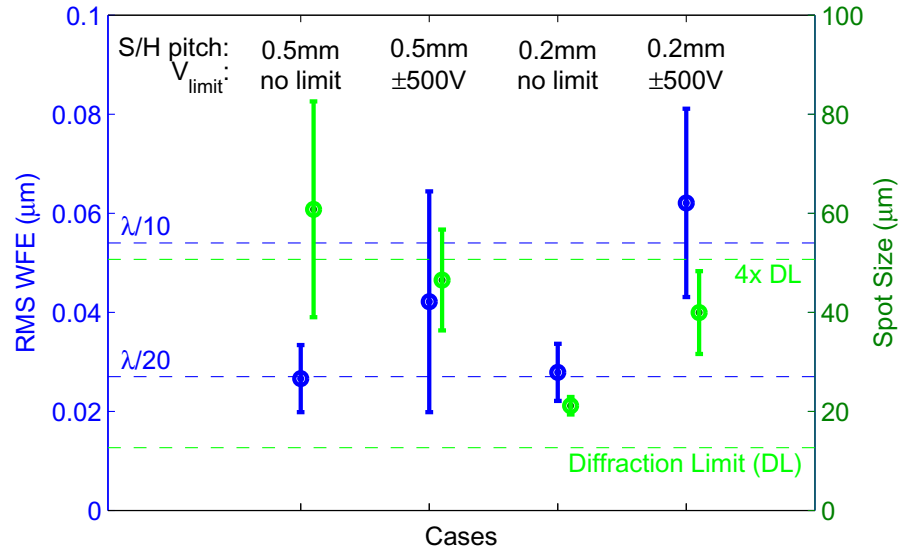


(b)

Figure 7.15: Telescope geometric spot diameter, using 80% encircled energy criteria, of the (a) compact and (b) wide configurations for different cases of Shack-Hartmann sampling and mirror voltage limits. The reference wavelength is 540 nm.



(a)



(b)

Figure 7.16: Summary of the wavefront and spot size performance distributions of the (a) compact and (b) wide configurations for different cases of Shack-Hartmann sampling and mirror voltage limits. The reference wavelength is 540 nm, and the error bars indicate one standard deviation of the distributions.

Chapter 8

Conclusion

This thesis has presented the argument for developing new, lightweight deformable mirrors so as to enable the construction of future large space telescopes. Identical, active spherical segments could populate the telescope's aperture and help to lower system costs by standardizing the segment design. The AAReST demonstration mission is used as a motivator for developing scaled deformable mirror prototypes. The conceptual design of a surface-parallel actuated mirror laminate has been described with integrated piezoelectric polymers.

Choices of laminate substrate material such as glass and silicon, reflective coatings such as gold and aluminum, and alternative active materials such as PZT have been covered. The fabrication process for making mirrors with glass substrates and P(VDF-TrFE) has been described with detail given for each of the processing steps, including shaping the substrate, coating the various layers, poling the active layer, and connecting and mounting the mirror.

The material behaviors, particularly the piezoelectric and viscoelastic P(VDF-TrFE), have been measured, described, and shown over a wide range of temperatures. These properties were then used to estimate the mirror behavior at different temperatures, and show a process by which the mirror thermal stability can be optimized without sacrificing stroke.

The mathematical formulation for computing the optimal shape control inputs has been covered. The use of actuator influence functions in a linear model allows for ease of control. A mirror's performance, both in correctability and stroke for various Zernike modes, can be estimated using a finite element model, and has been shown to allow actuator electrode design optimization. For isotropic, surface-parallel actuated mirrors without boundary control, the limiting mode for control is astigmatism. An optimized design that enhances the mirror's astigmatism performance, and will maintain good control of the other modes has been shown.

Experiments using an optical testbed with a wavefront sensor have demonstrated the validity of the shape control models. Experiments have been performed on 16-actuator and 41-actuator mirror prototypes. The design for a low mass and low power control electronics scheme suitable for a Cubesat-sized spacecraft was

shown and used to control the mirrors. The initial prototypes were able to achieve controlled figure errors on the order of a micron. This performance can be improved by using a substrate figuring process, such as thermal slumping for glass.

The analysis for determining a mirror's dynamic response to acoustic loading and other disturbances has been formulated, with example cases given for launch acoustics survival, and on-orbit jitter from reaction wheels. The limitations of thin laminates to surviving launch necessitates that care be taken when designing a mirror housing so that it attenuates acoustics loads, and uses optimal boundary conditions for pushing the mirror response modes to higher frequencies and lowering the overall deflections. Reaction wheel disturbances can have an effect of imaging performance depending on the magnitude of the wheel imbalances and the wheel's operating speed. Spinning down of the wheels prior to imaging, or using the mirror's actuators in a dynamic sense could mitigate this potential issue, and reduce image blur.

A numerical optical-thermal-mechanical model of the AAReST telescope was constructed to allow statistical performance estimation of the mirror shape control loop. The model included environmental perturbations such as temperature changes, as well as manufacturing tolerance allowances and misalignments. This model mapped out the acceptable ranges for mirror operations, and could be used in the future as a tool for fine tuning the telescope optical and control design, as well as creating manufacturing requirements on the flight mirrors. Using the current estimates for the disturbances, the model showed that the mirror design could likely provide near diffraction-limited imaging in both aperture configurations of the AAReST telescope.

Bibliography

- [1] BASTAITS, R., RODRIGUES, G., JETTEUR, P., HAGEDORN, P., AND PREUMONT, A. Multi-layer adaptive thin shells for future space telescopes. *Smart materials and structures* 21, 6 (2012), 064004.
- [2] BELY, P. *The design and construction of large optical telescopes*. Springer, 2003.
- [3] BORN, M., AND WOLF, E. *Principles of optics: electromagnetic theory of propagation, interference and diffraction of light*. Cambridge University Press, 1989.
- [4] BRECKINRIDGE, J., DOOLEY, J., AND PELLEGRINO, S. Large space apertures study report, 2009.
- [5] CAMBRIDGE GLASSBLOWING LTD. Glass Properties. <http://www.camglassblowing.co.uk/gproperties.htm>. Accessed: 11-7-2013.
- [6] CHEN, Q., NATALE, D., NEESE, B., REN, K., LIN, M., ZHANG, Q., PATTON, M., WANG, K., FANG, H., AND IM, E. Piezoelectric polymers actuators for precise shape control of large scale space antennas. In *The 14th International Symposium on: Smart Structures and Materials & Nondestructive Evaluation and Health Monitoring* (2007), International Society for Optics and Photonics, pp. 65241P–65241P.
- [7] COTRONEO, V., DAVIS, W. N., MARQUEZ, V., REID, P. B., SCHWARTZ, D. A., JOHNSON-WILKE, R. L., TROLIER-MCKINSTRY, S. E., AND WILKE, R. H. Adjustable grazing incidence x-ray optics based on thin pzt films. In *SPIE Optical Engineering+ Applications* (2012), International Society for Optics and Photonics, pp. 850309–850309.
- [8] DARGAVILLE, T. R., CELINA, M., ELLIOT, J., CHAPLYA, P., JONES, G., MOWERY, D., ASSINK, R., CLOUGH, R., AND MARTIN, J. *Characterization, performance and optimization of PVDF as a piezoelectric film for advanced space mirror concepts*. Sandia National Laboratories, 2005.
- [9] DE BLONK, B., MOORE, J., PATRICK, B., AND FLINT, E. Membrane mirrors in space telescopes. *Recent Advances in Gossamer Spacecraft* 212 (2006), 45–108.
- [10] EZOE, Y., SHIRATA, T., MITSUISHI, I., ISHIDA, M., MITSUDA, K., MORISHITA, K., AND NAKAJIMA, K. Shaped silicon wafers obtained by hot plastic deformation: performance evaluation for future astronomical x-ray telescopes. *Applied optics* 48, 19 (2009), 3830–3838.

- [11] FREUND, L. Substrate curvature due to thin film mismatch strain in the nonlinear deformation range. *Journal of the Mechanics and Physics of Solids* 48, 6 (2000), 1159–1174.
- [12] FREUND, L. B., AND SURESH, S. *Thin film materials: stress, defect formation and surface evolution*. Cambridge University Press, 2003.
- [13] GARDNER, J. P., MATHER, J. C., CLAMPIN, M., DOYON, R., GREENHOUSE, M. A., HAMMEL, H. B., HUTCHINGS, J. B., JAKOBSEN, P., LILLY, S. J., LONG, K. S., ET AL. The James Webb Space Telescope. *Space Science Reviews* 123, 4 (2006), 485–606.
- [14] HICKEY, G., BARBEE, T., EALEY, M., AND REDDING, D. Actuated hybrid mirrors for space telescopes. In *SPIE Astronomical Telescopes and Instrumentation: Observational Frontiers of Astronomy for the New Decade* (2010), International Society for Optics and Photonics, pp. 773120–773120.
- [15] HORANYI, M., HOXIE, V., JAMES, D., POPPE, A., BRYANT, C., GROGAN, B., LAMPRECHT, B., MACK, J., BAGENAL, F., BATISTE, S., ET AL. The student dust counter on the new horizons mission. *Space Science Reviews* 140, 1-4 (2008), 387–402.
- [16] HUBER, J., FLECK, N., AND ASHBY, M. The selection of mechanical actuators based on performance indices. *Proceedings of the Royal Society of London. Series A: Mathematical, Physical and Engineering Sciences* 453, 1965 (1997), 2185–2205.
- [17] KELLOGG, R. A., AND FLATAU, A. B. Blocked force investigation of a terfenol-d transducer. In *1999 Symposium on Smart Structures and Materials* (1999), International Society for Optics and Photonics, pp. 184–195.
- [18] KLEIN, R. *Concrete and abstract Voronoi diagrams*, vol. 400. Springer, 1989.
- [19] KUO, C.-P. Deformable-mirror concept for adaptive optics in space, 1991.
- [20] LASLANDES, M., HUGOT, E., FERRARI, M., HOURTOULE, C., SINGER, C., DEVILLIERS, C., LOPEZ, C., AND CHAZALLET, F. Mirror actively deformed and regulated for applications in space: design and performance. *Optical Engineering* 52, 9 (2013), 091803–091803.
- [21] LASLANDES, M., PATTERSON, K., AND PELLEGRINO, S. Active layer optimization in thin deformable mirrors. to be submitted in Applied Optics.
- [22] LINDLER, J., AND FLINT, E. Robustness of thin film shells with discrete boundary actuation. 47th AIAA/ASME/ASCE/AHS/ASC Structures, Structural Dynamics, and Materials Conference.
- [23] MOUNTAIN, C. M. The future of elts(extremely large telescopes): a very personal view. In *Proceedings of SPIE* (2003), vol. 5382, pp. 763–770.

- [24] NORTHROP GRUMMAN CORP. PMN Deformable Mirrors. http://www.northropgrumman.com/BusinessVentures/AOAXinetics/IntelligentOptics/Products/Documents/documentsheets/datasheet_PMN_Deformable_Mirrors.pdf. Accessed: 11-7-2013.
- [25] NORTON, A., EVANS, J. W., GAVEL, D., DILLON, D., PALMER, D., MACINTOSH, B., MORZINSKI, K., AND CORNELISSEN, S. Preliminary characterization of boston micromachines' 4096-actuator deformable mirror. In *SPIE MOEMS-MEMS: Micro-and Nanofabrication* (2009), International Society for Optics and Photonics, pp. 72090I–72090I.
- [26] PALIK, E. D. *Handbook of Optical Constants of Solids*. Academic Press, 1985.
- [27] PATTERSON, K., AND PELLEGRINO, S. Shape correction of thin mirrors. In *52nd AIAA/ASME/ASCE/AHS/ASC Structures, Structural Dynamics and Materials Conference* (2011), American Institute of Aeronautics and Astronautics.
- [28] PATTERSON, K., YAMAMOTO, N., AND PELLEGRINO, S. Thin deformable mirrors for a reconfigurable space aperture. 53rd AIAA/ASME/ASCE/AHS/ASC Structures, Structural Dynamics and Materials Conference.
- [29] PEARSON, D. D., CAVACO, J. L., ROCHE, J., ET AL. Multichannel, surface parallel, zonal transducer system, Mar. 23 2010. US Patent 7,683,524.
- [30] PEARSON, J., MOORE, J., AND FANG, H. Large and high precision inflatable membrane reflector. In *51st AIAA/ASME/ASCE/AHS/ASC Structures, Structural Dynamics, and Materials Conference* (2010), American Institute of Aeronautics and Astronautics.
- [31] PRAZISIONS GLAS OPTIK GMBH. D263 T Borosilicate Thin Glass. <http://www.pgo-online.com/intl/katalog/D263.html>. Accessed: 11-7-2013.
- [32] RAKIĆ, A. D. Algorithm for the determination of intrinsic optical constants of metal films: application to aluminum. *Applied optics* 34, 22 (1995), 4755–4767.
- [33] RODDIER, F. *Adaptive Optics in Astronomy*. Cambridge University Press, 1999.
- [34] ROMAINE, S., BRUNI, R., GORENSTEIN, P., PARK, S., REID, P., RAMSEY, B., AND KESTER, T. Platinum as a release layer for thermally formed optics for ixo. In *SPIE Astronomical Telescopes and Instrumentation: Observational Frontiers of Astronomy for the New Decade* (2010), International Society for Optics and Photonics, pp. 77323T–77323T–6.
- [35] SALINARI, P., DEL VECCHIO, C., AND BILIOTTI, V. A study of an adaptive secondary mirror. In *European Southern Observatory Conference and Workshop Proceedings* (1994), vol. 48, p. 247.

- [36] SATO, T., ISHIDA, H., AND IKEDA, O. Adaptive pvdf piezoelectric deformable mirror system. *Applied Optics* 19, 9 (1980), 1430–1434.
- [37] SCHOTT NORTH AMERICA INC. D 263 LA eco Thin Glass. http://www.us.schott.com/advanced_optics/english/products/optical-materials/thin-glass/thin-glass-d-263-la-eco/index.html. Accessed: 11-7-2013.
- [38] SCHWARZL, F., AND STRUIK, L. Analysis of relaxation measurements. *Advances in Molecular Relaxation Processes* 1, 3 (1968), 201–255.
- [39] SONG, H., SIMONOV, A. N., AND VDOVIN, G. Multiplexing control of a multichannel piezoelectric deformable mirror. In *Proceedings of the SPIE* (2005), vol. 6018, pp. 60181F–60181F–10.
- [40] STAHL, H. P. Design study of 8 meter monolithic mirror uv/optical space telescope. In *Astronomical Telescopes and Instrumentation: Synergies Between Ground and Space* (2008), International Society for Optics and Photonics, pp. 701022–701022.
- [41] STEINHAUS, E., AND LIPSON, S. Bimorph piezoelectric flexible mirror. *Journal of the Optical Society of America* 69, 3 (March 1979), 478–481.
- [42] STONEY, G. G. The tension of metallic films deposited by electrolysis. *Proceedings of the Royal Society of London. Series A, Containing Papers of a Mathematical and Physical Character* 82, 553 (1909), 172–175.
- [43] TOKOVININ, A., THOMAS, S., AND VDOVIN, G. Using 50-mm electrostatic membrane deformable mirror in astronomical adaptive optics. In *Astronomical Telescopes and Instrumentation* (2004), International Society for Optics and Photonics, pp. 580–585.
- [44] UNITED LAUNCH ALLIANCE. Delta IV Launch Services Users Guide. http://www.ulalaunch.com/site/docs/product_cards/guides/Delta%20IV%20Users%20Guide%20June%202013.pdf. Accessed: 11-7-2013.
- [45] WILKIE, W. K., BRYANT, R. G., HIGH, J. W., FOX, R. L., HELLBAUM, R. F., JALINK JR, A., LITTLE, B. D., AND MIRICK, P. H. Low-cost piezocomposite actuator for structural control applications. In *SPIE's 7th Annual International Symposium on Smart Structures and Materials* (2000), International Society for Optics and Photonics, pp. 323–334.
- [46] YANG, E.-H., HISHINUMA, Y., CHENG, J.-G., TROLIER-MCKINSTRY, S., BLOEMHOF, E., AND LEVINE, B. M. Thin-film piezoelectric unimorph actuator-based deformable mirror with a transferred silicon membrane. *Microelectromechanical Systems, Journal of* 15, 5 (2006), 1214–1225.

- [47] ZHANG, W. Manufacture of mirror glass substrates for the nustar mission. In *SPIE Optical Engineering+ Applications* (2009), International Society for Optics and Photonics, pp. 74370N–74370N–11.
- [48] ZHANG, W. Next generation x-ray optics: High angular resolution, light weight, and low production cost. In *American Astronomical Society Meeting Abstracts* (2013), vol. 221.